Structured Illumination for Super-Resolution Terahertz Imaging

JAMES GILL-FLEMING

Structured Illumination for Super-Resolution Terahertz Imaging

James P. Gill-Fleming

A thesis presented for the degree of

Doctor of Philosophy

Centre for Advanced Instrumentation

Durham University

United Kingdom

May 2025

Structured Illumination for Super-Resolution Terahertz Imaging

James P. Gill-Fleming

Abstract

In this thesis, advanced imaging techniques from the field of microscopy are adopted to perform structured illumination super-resolution imaging at the terahertz (THz) frequency band (0.1-10 THz). Through the use of a structured sinusoidal illumination, higher spatial frequency information that is inaccessible via diffraction-limited widefield imaging is encoded into our images. A Fourier-based reconstruction algorithm produces an image with a resolution better than that allowed by the diffraction-limit.

For this work, a recently demonstrated, novel 0.55 THz imaging system that performs efficient THz-to-optical conversion using a room-temperature vapour of excited caesium atoms is used. Such a system offers kilohertz framerate speeds, enabling the exploration of these advanced imaging techniques that have, until now, been overlooked at the THz band.

This work will explore the concepts, theory and experimental implementations of two super-resolution imaging techniques and demonstrate an image resolution improvement of $\times 1.74 \pm 0.03$ when compared to diffraction-limited widefield imaging.

Supervisors: John M. Girkin and Kevin J. Weatherill

Declaration

The work in this thesis is based on research carried out at the Centre for Advanced Instrumentation and the Quantum Light and Matter Group in the Department of Physics, University of Durham, England. No part of this thesis has been submitted elsewhere for any other degree or qualification, and it is the sole work of the author unless referenced to the contrary in the text.

This work was supported by the Engineering and Physical Sciences Research Council (EPSRC) through an EPSRC studentship.

Publications

Some of the work presented in this thesis has been published in journals and conference proceedings - the relevant publications are listed below.

- J. P. Fleming, L. A. Downes, J. M Girkin, K. J Weatherill, "Structured illumination for super resolution terahertz imaging." Presented at *Terahertz, RF, Millimeter, and Submillimeter-Wave Technology and Applications XVII, San Francisco, United States* (2024, January)
- J. P. Fleming, L. A. Downes, J. M Girkin, K. J Weatherill, "Virtually structured illumination for terahertz super-resolution imaging", *In submission to Optics Express*

Acknowledgements

Some of the people I'd like to acknowledge here have no background or interest in anything this thesis explores, but have been a source of motivation and inspiration nonetheless. I find it incredibly kind, humble and selfless to support a person's passion when it does not align with your own. Thank you.

On the personal basis, it would be best to start with my two excellent supervisors Kevin and John. I have enjoyed the freedom you have given me to really take ownership and control over my own research, while still having the knowledge I had your support at a moments notice. Thank you for your guidance, thank you for your time and most importantly, thank you for your belief.

Thank you to everyone in the THz group, past and present. To Lucy, Andrew and Matt, you've all been so supportive and welcoming from day one. You three arguably set the tone for the group, and that was one that was welcoming and supportive. I have never hesitated to ask questions or share my opinion with the group, which often lead to worthwhile discussions. I am undoubtedly now a better researcher as a result. To Tepi and Gianluca, who have worked hard on their PhDs alongside mine. For a lot of the time, it felt our research ran adjacent, as we spun off in our own directions. For that I am glad. Whether you were presenting breakthroughs or challenges of your research, it has been a source of motivation and inspiration for my own work. I wish you both the best on your future ambitions.

I would like to thank everyone from both QLM and CfAI. I have had the privilege of being a part of both groups. While this has meant twice the group meetings and seminars to attend and twice the presentations to deliver, that has been outweighed by what has felt like more than twice the support and friendship.

To my friends and family, thank you for filling out my life with everything else but Physics. At times my PhD could have become all consuming, but having a good network of people to spend my downtime with has enabled me to keep refreshed and motivated throughout my PhD.

To Mum and Dad, I am profoundly grateful for a lifetime of endless support, and guidance. It has always felt like I have had a natural work ethic and sense of curiosity, but I am sure it is a result of your love and nurturing. From a young age, it was a continual joke that I would never leave education, and I am sure this thesis just adds to it.

To Dylan, thank you for being the best brother and friend. For someone who decided Computer Science was a better idea, I admire your intelligent questions about my work and Physics in general. On more than one occasion have you stopped me in my tracks and made me revaluate my own understanding. To me, the work in this thesis is clearly better off as a result.

And finally, this thesis would not exist if it wasn't for the unwavering love and support from my wife Alex, who has lived (and endured) every twist and turn of my PhD with me. In the difficult times of my PhD, you'd always reassure me that everything happens for a reason, despite my protests against any concept of fate. You would then highlight that I was that kind of person where everything manages to work its way out in the end, to which my argument was then lost. During my PhD you have worked hard on your own goals and achievements, yet haven't faltered when it came to help me pursue mine. Being there everyday is truly an underappreciated gift, thank you.

Contents

Abstract i

Declaration ii

Acknowledgements iv

List of Figures x

List of Tables xiii

Nomenclature xiv

1 Introduction 1

1.1 The THz Band 1

1.2 THz Imaging 3

1.2.1 Single Pixel Imaging 3

1.2.2 Focal Plane Arrays 4

1.3 An Atom-based Approach 5

1.3.1 Alkali metals 5

1.3.2 Rydberg atoms 6

1.3.3 THz Detection Scheme 8

1.4 Structured Light 9

1.5 Super-resolution Imaging 10
1.6 Structured Illumination Super-resolution Imaging 11
1.7 Thesis Structure 11
1.8 Publications 12

2 Experimental Setup **13**
2.1 Atomic System 13
2.2 Optical Bench Layout 15
2.3 Excitation Lasers 16
2.3.1 Laser Frequency Stabilisation: Basic Principles 17
2.3.2 Laser 1: Ground-state Polarisation Spectroscopy 19
2.3.3 Laser 2: Excited-state Polarisation Spectroscopy 21
2.3.4 Laser 3: Pound-Drever-Hall Cavity Frequency Locking 23
2.3.5 Laser Beam Shaping 27
2.4 Caesium Vapour Cell 28
2.5 THz Objective Lens 29
2.6 Optical Readout 30
2.7 THz Illumination Source 30
2.7.1 Microwave Seed Signal 32
2.7.2 THz Power Control 32
2.7.3 THz Emission and Beam Shaping 33
2.8 Image Processing 34
2.9 Conclusion 35

3 Image Resolution **36**
3.1 Defining Resolution 36
3.1.1 Abbe's Limit 37
3.1.2 Rayleigh Criterion 38
3.1.3 Sparrow Limit 39
3.1.4 Outlook 40

3.2 System Response Functions 41
3.2.1 Point Spread Function 41
3.2.2 Edge Spread Function 44
3.2.3 Line Spread Function 45
3.2.4 Modulation Transfer Function 46
3.2.5 Outlook 48
3.3 Quantitative Resolution Measurements 49
3.3.1 1951 USAF target 49
3.3.2 Single pinhole 53
3.3.3 Slanted Edge Method 54
3.3.4 Siemen Star 57
3.3.5 Comparison 61
3.4 Conclusion 62

4 Structured Illumination Super-Resolution Imaging 63

4.1 The Structured Illumination Concept 63
4.2 Theory 64
4.2.1 Fourier Band Separation 67
4.2.2 Deconvolution 69
4.2.3 Band Shifting 69
4.2.4 Reconstruction 70
4.2.5 Additional Comments 72
4.3 Simulation 73
4.3.1 Implementation Details 74
4.3.2 Results 77
4.4 Generating Structured THz Illumination 79
4.4.1 Imaged Grating 80
4.4.2 Fresnel Biprism 84
4.4.2.1 Biprism Design 85
4.4.2.2 Biprism Manufacture 86

4.4.2.3 Characterising Biprism Performance 87
4.4.3 Choice of Structured Illumination 89
4.5 Experimental Implementation 90
4.5.1 Target Mask 91
4.5.2 Calibration 92
4.5.3 Additional Image Processing 93
4.6 Results 93
4.6.1 Incorrect Phase 95
4.6.2 Incorrect Spatial Frequency 96
4.6.3 Additional spatial frequencies 96
4.7 Conclusion 97

5 Virtually Structured Detection **98**
5.1 Concept 98
5.2 Theory 100
5.3 Advantages of Virtually Structured Detection 104
5.4 Generating THz Line Illumination 105
5.4.1 Cylindrical lens 106
5.4.2 Projected sub-diffraction slit 107
5.4.3 Comparison 108
5.5 Simulation 109
5.6 Experimental Implementation 113
5.6.1 Calibration 115
5.7 Results 117
5.7.1 USAF Target 117
5.7.2 Image Icon Targets 121
5.8 Conclusion 125

6 Conclusion and Outlook **127**
6.1 Image Deconvolution 127

6.2 Improved Widefield Structured Illumination 128
6.3 Beam-scanning Virtually Structured Detection 128
6.4 Other Structured Illumination Technqiues 129
6.4.1 Optical Sectioning 129
6.4.2 THz Off-Axis Holography 129
6.5 Conclusion 130

Appendix A Fourier Domain Shifting **132**

Appendix B VSD Convolution **134**

Bibliography **136**

List of Figures

1.1 THz band within the electromagnetic spectrum 2

1.2 Calculated THz transitions for alkali metal Rydberg atoms 7

1.3 General excitation scheme for THz detection in caesium 8

2.1 Caesium atom excitation Scheme for 0.55 THz imaging 14

2.2 THz Imaging Optical Bench Layout 15

2.3 Ground-state polarisation spectroscopy schematic layout. 19

2.4 Ground-state polarisation locking signal 20

2.5 Excited-state polarisation spectroscopy experimental layout 21

2.6 Excited state polarisation spectroscopy error signal 22

2.7 Experimental layout for Pound-Drever-Hall laser locking 23

2.8 PDH reflected power vs detuning for a reference cavity 24

2.9 PDH Photodiode signal vs. laser frequency detuning 26

2.10 Error signal generated by the PDH technique 27

2.11 Top down schematic view of the caesium vapour cell 28

2.12 Power output vs. Output frequency for the AMC 702 31

2.13 Power output vs. UCA voltage for the AMC 702 32

2.14 THz image processing 34

3.1 Comparison of Rayleigh vs. Abbe vs. Sparrow resolution definitions . . 37

3.2 Abbe's limit based on simple lens geometry. 38

3.3 System response functions 41
3.4 PSF Simulation 42
3.5 Gaussian vs. Airy PSF 43
3.6 ESF profile from a simulated image of a high-contrast edge 44
3.7 LSF profile from a simulated image of a slit 46
3.8 MTF curve of the Gaussian model 47
3.9 1951 USAF Resolution Target 50
3.10 THz USAF Resolution Target 51
3.11 Widefield 0.55 THz image of the USAF resolution target 52
3.12 Measurement of the PSF through imaging a single pinhole 53
3.13 THz widefield image of a slanted edge. 54
3.14 Slanted edge ESF and MTF measurement 56
3.15 Siemen star targets for N=16 and N=65 57
3.16 Varying contrast across a Siemens star target 58
3.17 THz 8-Spoke Siemen Star Target 59
3.18 Siemen star MTF measurement 60

4.1 Moiré fringes from two similar patterns 64
4.2 Pictorial representation of the *imaging equation* 65
4.3 Pictorial representation of SIM Fourier reconstruction 67
4.4 Simulated reconstruction of SIM Fourier spectrum 71
4.5 Masking of Fourier bands 76
4.6 SIM THz simulation using Ψ target 77
4.7 Structured illumination through an imaged grating 80
4.8 Photo of 3D printed masks for structured illumination 81
4.9 Resulting illumination from illumination masks 82
4.10 Diagram of a Fresnel biprism producing structured illumination 84
4.11 Fringe separation vs. biprism pitch angle 85
4.12 Photo of the manufactured PTFE biprisms 86
4.13 Imaged biprism fringes vs. pitch angle 87

4.14 Biprism fringe profile for the $\alpha = 30°$ biprism 88
4.15 Experimental layout for THz SIM using a Fresnel birprism 90
4.16 Photo of THz brass target mask 92
4.17 SIM Durham Shield result 94
4.18 SIM phase validation 95

5.1 Schematic diagram of the VSD processing 103
5.2 Line illumination from a cylindrical lens 106
5.3 Line illumination from a sub-diffraction slit 107
5.4 Simulation target object and widefield image 109
5.5 Simulated virtually structured image 110
5.6 VSD simulation using a USAF target 112
5.7 Experiential layout for THz VSD 113
5.8 Line illumination calibration 115
5.9 Photo of manufactured USAF Target 117
5.10 VSD Super-resolution results of the USAF target 118
5.11 VSD Edge Spread Function measurement 120
5.12 Photo of manufactured Icon Target 121
5.13 VSD results for each orientation angle 122
5.14 VSD image icon results 123

List of Tables

1.1 Scaling of Rydberg atom properties 6

3.1 Results of quantitative resolution measurements 61

4.1 Comparison between an optical microscope and THz imaging system . . 73

Nomenclature

AMC Amplifier Multiplier Chain

UCA User Controlled Attenuation

ESF Edge Spread Function

MTF Modulation Transfer Function

OTF Optical Transfer Function

PSF Point Spread Function

FWHM Full Width Half Maximum

SIM Structured Illumination Microscopy

VSD Virtuall Structured Detection

Chapter 1

Introduction

The work presented in this thesis is the union of three seemingly separate, but equally fascinating fields. That of terahertz imaging, Rydberg atomic physics and Super-resolution microscopy. Each field, in its own right, is the culmination of decades of research, innovation and development.

Recent work has coupled the use of Rydberg atomic physics and terahertz (THz) imaging to produce a highly effective atom-based THz imaging sensor [1]. This thesis endeavours to leverage this new technology to adapt advanced optical imaging techniques developed in the field of microscopy, and implement them at the THz domain.

1.1 The THz Band

Commonly defined between 0.1-10 THz [2] the THz band is the narrow frequency range positioned between the microwave and far infrared bands, as shown in Figure 1.1. From the first practical demonstration of THz imaging in 1995 [3], the THz field has garnered interest due to the many promising properties associated with THz waves. Notably, THz radiation readily penetrates common optically opaque materials such as plastics, cloth and paper, making it a promising technology for use in non-destructive testing with uses in pharmaceutical quality control [4], food inspection [5, 6] and analysis of historical objects [7].

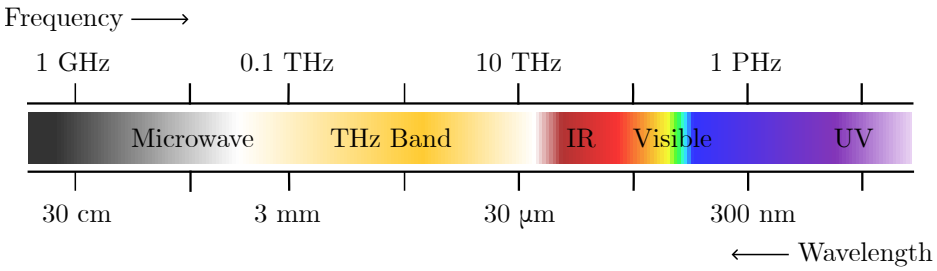

Figure 1.1: A portion of the electromagnetic spectrum, displaying the position of the THz band (0.1 - 10 THz) between the lower frequency microwave and higher frequency infrared bands. The corresponding frequency and wavelengths of each band is shown.

Furthermore, the low energy photons of THz waves (0.4 - 40 meV) means THz radiation is non-ionising, making it a safe alternative to x-ray imaging in security applications [8, 9] and a promising diagnostic tool for biological and medical applications [10, 11].

Terahertz radiation is strongly attenuated by polar liquids, including water and therefore can be used for hydration monitoring. This has applications from building material inspection [12] to medical applications such as monitoring the healing process of skin burns [13, 14] and identifying the boundaries between healthy and malignant (cancerous) tissue [15].

Historically, detection of THz radiation has been difficult. Semiconductor-based detectors fail in the THz band because the low photon energy of THz radiation is insufficient to overcome the band gap of most semiconductors. While electronic methods common to RF and microwave detection aren't suitable for the faster, higher frequency THz waves. This led to the coined term 'THz gap', highlighting the challenges associated with this frequency range [16].

1.2 THz Imaging

THz imaging approaches can be broadly characterized into two categories, single pixel imaging and focal plane arrays. Either approach comes with its own advantages and limitations that influence its use in practical applications. With no current THz technology being the clear option for all THz imaging use cases.

1.2.1 Single Pixel Imaging

The single-pixel imaging approach uses a single 'bucket' detector that is unable to discern any spatial information. Therefore images must be constructed, typically through raster scanning an object to build up an image pixel-by-pixel [17]. Through this approach, high-resolution images can be produced at the expense of long acquisition times. This trade-off between better spatial resolution at the expense of temporal resolution ultimately hinders the imaging frame-rate, which has yet to demonstrate video-rate capability. Broadband THz point detectors, such as Golay cells [18], can operate at room-temperature but are highly susceptible to noise [19] and therefore require exposure times than can exceed 1 second per pixel.

As a result, a large focus on single-pixel imaging research has been to improve the acquisition speed. Either through improved detector sensitivity, allowing for reduced exposure times per pixel [20–22] or advanced beam-scanning systems that allows for faster raster scanning [23]. One recent innovative approach employs the use of THz spatial light modulators (SLMs) to perform single-pixel compressive sensing by using a series of patterned illuminations.

Such an approach is innovative on two counts. First, it eliminates the need for raster scanning the sample, so the acquisition speed is no longer constrained by mechanical motion but instead by the rate at which spatial patterns can be projected onto the sample. While this enables faster imaging, it still falls short of achieving true video-rate speeds [24, 25]. Second, by leveraging optical excitation to encode spatial

information, single-pixel terahertz imaging decouples spatial resolution from the longer THz wavelengths. This allows the achievable image resolution to be governed by the much shorter wavelength of the optical beam used for excitation, enabling super-resolution imaging well beyond the conventional THz diffraction limit [26].

A key advantage of single-pixel imaging occurs when paired with spectroscopic THz detectors, which enables the production of images with rich spectral information [27]. THz time-domain spectroscopy (THz-TDS) systems which work by emitting ultrafast terahertz pulses and measuring their time-resolved electric field after interaction with a sample, allows for the measurement of both amplitude and phase information. Fourier transformation of the terahertz pulses, provides high resolution spectral information about the sample. THz-TDS systems are therefore widely used for non-destructive material characterization, particularly useful in applications that want to perform material discrimination [28, 29].

1.2.2 Focal Plane Arrays

Focal plane arrays encompass THz detectors that can produce full-field images in a single-shot, and without the need for scanning individual pixels can achieve much faster imaging speeds. Such detectors consist of pixel arrays that form the overall imaging sensor.

Examples include field-effect transistors [30] and microbolometer arrays [31]. These sensors can operate at room-temperatures while achieving video-rates of up to 90 Hz, but suffer from high read-out noise, poor sensitivity and limited spatial resolution [32, 33]. Despite this, these technologies are now commonly found in commercial uncooled THz cameras [34].

Detectors based on super-conducting materials can provide improved sensitivity, but at the cost of expensive cryogenic cooling while suffering from similar scaling issues [35, 36]. As a result, they have found limited use in THz applications.

THz focal plane arrays are not without their drawbacks. They are currently limited

to broadband detection, and are unable to capture spectral information that would be useful for many diagnostic applications. Additionally for arrays with a sufficient number of pixels, the image spatial resolution is still limited by diffraction, and is therefore produced images can only resolve spatial details on the order of the imaging wavelength (30 μm - 3 mm).

1.3 An Atom-based Approach

Recently, a new approach to THz widefield imaging has been presented based on THz-to-optical conversion, facilitated by a thermal vapour of alkali metal Rydberg atoms [1, 37, 38]. This highly efficient process enables the conversion of THz photons to optical photons that can then be readily detected through the use of an optical camera. In doing so, this approach enables full-frame THz imaging with unprecedented sensitivity and speed.

1.3.1 Alkali metals

The alkali metals have quickly become the atomic species of choice for many atomic experiments. These atoms have a single valence electron and therefore can be modelled approximately as simple hydrogen-like systems; with a single outer valence electron and an single effective core. This makes it possible to calculate their atomic properties to high accuracy, enabling practical experimental applications and precise control in a wide range of atomic experiments [1].

Alkali metals also exhibit high vapour pressures at room temperature, which enables many atom-light experiments with an ensemble of atoms in the form of a contained thermal vapour. Doing away with the need for complex laser cooling and trapping arrangements that would be required for equivalent cold-atom experiments.

1.3.2 Rydberg atoms

Rydberg atoms, named so after Johannes Rydberg, are atoms that are in highly excited states of high principle quantum number, n [39]. Such atoms have their valence electron far from the atomic nucleus, making them highly sensitive to external electric fields and exhibit unusually long lifetimes. Such properties of Rydberg atoms make them attractive for a wide range of sensing applications across the radio, microwave, terahertz ranges [40, 41]. The properties of Rydberg atoms scale non-linearly with n, and therefore quickly become 'exaggerated' with increasing n. A few of these property scalings are shown in Table 1.1.

Table 1.1: Scaling of various Rydberg properties with respect to n, the principle quantum number [39].

Property	n scaling
Binding energy Energy required to remove the electron from the atom.	n^{-2}
Energy level spacing The difference in energy between adjacent quantum states.	n^{-3}
Orbital radius The average distance of the electron from the nucleus.	n^{2}
Dipole moment Interaction between the electric dipole moment and external fields.	n^{2}
Polarisability The ability of the atom to become polarized in an electric field.	n^{7}
Radiative lifetime Average lifetime before decaying to a lower energy state.	n^{3}

When coupled with the simple structure of alkali metal atoms, the properties of Rydberg states can be readily calculated using software packages such as ARC (Alkali Rydberg Calculator) [42]. This enables precise modelling of their interactions with external fields, allowing for the design and optimization of Rydberg-based sensing applications.

For the application of THz sensing and imaging, there are two main Rydberg properties of interest. One, the energy level spacing, where for relatively modest values of n, the neighbouring Rydberg states are separated by an energy spacing corresponding to THz frequencies [39]. And therefore these Rydberg states are sensitive to resonant THz fields. Second, is the very large dipole moments of Rydberg states, which results in a high probability of interaction [1], and therefore high sensitivity to an incident THz field.

Through the use of ARC [42], we can model and calculate the possible THz transitions that we can feasibly detect with a Rydberg alkali metal atom sensor. A portion of this spectrum is shown in Figure 1.2 for three alkali metals with appreciable vapour pressure at room temperature.

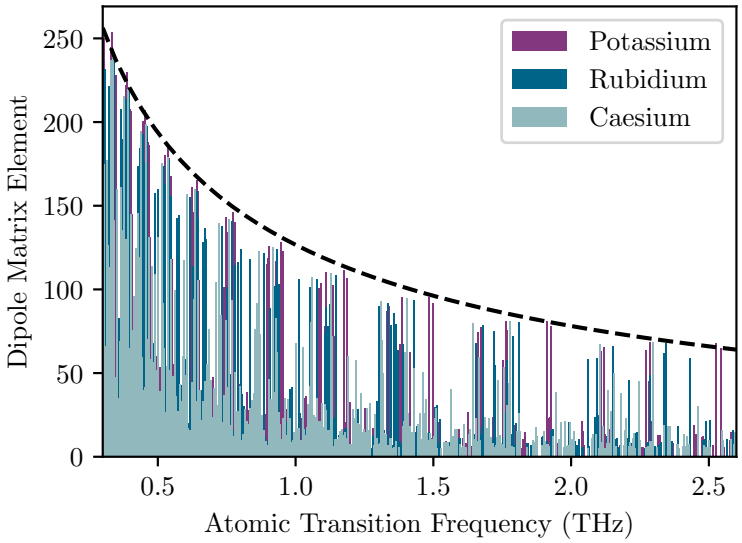

Figure 1.2: The THz transition spectrum of potassium, rubidium and caesium calculated using ARC. The general trend of decreasing sensitivity to external THz fields with increasing transition frequency is indicated by the black dashed line. Using code adapted from Dr Lucy A. Downes (with permission).

Each atomic species offers a rich spectrum of THz separated transitions, that could feasibly be used as part of a THz detection scheme. Only a small frequency portion is shown, with the possible spectrum for each atomic species extends much further both into the microwave and higher THz band.

1.3.3 THz Detection Scheme

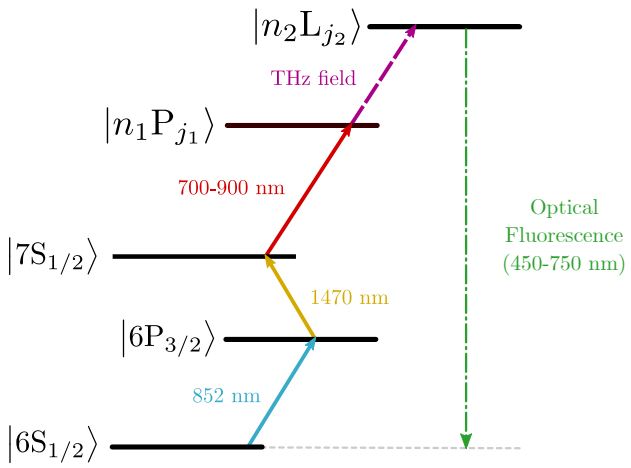

Figure 1.3: General excitation scheme for THz detection in caesium. By preparing the caesium to a THz-sensitive state enables efficient THz-to-optical conversion.

Knowing that alkali metal atoms have a rich spectrum of possible THz transitions, we can devise an atomic excitation scheme to perform THz-to-optical conversion. A general scheme for caesium is outlined Figure 1.3. In this scheme we first excite caesium from its ground-state $6\,\mathrm{S}_{1/2}$ to $n_1\mathrm{P}_{j_1}$ - a THz sensitive state of choice. In this 'prepared' state, the caesium atom can be further excited to a higher energy state, $n_2\mathrm{L}_{j_1}$, by a resonant THz field. The frequency of this THz field corresponds to the energy gap between the these two states. At this final excited state, the caesium atom will spontaneously decay back to the ground-state through known probabilistic decay pathways, emitting optical photon(s) in the process. It is this optical fluorescence that constitutes as the detection of the incident THz field. The continual conversion of THz photons to optical photons is therefore facilitated by the continual excitation and spontaneous decay of caesium atoms.

The choice of transition $n_1\mathrm{P}_{j_1} \rightarrow n_2\mathrm{L}_{j_1}$ is a complex decision based on numerous factors which have been well discussed [37, 38]. Briefly, this includes the spectral contrast between the signal fluorescence and background fluorescence, the transition coupling strength to the external resonant THz field and the available power from both the THz illumination source and excitation lasers.

This thesis uses a previously built THz imaging system based on a 0.55 THz Rydberg transition in caesium which achieves a conversion efficiency of 52.4% [37]. That is, approximately every two incident THz photons leads to the emission of one optical 'signal' photon. This results in a THz imaging detector with exceptional sensitivity, which enables imaging at very high framerates, with the most recent results demonstrating a framerate of up to 12,000 frames-per-second [38].

The many design choices, including the choice of the 0.55 THz transition, is covered in great detail in [1] and further in [43]. A more operational-centric description of the THz imaging system is also provided in Chapter 2.

1.4 Structured Light

Structured light refers to electromagnetic fields with deliberately shaped spatial or temporal profiles, engineered in amplitude, phase, or polarization. Spatially structured beams—such as Airy, Bessel, and vortex beams—can exhibit non-diffracting, self-healing, properties [44], while temporally structured pulses enable control over spectral content and interaction dynamics [45].

These engineered light fields have driven advances across diverse domains, from super-resolution microscopy [46] and optical trapping [47] to high-capacity communication [48] and precision metrology [49].

Importantly, recent work has extended the frontier of structured light into the terahertz (THz) domain [50], using spatially structured non-paraxial Airy beams for THz imaging, achieving enhanced resolution and contrast when imaging obstructed samples. This work not only showcases the practical viability of structured illumination in the THz band but also reinforces its potential for transformative impact in non-destructive imaging and material inspection.

1.5 Super-resolution Imaging

Super-resolution imaging has been almost exclusively championed by the field of microscopy, where its motivation is clear. Through conventional microscopy, the continual drive to resolve ever-smaller features of biological cells quickly encounters the seemingly insurmountable limit of diffraction, which sets a hard limit on the resolution of an imaging system. Super-resolution imaging changes this narrative, by producing images with a spatial resolution beyond what would be allowed by diffraction. With over 30 years of research, super-resolution microscopy has become a vast and diverse field, featuring many different techniques for *sub-diffraction* imaging [51–53].

The question is therefore, what is the motivation behind super-resolution imaging at the THz band? As shown in Figure 1.2 there is a multitude of THz transitions to chose from, many at higher THz frequencies than our chosen 0.55 THz transition. Opting for one of these higher frequencies would produce widefield images with better diffraction-limited resolution.

However, we must compete with additional constraints when imaging at such higher THz frequencies. For our atom-based imaging approach specifically, this includes a diminishing sensitivity with increasing THz frequency, as shown in Figure 1.2. More generally, THz imaging is further constrained by diminishing power of THz sources at higher frequencies, as source efficiencies are typically lower [54, 55]. Fundamentally, higher THz frequencies suffer from higher attenuation through common materials [56, 57], reducing their promise of high penetrating power. Combined with the other compounded constraints, opting to image at a higher THz frequency could become less attractive or even infeasible.

Super-resolution imaging in the THz band offers a potential solution, enabling higher spatial resolution while preserving the advantageous properties of lower-frequency THz radiation - offering a best of both worlds solution.

1.6 Structured Illumination Super-resolution Imaging

For this thesis, we shall focus on one class of super-resolution imaging, known in microscopy as Structured Illumination Microscopy (SIM) [46]. This Fourier-based method takes advantage of a spatially structured sinusoidal illumination to encode higher spatial resolution information into widefield images. More broadly, SIM falls under the umbrella of structured light techniques, which take advantage of engineered spatial illuminations. In the context of THz imaging, structured light offers an exciting opportunity to bypass diffraction limits while preserving the penetration and material contrast advantages of lower THz frequencies. As recent work has shown [50], applying structured illumination at THz frequencies can improve resolution and contrast, highlighting the strong potential of structured light as a tool for next-generation THz imaging.

1.7 Thesis Structure

This thesis presents and demonstrates my work on super-resolution THz imaging, achieving enhanced image resolution while maintaining the benefits of imaging at 0.55 THz. The thesis is structured accordingly.

Chapter 2 provides a broad technical overview on the atom-based THz imaging system. This chapter provides operational details of each sub-system that drives the system, including details on optical readout and imaging processing. As this system was developed and implemented prior to my arrival by Dr Lucy A. Downes, a more detailed description of the system can be found in their PhD thesis [1].

Chapter 3 introduces the concept and definitions of an imaging system's spatial resolution that I adopt and use in later chapters. I present experimental evaluations of various common resolution measurement methods, and consider the most appropriate approach for our THz system. Overall, Chapter 3 provides an important resolution benchmark for later super-resolution work.

Chapter 4 introduces the structured illumination super-resolution technique, known as Structured Illumination Microscopy (SIM). The chapter explores the concept and theory of SIM, before considering its use in the THz band. I then present results from simulation that validates the SIM method for use at the THz band. The validation from the simulation results then lead to discussion on the used experimental implementation, and then the subsequent experimental results.

Chapter 5 covers a second super-resolution technique, known as Virtually Structured Detection (VSD). This imaging scanning approach builds on the concept and theory of Chapter 4. As with Chapter 4, I validate the VSD method through simulation before implementing the method experimentally. The chapter then considers the advantages and drawbacks of the VSD approach when compared with SIM.

1.8 Publications

The following publications are a result of work presented in this thesis, in particular Chapter 5.

- J. P. Fleming, L. A. Downes, J. M Girkin, K. J Weatherill, "Structured illumination for super resolution terahertz imaging." Presented at *Terahertz, RF, Millimeter, and Submillimeter-Wave Technology and Applications XVII, San Francisco, United States* (2024, January)
- J. P. Fleming, L. A. Downes, J. M Girkin, K. J Weatherill, "Virtually structured illumination for terahertz super-resolution imaging", *In submission with Optics Express*

Chapter 2

Experimental Setup

This chapter outlines the practical implementation and experimental layout of the THz imaging system, that operates by utilising THz separated transitions in caesium to perform efficient THz-to-optical conversion and therefore imaging. While the THz imaging system facilitates the work presented in this thesis, development of the THz imager is the result of prior work by Dr Lucy A. Downes. For greater detail into the design and operation of the THz imager system, I direct the reader to their excellent and thorough works on the THz system [1, 37, 38].

2.1 Atomic System

As discussed in Chapter 1, the atom-based THz sensor approach can be used to detect a broad range of THz frequencies by choosing the appropriate THz separated atomic transition. For this thesis, we will use the $14P_{3/2} \rightarrow 13D_{5/2}$ transition in caesium which corresponds to an THz imaging frequency of 545 GHz (0.55 THz) and an optical signal fluorescence of 535 nm. The relevant energy levels of caesium for this process are shown in Figure 2.1. This particular transition was identified in previous work [1], due to favourable properties of the transition which include the transition interaction strength, contrast between signal and background fluorescence and available THz illumination power.

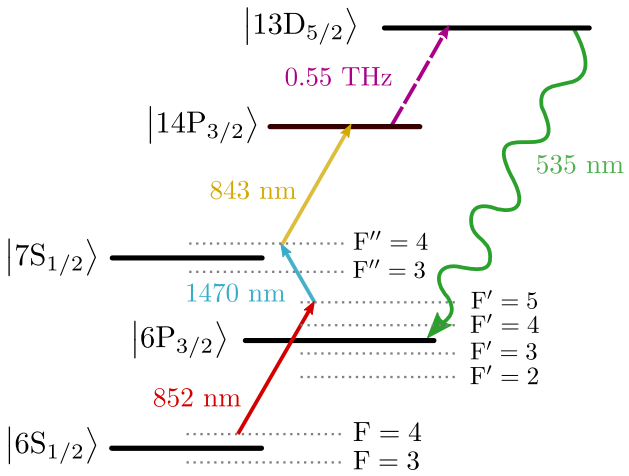

Figure 2.1: The energy level diagram of caesium, showing the excitation scheme used to achieve 0.55 THz imaging through THz-to-optical conversion. For each laser excitation, the hyperfine levels are shown.

In order to drive the $14P_{3/2} \rightarrow 13D_{5/2}$ transition by an external 0.55 THz field, the caesium atoms must first be excited to the $14P_{3/2}$ state. This is achieved by a three-step excitation scheme using three resonant infrared lasers, of wavelengths 852 nm, 1470 nm and 843 nm.

Only when the caesium atoms are 'prepared' in the $14P_{3/2}$ state, are they sensitive to an incident resonant 0.55 THz field, which further excites the caesium atoms to the $13D_{5/2}$ state. This opens up a dominant decay pathway from $13D_{5/2} \rightarrow 6P_{3/2}$, leading to the emission of green 535 nm photons, which produces a fluorescence signal, indicating the detection of THz photons.

In the absence of a THz field, the caesium atoms will probabilistically decay through alternative pathways to reach the ground state, $6S_{1/2}$. During this process, they emit a background fluorescence. Ultimately, this leads to a closed atomic system, allowing for the continual preparation, excitation and decay of the caesium atom population. This enables continuous THz-to-optical conversion, and therefore continuous THz detection and imaging.

2.2 Optical Bench Layout

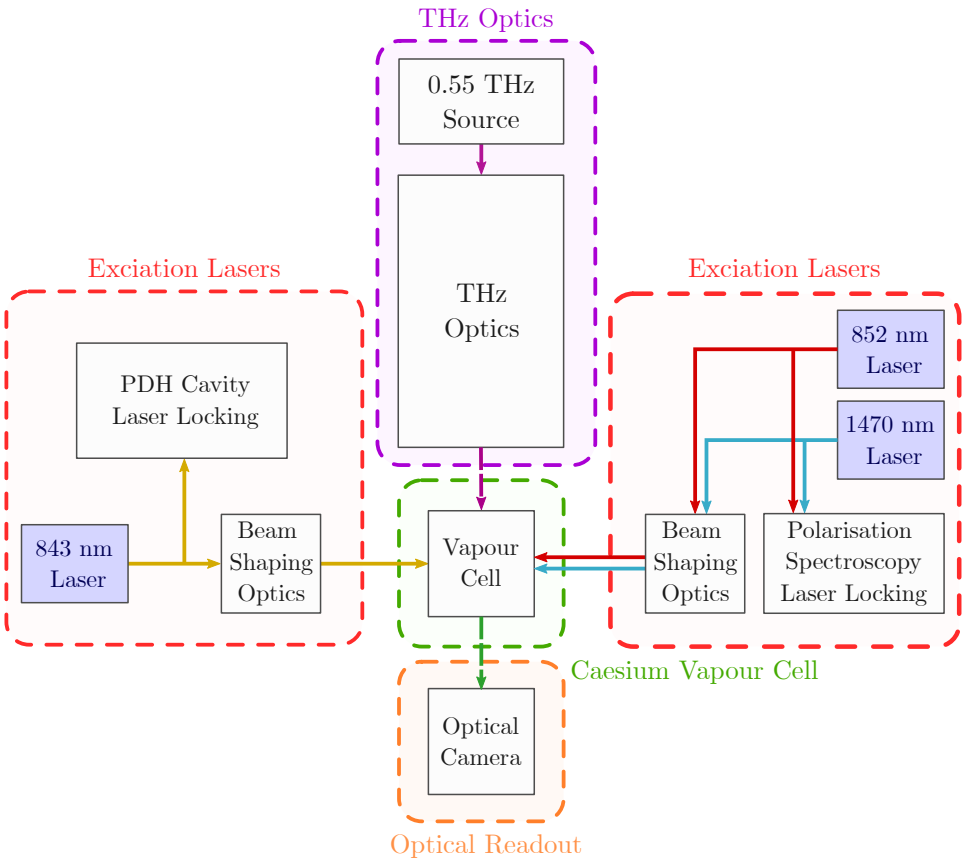

Figure 2.2: Optical bench layout for the entire THz imager system. For this thesis we run the entire imager as a unified 'camera', with only the THz optics being changed and modified.

The THz imaging system consists of four primary components on the optical bench, as illustrated in Figure 2.2.

1. **Excitation Lasers** – This subsystem includes the laser sources, frequency stabilization optics, and beam shaping elements necessary to drive the chosen excitation scheme.

2. **Caesium Vapour Cell** – At the core of the system lies the caesium vapour cell, in which THz-sensitive caesium atoms serve as the THz sensor. This component represents the THz part of the THz-to-optical conversion process.

3. **Optical Readout** – The optical readout captures fluorescence from the vapour cell using a dedicated imaging camera. This component represents the optical part of the THz-to-optical conversion process.

4. **THz Optics** – This section encompasses the THz section of the optical bench, including the THz illumination source, THz beamshaping optics, THz object targets, and THz imaging elements. A THz objective lens focuses the incident THz field into the vapour cell for detection. This is the section of primary interest in the next section.

Each section operates in unison to form a unified THz imaging system. The following section will examine these components and describe how they operate.

2.3 Excitation Lasers

The three-step excitation scheme, required to prepare the caesium atoms in the THz-sensitive state, comprises of one laser per excitation step. The wavelength of each laser is frequency stabilised, such that it remains resonant with its respective transition that it is driving.

- The first-step 852 nm laser is a Toptica DL100, and is frequency stabilised to the caesium $6S_{1/2}$ $F = 4 \rightarrow 6P_{3/2}$ $F' = 5$ hyperfine transition by the use of ground-state polarisation spectroscopy [58].

- The second-step 1470 nm laser is a Toptica DLPro, and is frequency stabilised to the caesium $6P_{3/2}$ $F' = 5 \rightarrow 7S_{1/2}$ $F'' = 4$ hyperfine transition by the use of excited-state polarisation spectroscopy [59].

- The third-step 843 nm laser is a fibre-coupled MOGLabs laser system, that is frequency stabilised to a cavity reference through the Pound-Drever-Hall locking technique [60].

The THz imager relies on the excitation lasers being resonant with their respective transitions. Maintaining this resonance ensures optimal excitation of caesium atoms with the available optical power. Ultimately, this maximises the output fluorescence and therefore the signal-to-noise of our THz images.

For a laser without active frequency stabilisation, known as 'free-running, the frequency of the laser will naturally drift due to fluctuations in environmental conditions, such as temperature, air pressure, humidity and electrical supply. Over the short-term, this results in unwanted laser frequency noise. Such noise broadens the spectral lineshape of the laser, which reduces the amount of available optical power at the resonant frequency.

Over the long term, a free-running laser will undergo large frequency drifts, causing the laser to become far from resonant with the transition. Therefore the laser no longer drives the transition which interrupts the excitation scheme, leading to a loss of fluorescence and therefore THz imaging. It is therefore necessary to ensure the frequency of our laser remains 'locked' to the resonant frequency of our atomic transition, through the use of active laser frequency stabilisation.

2.3.1 Laser Frequency Stabilisation: Basic Principles

Frequency stabilisation of a laser is an active closed-loop system and is comprised of three main components; a frequency reference, a loop controller and a servo controller.

The servo controller acts to adjust the frequency of the laser by adjusting the operating parameters of the laser. Depending on the type of laser, this may be by adjusting the laser's temperature or injection current. Or it might be by adjusting the laser's cavity length using piezoelectric actuators or by tuning an external cavity element.

The frequency reference provides a stable reference to compare the frequency of our laser, in order to determine how much the laser frequency has drifted. Such

frequency reference could be from an atomic transition, an optical cavity or another frequency stabilised laser. The frequency reference should produce a response that is proportional to the frequency drift of the laser, ideally with a sharp linear response about resonance. This is known as the frequency *error signal* and is used as feedback to the loop and servo controllers.

The loop controller is the intermediary between the frequency reference and servo controller, it takes and processes the error signal and provides feedback to the servo controller. Typically the loop controller is a PID loop (Proportional-Integral-Derivative) that optimizes the correction applied to the servo controller by balancing three components. The proportional term provides an immediate response by applying a correction proportional to the error signal, while the integral term accumulates past errors to eliminate long-term drifts. The derivative term predicts future errors based on the rate of change, damping oscillations and preventing frequency overshoot. Together, these components ensure smooth and stable frequency locking by preventing excessive corrections while minimizing drift and oscillations.

All three of our excitation lasers achieve frequency stabilisation in this manner, the only difference being in the choice of frequency reference and approach of generating the error signal from that reference.

2.3.2 Laser 1: Ground-state Polarisation Spectroscopy

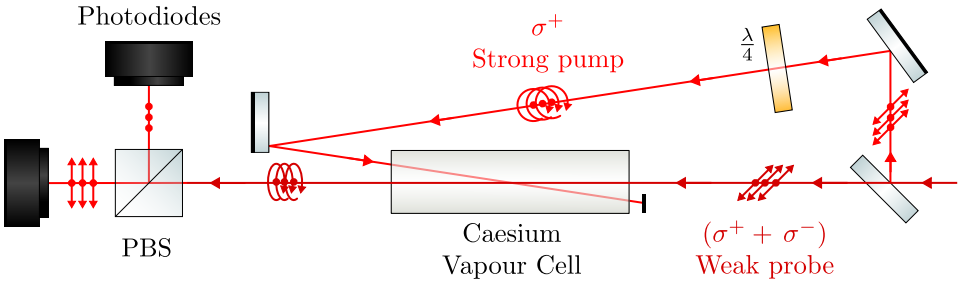

Figure 2.3: Schematic diagram of ground state polarisation spectroscopy. From a single linear polarised beam, the circularly polarised strong pump beam and linearly polarised weak probe beam are generated. The propagating direction of each beam is highlighted by the arrowheads, and shows how the two beam counter-propagate and overlap each other within the caesium vapour reference cell. The probe beam exits with a elliptical polarisation that is analysed by a polarising beamsplitter (PBS) and a pair of photodiodes.

The 852 nm first-step laser is frequency stabilised through polarisation spectroscopy [61, 62]. A technique that generates an error signal from a polarisation-dependent interaction between our laser and the $6S_{1/2}$ $F = 4 \rightarrow 6P_{3/2}$ $F' = 5$ transition of caesium atoms contained within a separate reference vapour cell. This produces a laser with a frequency that is resonant with the transition it is locked on to.

The laser input is split into two beams of differing intensity, a strong pump beam and a weak probe beam. The strong pump beam (as shown in Figure 2.3) is circularly polarized, and induces an anisotropy in the caesium vapour. This anisotropy is then measured by interrogating the caesium vapour by a counter-propagating linearly polarized weak probe beam.

The linearly polarized probe beam can be described as a combination of two beams of equal amplitude and opposite circular polarisation (σ_+ and σ_-). Because of the anisotropy, each circularly polarised component of the probe beam undergoes a difference in absorption as it passed through the caesium vapour. As a result, the probe beam exits the caesium vapour with an elliptical polarisation, with the ellipticity and angle of the polarisation proportional the difference in absorption coefficients $\Delta\alpha = \alpha_+ - \alpha_-$ [63], and therefore the degree of anisotropy.

The probe beam is analysed by a polarising beam splitter (PBS) and a pair of photodiodes. This produces a differential signal that is proportional to the anisotropy of the vapour medium. For a closed atomic transition such as this one, where the excited state exclusively decays back down to the non-excited state, the anisotropy of the caesium vapour shows a dispersive or derivative lineshape about resonance, that is ideal as an error signal [58].

Typical experimental signals from both photodiodes, and their difference is shown in Figure 2.4. The transmission of the probe beam differs between the p-polarisation

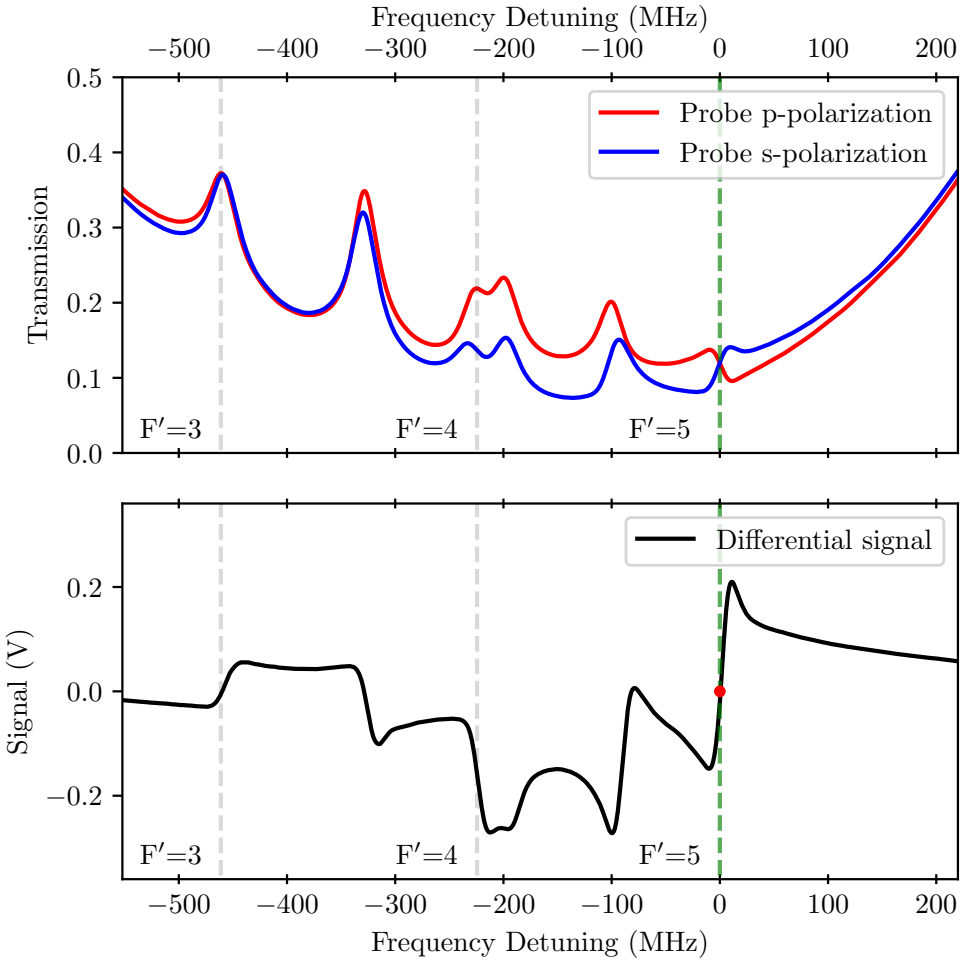

Figure 2.4: (Top) Experimentally detected power of the two linear polarisations of the rotated weak probe beam. (Bottom) The resulting differential signal, which is proportional to the degree of anisotropy induced in the caesium vapour by the counter-propagating pump beam. The differential signal is used as the laser locking error signal and is used to keep the laser's frequency resonant with the $6S_{1/2}$ F = $4 \rightarrow 6P_{3/2}$ F′ = 5 transition; this point is highlighted by the red dot.

and s-polarisation states, due to the induced difference in absorption coefficients. The frequency detuning scale is relative to the resonant point of the $6S_{1/2}$ $F = 4 \rightarrow 6P_{3/2}$ $F' = 5$ transition, which is indicated by the green dashed line. By careful adjustment of the linear polarisation of the probe beam, the zero-point of the error signal can be tuned to occur at resonance, this is indicated by the red point on the error signal curve. Around the resonant point, the error signal exhibits the ideal dispersive lineshape, that remains linearly proportional to any frequency drifting about resonance. By feeding this error signal into the control loop of the laser, we are able to stabilize the laser frequency to remain on resonance with the atomic transition.

2.3.3 Laser 2: Excited-state Polarisation Spectroscopy

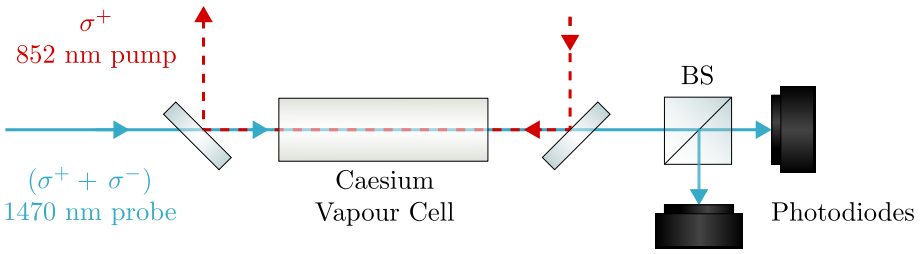

Figure 2.5: Schematic diagram of excited-state polarisation spectroscopy. The circularly polarised 852 nm pump beam (red dashed line) and the linearly polarised 1470 nm probe beam (blue solid line) counterpropagate each other within the caesium vapour reference cell. The subsequent elliptical polarised 1470 nm probe beam is then analysed by a polarising beamsplitter and photodiode pair.

The second-step 1470 nm locking uses excited-state polarisation spectroscopy [59] which is similar to ground-state polarisation spectroscopy, except the pump and probe beams are different frequencies. A strong pump beam of 852 nm drives the $6S_{1/2}$ $F = 4 \rightarrow 6P_{3/2}$ $F' = 5$ ground-state transition. The weak probe of 1470 nm laser then drives the $6S_{1/2}$ $F = 4 \rightarrow 6P_{3/2}$ $F' = 5$ excited state transition. The advantage of this approach is the existing frequency stabilised 852 nm laser is utilised for the pump beam.

Excited-state polarisation spectroscopy operates in the same fashion as ground-state polarisation spectroscopy. The circularly polarized pump beam induces an anisotropy in the caesium vapour, which causes a difference in absorption for the σ^+ and σ^+ components of the linearly polarized probe beam. The probe beam therefore exits the vapour with an elliptical polarisation, which is analysed by its own PBS and photodiode pair. For excited polarisation spectroscopy, the differential signal produced is a single dispersive signal that is ideal to frequency stabilise the 1470 nm probe laser. The ideal, theoretical signal is shown in Figure 2.6.

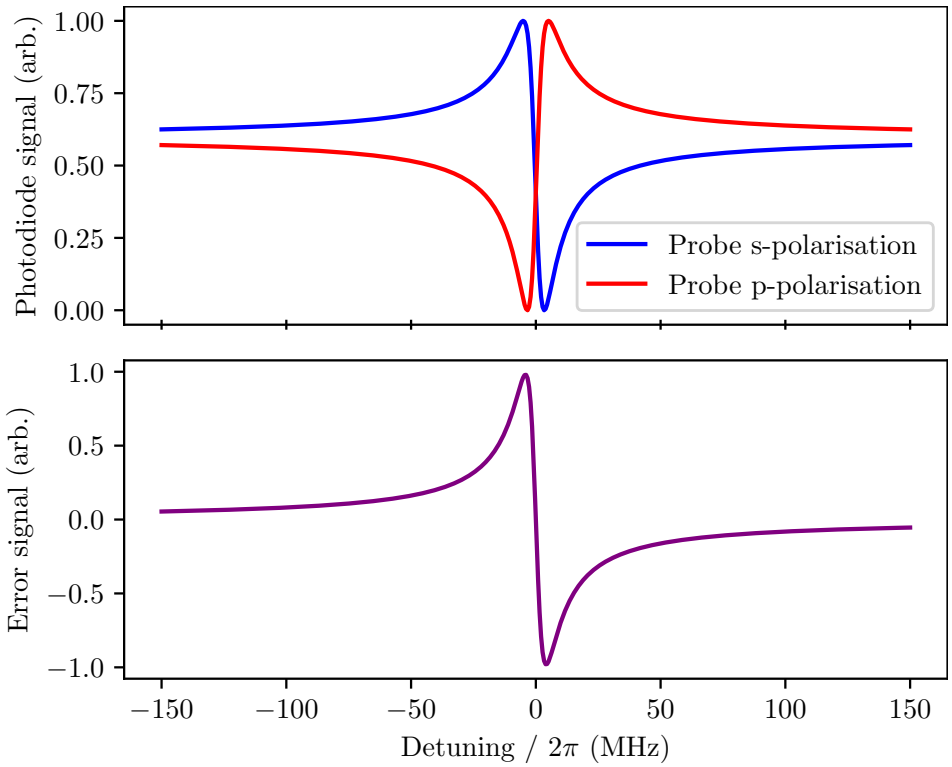

Figure 2.6: Ideal excited state polarisation spectroscopy photodiode signals and resultant dispersive error signal from their difference. Simulated case based on [59].

2.3.4 Laser 3: Pound-Drever-Hall Cavity Frequency Locking

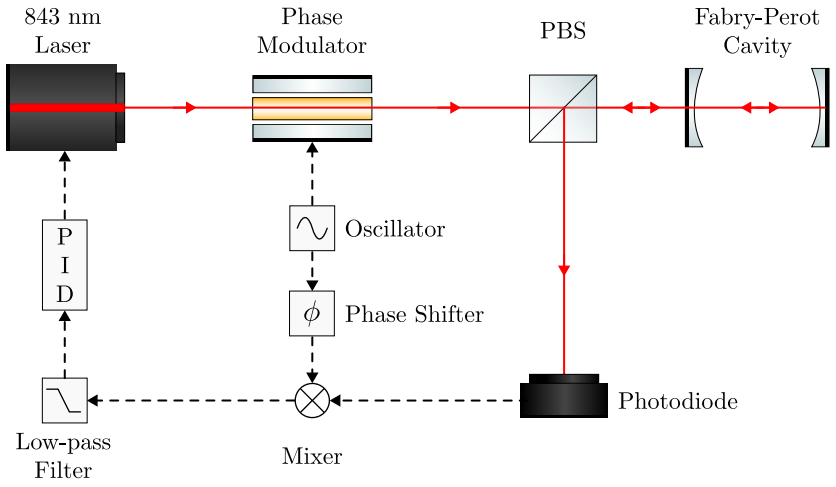

Figure 2.7: Schematic diagram of the experimental layout for Pound-Drever-Hall laser locking technique. A phase modulator adds phase sidebands to the laser beam before it entering the Fabry-Pérot cavity. The reflected power from the cavity is then detected on a photodiode. The resulting electrical signal (black dashed line) is processed to produce the error signal for the laser's PID loop.

The 843 nm third-step laser is locked to a stable reference cavity through the Pound–Drever–Hall (PDH) technique, which is used to lock a laser to one of the resonances of a reference cavity. A basic schematic of the optical setup for the PDH technique is shown in Figure 2.7.

The PDH technique locks a laser by measuring a cavity's phase response, which exhibits a dispersive feature in the reflected signal near resonance—ideal for generating a sensitive error signal. In contrast, the transmitted signal follows the cavity's intensity response and lacks the phase sensitivity needed for effective locking.

However the photodiode can not directly measure the phase response of the cavity, and instead detects in reflected power. The reflected power response is shown in Figure 2.8, and follows a symmetric inverted Lorentzian profile. This makes for a poor error signal as we can not determine the sign (direction) of the laser's frequency detuning.

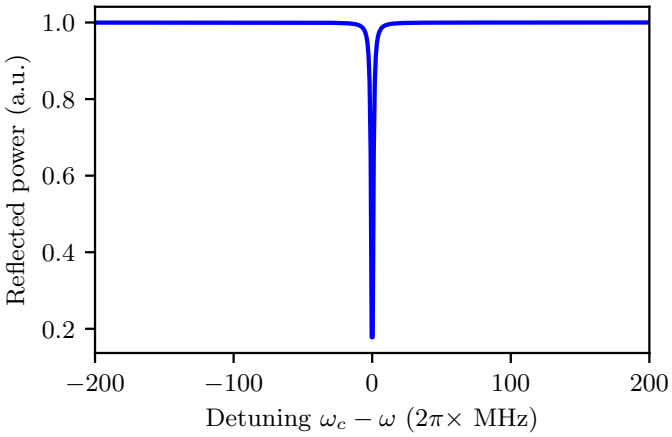

Figure 2.8: The reflected power from the cavity for a laser without phase modulation. The response is a well defined peak at the cavity resonant frequency, ω_c but the symmetric nature of the response about the cavity resonance makes for a poor error signal.

The PDH technique solves this problem by applying a varying phase modulation to the laser beam, this effectively splits the laser into three frequency components, the central carrier frequency ω_c and two sideband frequencies $\omega_c \pm \Omega$, where Ω is the modulation frequency of the phase modulator. The electric field of the modulated laser beam can be written as:

$$E(t) = E_0 e^{i\omega_c t}\left[1 + \frac{1}{2}e^{i\Omega t} - \frac{1}{2}e^{-i\Omega t}\right]. \tag{2.1}$$

Before the reference cavity, the two sidebands differ by π phase and are of equal amplitude, and therefore would not be detected by the photodiode as they cancel each other out. However, by passing the phase modulated laser through the reference cavity introduces a frequency-dependent phase delay, that affects the two sidebands differently. The effect of the cavity can be modelled by the transfer function of a Fabray-Pérot cavity [43].

$$R(\omega) = r\,\frac{1 - e^{i2\alpha(\omega)}}{1 - r^2 e^{i2\alpha(\omega)}} \tag{2.2}$$

Where r is the reflection coefficient of the mirrors and $\alpha(\omega) = \omega L/c$ is the phase picked up the laser travelling the length of the cavity. The electric field of the reflected laser beam is therefore given as

$$E_r(t) = E_0 \left[R(\omega_c) e^{i\omega_c t} + \frac{1}{2} R(\omega_c + \Omega) e^{i(\omega_c + \Omega)t} - \frac{1}{2} R(\omega_c - \Omega) e^{i(\omega_c - \Omega)t} \right] . \quad (2.3)$$

Here we note that the sidebands pick up a factor of $R(\omega_c \pm \Omega)$, which introduces a phase term to each sideband that differs in sign, therefore the symmetry of the sidebands is broken and no longer cancel out. If we consider the power at the photodiode $P_r = |E_r|^2$ we find:

$$\begin{aligned} P_r = {} & P_0 |R(\omega)|^2 \\ & + \frac{P_0}{4} \left\{ |R(\omega + \Omega)|^2 + |R(\omega - \Omega)|^2 \right\} \\ & + P_0 \left\{ \mathrm{Re}[\chi(\omega)] \cos \Omega t + \mathrm{Im}[\chi(\omega)] \sin \Omega t \right\} \qquad + (\text{terms in } 2\Omega) \end{aligned} \quad (2.4)$$

Where $\chi(\omega)$ is given by

$$\chi(\omega) = R(\omega) R^*(\omega + \Omega) - R^*(\omega) R(w - \Omega) \quad (2.5)$$

Figure 2.9 shows the detected reflected power P_r as a function of the detuning about the cavity resonance. The phase added by the cavity prevents the modulation sidebands from cancelling, leading to amplitude sidebands in our reflected laser beam. More importantly, the response is dispersive about the cavity resonance, which is a result of the contribution from $\chi(\omega)$. Ultimately $\chi(\omega)$ is the quantity of interest for the PDH technique, as it is an antisymmetric dispersive function about the cavity resonant frequency, and therefore an ideal error function.

To derive this error signal, the photodiode signal is processed through a phase-sensitive lock-in detection scheme. The photodiode voltage signal, $V_r \propto P_r$, is frequency mixed with a version of the original modulation voltage that has been delayed by a phase of ϕ.

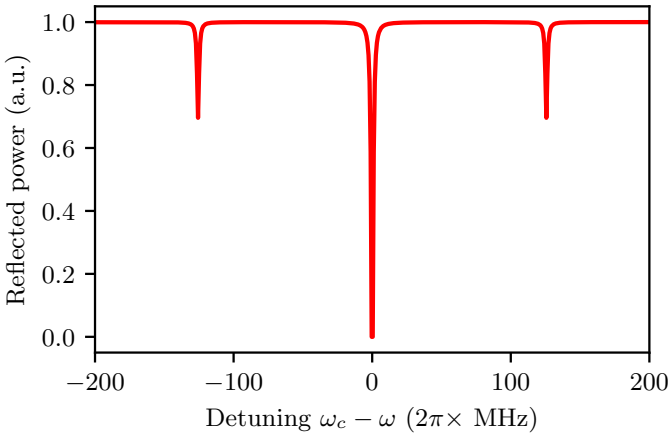

Figure 2.9: Reflected power detected by the photodiode as a function of the laser detuning about a cavity resonance, showing the central cavity resonance and induced amplitude sidebands. As reflected power is detected, the power decreases at resonance as the cavity reaches maximum transmission.

The mixed signal is therefore

$$\begin{aligned} V_{\text{mixed}}(\omega) &= V_r \cos(\Omega t + \phi) \\ &\propto P_r \cos(\Omega t + \phi) \end{aligned} \tag{2.6}$$

This mixed voltage signal is then low-pass filtered to remove the sinusodial terms of ω. This results in the error signal [64]

$$V_{\text{error}}(\omega) \propto \text{Re}[\chi(\omega)] \cos\phi + \text{Im}[\chi(\omega)] \sin\phi \tag{2.7}$$

For a typical modulation frequency of $\Omega = 2\pi\,(20\text{ MHz})$, which is large compared to the linewidth of the cavity, $\chi(\omega)$ is almost purely imaginary [43]. Therefore through appropriate choice of $\phi = \pi/2$ our final error signal is

$$\begin{aligned} V_{\text{error}}(\omega) &\propto \text{Im}[\chi(\omega)] \\ &\approx \chi(\omega) \end{aligned} \tag{2.8}$$

The resultant error signal is shown in Figure 2.10. The signal features a sharp dispersive shape at resonance, making it an ideal error signal for laser locking.

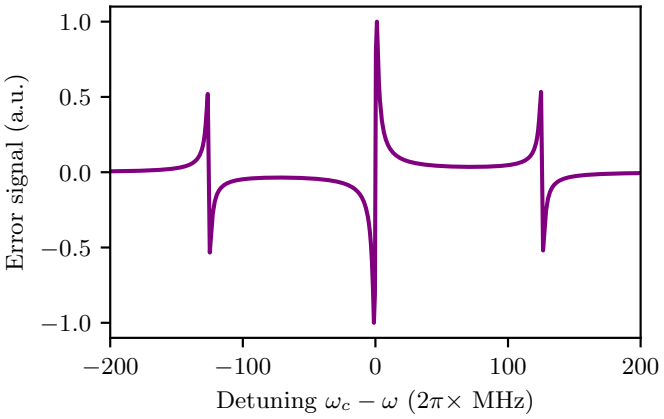

Figure 2.10: The final PDH error signal derived by demodulation of the photodiode signal. Being proportional to $\chi(\omega)$, the signal is dispersive about the resonance, making it the ideal error signal for laser locking.

2.3.5 Laser Beam Shaping

The overlapping region of the laser beams inside the vapour cell produces the excited caesium atoms that can be used to readily detect incident THz radiation. We shape all three excitation beams into overlapping lightsheets through the use of cylindrical lenses to generate a 2D sheet of excited caesium atoms, measuring approximately 10 mm$\times$10 mm$\times$100μm [1]. This 2D sheet of THz-sensitive caesium atoms acts as our imaging sensor for any incident resonant THz field.

The cylindrical lenses expand each laser beam in the vertical direction, and are positioned to overlap within the vapour cell through the use of steering mirrors. The cylindrical lenses used each have a large focal length, such that the Rayleigh range of the lighsheets are longer than the propagation distance through the vapour cell. This ensures the laser intensity remains relatively constant across the vapour cell, so that the fluorescence and resultant THz image are uniform [1].

2.4 Caesium Vapour Cell

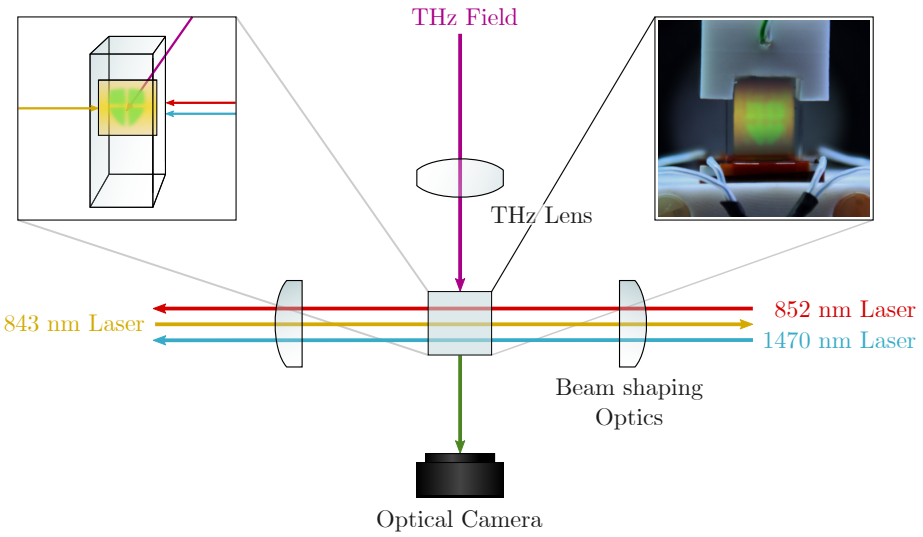

Figure 2.11: Top down view of the vapour cell, showing the use of the four sides of optical access. Left inset shows how the three excitation lasers and incident THz field enter the vapour cell and interact. The right inset shows a true-colour composite image of the vapour cell during normal operation of the THz imaging system.

The vapour cell is at the heart of the THz imaging system, it is the convergence point of the three exciation lasers, incident THz field and the focus of the optical readout system. An in-house manufactured cuboidal glass vapour cell, which measures approximately $10 \times 10 \times 60$ mm, hosts the caesium atoms and is held on the optical bench by a custom Teflon mount.

The vapour cell provides optical access to the caesium atoms from four sides, as shown in Figure 2.11. Two opposing sides of the cell provide access for the three excitation laser lightsheets, that overlap within the vapour cell, setting the position of the THz detector plane. A third side allows entry of the incident THz field, which is focused by a THz objective lens to form an image at the formed THz detector plane. The fourth, opposing side provides optical readout access, where a camera captures fluorescence emitted by the caesium atoms.

To increase the density of the caesium vapour, and therefore increase the intensity

of the fluorescence, the base of the vapour cell is heated to 45°C by two metal ceramic heaters (Thorlabs HT24S).

The temperature of the vapour cell is not actively controlled, instead the vapour cell is left to reach thermal equilibrium with the cell heater power being adjusted accordingly. The target temperature of 45 °C is a trade-off between a high number density of caesium atoms to produce a bright fluorescence, but not too high a number density that the vapour becomes optically thick. In doing so, the excitation lasers become significantly absorbed by the vapour as they propagate through the vapour cell. This leads to non-uniform fluorescence across the vapour cell.

2.5 THz Objective Lens

To be able to form THz images, a THz objective lens is required to focus the THz field from an imaging plane onto the detector plane within the vapour cell. We use a commercial two-element silicon objective lens ($\mathrm{i2S}, \mathrm{d} = 60\ \mathrm{mm}, \mathrm{f} = 70\ \mathrm{mm}$) to image onto the THz-sensitive atomic vapour. The objective is designed with a 1x magnification, and therefore performs a 1:1 correspondence from the imaging plane to the detector plane. The position of the THz objective therefore remains in a fixed position, and represents the 'front' of the THz imaging system.

2.6 Optical Readout

A key part of the THz detection scheme, is detecting the optical fluorescence signal produced by the caesium atoms in the vapour cell. For optical readout, we use an Andor iXon 887 Monochromatic EMCCD camera that is actively cooled to $-20°C$ using the on-board air-cooled Peltier element. A 1:1 Steinheil achromatic triplet lens is used to image to the fluorescing vapour. The camera is positioned such that the imaging plane of the camera corresponds to the detector plane within the vapour cell. To suppress unwanted background fluorescence and scattered infrared laser light, a bandpass filter (Semrock BrightLine 535/6nm) is added to the lens assembly.

The iXon camera is controlled by the MicroManager software package [65], an open source project used for coordination of microscope hardware. While not used strictly for microscopy in this use case, the MicroManager software allows for basic control over the camera's functionality, as well as coordinating image acquisition with other hardware, such as the translation stages that are later used in Chapter 4 and Chapter 5.

2.7 THz Illumination Source

To image with our THz system, we require a resonant THz illumination source. Just as with the infrared lasers, the incident THz field must precisely match the target transition frequency for effective excitation of the THz separated transition. To provide continuous-wave (CW) resonant THz illumination, we use a commercial Amplifier/Multiplier Chain (AMC) from Virgina Diodes. These devices are a chain of non-linear electronics that perform frequency upconversion and power amplification of a seed microwave signal to generate a high-power, narrow band CW THz field.

For this work, we will use the Virginia Diodes AMC 702 which can provide THz illumination across a short frequency range between 540-560 GHz. The output power the source can produce is frequency dependent over the tunable range with the power spectrum of the THz source shown in Figure 2.12. For the 0.55 THz imaging transition, the AMC can deliver a maximum power output of 4.53 mW. At such high powers, the strong THz field perturbs the atomic system, resulting in reduced fluorescence and consequently lower detection sensitivity. To mitigate this 'saturation effect', the AMC is operated at a reduced power level, with the optimal illumination power determined empirically by monitoring the fluorescence response.

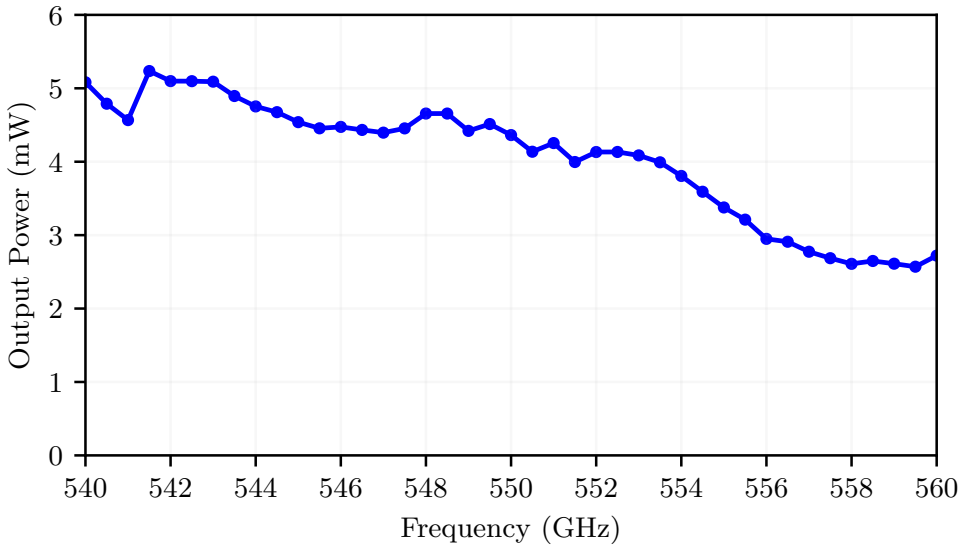

Figure 2.12: Power output of the AMC 702 across its tunable frequency range, as reported by the AMC 702 datasheet.

2.7.1 Microwave Seed Signal

The AMC 702 has a fixed upconversion factor of 36, therefore to generate the required 545 GHz (0.55 THz) field to drive the THz imaging transition, the AMC must be powered by a 15.239 GHz microwave seed signal. We use a Windfreak Synth HD Pro, a compact dual-channel USB microwave signal generator, which produces the 15.239 GHz seed signal at a power output of 13 dBm; the recommended power input for the AMC. The frequency and power settings of the Windfreak are controlled in software on the lab PC.

2.7.2 THz Power Control

To control the power output of the THz source, the AMC can attenuate its power through the User Controlled Attenuation (UCA) port, which accepts an analogue voltage between 0 V and 5 V. The input voltage corresponds to the attenuation level as shown in Figure 2.13.

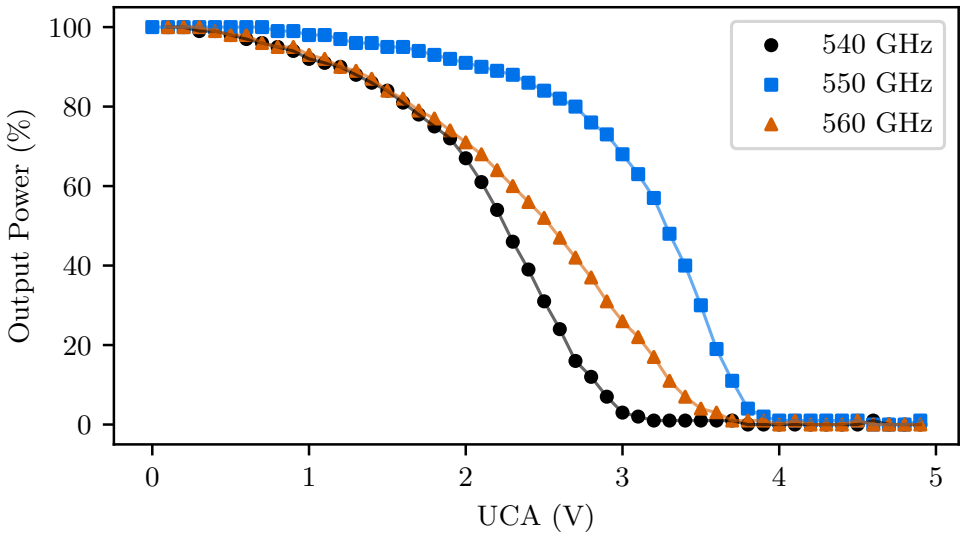

Figure 2.13: Power output of the AMC 702 as a function of the UCA voltage, as reported by the AMC 702 datasheet. The attenuation level is dependent on the operating frequency of the AMC.

The response of the UAC is highly non-linear and dependent on the operating output frequency, therefore knowledge of the power output relies on the manufacturers calibration. For this work, quantitative knowledge of the power output is not strictly required. The important aspect is control over the power output to ensure high signal-to-noise in our images without saturation of the imaging system.

The UCA port is connected and controlled by a National Instruments USB-6001 Multifunction I/O device, which produces the 0-5 V analogue control voltage and is operated via software on the lab PC.

2.7.3 THz Emission and Beam Shaping

The emitted THz field is coupled to free-space through the use of a diagonal feed-horn, which produces a diverging beam with an initial Gaussian $1/e^2$ waist radius of $\omega_0 = 1.3$ mm. The output beam has a half-angle divergence of the beam is 8.45°, with 84% of the output beam being the fundamental Gaussian mode (TEM_{00}). To collimate the beam, a 50 mm diameter, 75 mm focal length aspheric PTFE (Teflon) lens is mounted in-front of the feed-horn. PTFE is an ideal lens material for the THz band, due to its modest refractive index $n = 1.466$ and low absorption [38]. This produces a collimated beam with a Gaussian beam waist of $w = 11.1$ mm. Which is more than sufficient to illuminate the entire vapour cell.

2.8 Image Processing

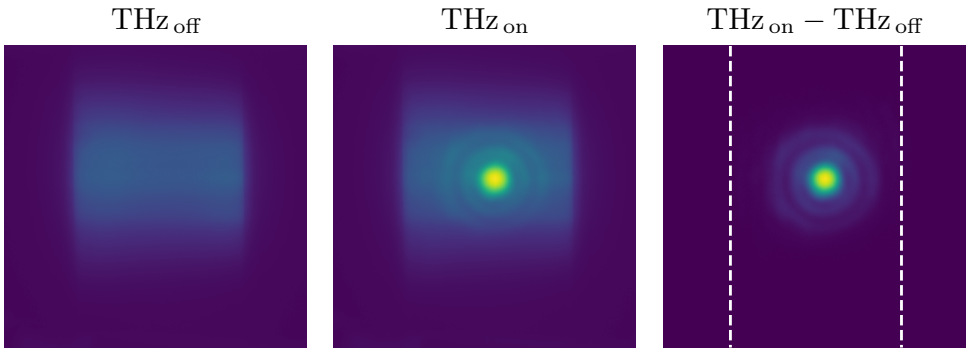

Figure 2.14: Demonstration of the image differencing process to extract the signal fluorescence only. The edge of the vapour cell is highlighted in the final THz image, as the difference image is cropped down to this region. A false colourmap is used for visual clarity of the vapour cell edges.

Generated THz images are composed of two raw images. One $\mathrm{THz}_{\mathrm{off}}$ image where there is no incident THz illumination, and therefore only consists of the background fluorescence. And one $\mathrm{THz}_{\mathrm{on}}$ image, which includes incident THz illumination and is the combination of the background and signal fluorescence. The THz image is therefore the difference between the two frames, $\mathrm{THz}_{\mathrm{on}} - \mathrm{THz}_{\mathrm{off}}$, as shown in Figure 2.14. Typically, a single background image can be used for a large number of sequential $\mathrm{THz}_{\mathrm{on}}$, as fluctuations in the fluorescence varies slowly over large timescales. This allows for fast acquisition of many THz images.

The vapour cell does not take up the entire field of view (FOV) of the camera, therefore the processed THz image is cropped down to the width of the vapour cell. The height of the THz image is also cropped down, so that the final THz image is square. The final cropped THz image therefore encompasses a 10 mm $\times$ 10 mm portion of the vapour cell. Which leads to the THz imaging system having a 10 mm $\times$ 10 mm active THz sensing region.

2.9 Conclusion

In this chapter we have described and discussed the components that must be understood and operated in order to perform atom-based THz imaging. We explained the role of the different optical components required to produce a THz-sensitive vapour of caesium that allows for efficient THz-to-optical conversion, and therefore highly sensitive THz detection and imaging. This leads to the capture of raw fluorescence images that are processed to generate complete THz frames. For the remainder of this thesis work, we shall consider the imaging system to work as presented and use it to implement advanced super-resolution imaging techniques taken from the optical domain.

Chapter 3

Image Resolution

This chapter explores the definitions of image resolution and how it can be quantified. I present various methods considered for determining the spatial resolution of an imaging system and demonstrate these methods experimentally to outline their effectiveness at the THz band. This chapter is used to guide and informed the choice of resolution metric which will be used to assess the success of super-resolution imaging techniques in later chapters.

3.1 Defining Resolution

One of the larger contributing factors to the resolution of an optical system, is how one defines resolution. In many instances, the measure of resolution is better served as a comparative metric rather an absolute one, with the use of a resolution metric ultimately depending on subjective choice.

Development of microscopy and astronomy instrumentation has led to a large range of definitions for resolutions, which are all variations on a theme; how well two neighbouring point sources can be resolved.

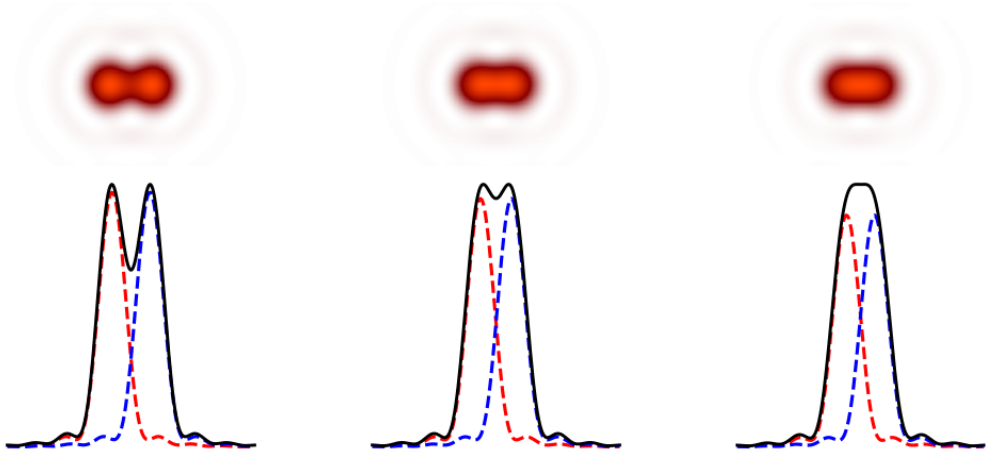

$d = 0.61\frac{\lambda}{NA}$ $d = 0.5\frac{\lambda}{NA}$ $d = 0.47\frac{\lambda}{NA}$

(a) Rayleigh Criterion **(b)** Abbe's Limit **(c)** Sparrow's Limit

Figure 3.1: Comparison on three definition of resolution dervied from considering the overlap of diffraction limited point sources, ordered by decreasing limit magnitude.

3.1.1 Abbe's Limit

Ernst Abbe's Limit, expressed as an equation in 1882 [66], is the earliest wholly theoretical treatment on resolution.

$$d_{\text{Abbe}} = 0.5\ \frac{\lambda}{\text{NA}} \tag{3.1}$$

By applying geometric optics, Abbe's limit considers the *numerical aperture* of a lens, which defines the light collecting power of the lens

$$\text{NA} = n \sin\theta\ . \tag{3.2}$$

Where n is the refractive index of the medium the lens is in ($n \approx 1$ for air) and θ, the half-angle of the maximum cone of light that can enter the lens. This angle determines the resolution limit as it directly influences the numerical aperture, with larger angles yielding higher resolution.

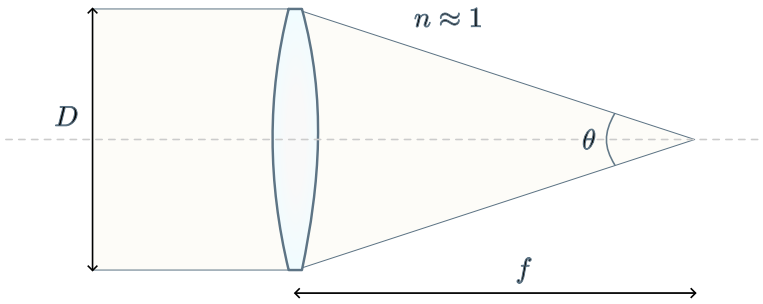

Figure 3.2: Abbe's limit based on simple lens geometry.

Considering the lens geometry shown in Figure 3.2, we can further define numerical aperture by the properties of the lens

$$\mathrm{NA} = n \, \frac{D}{2f} \, . \tag{3.3}$$

With f being the focal length, and D the clear diameter of the lens. Using numerical aperture provides insight into how to design an imaging system with high resolving power.

3.1.2 Rayleigh Criterion

Developed by Lord Rayleigh in the 19th century, the Rayleigh criterion defines resolution as the minimum angular separation at which two point sources of light can be distinctly resolved [67]. Rooted in diffraction theory, the criterion describes the condition where the central maximum of one diffraction pattern overlaps with the first minimum of the other, providing a practical limit for optical resolution.

A typical imaging system will employ circular apertures, leading to the Airy disc diffraction pattern. Therefore the resulting Rayleigh criterion is given

$$\theta = 1.22 \, \frac{\lambda}{D} \, , \tag{3.4}$$

where λ is the wavelength of light, and D is the aperture diameter. The factor 1.22 arises from the first zero of the Bessel function $J_1(x)$, which describes the intensity distribution of the Airy pattern formed by a circular aperture [68].

Using the *small angle approximation*, a lens of focal length f will provide the spatial resolution

$$d_{\text{Rayleigh}} \approx 1.22 \ \frac{f\lambda}{D} = 0.61 \frac{\lambda}{\text{NA}} \tag{3.5}$$

Incorporating the definition of the numerical aperture from Equation 3.3, we find

$$d_{\text{Rayleigh}} = 0.61 \frac{\lambda}{\text{NA}} \tag{3.6}$$

Of the three definitions of resolution, the Rayleigh criterion is the most employed, especially in applications such as microscopy where the imaging system is diffraction-limited.

3.1.3 Sparrow Limit

The Sparrow Limit develops the Rayleigh criterion to provide a more stringent measure of resolution, and was developed for the characterisation of spectral resolving power of spectroscopes/spectrometers [69]. Resolution is defined as the separation of two point-sources, such that there is no reduction in intensity between the two point-sources, leading to a flat intensity profile at the peak.

Assuming circular aperture geometry, and therefore an Airy disc diffraction pattern, the Sparrow Limit is given as

$$d_{\text{Sparrow}} = 0.47 \ \frac{\lambda}{\text{NA}}. \tag{3.7}$$

The Sparrow Limit provides the smallest value for resolution for a given system, out of the three definitions, and is $\frac{1}{\sqrt{2}}$ smaller than the Rayleigh criterion.

3.1.4 Outlook

Going forward in this thesis, the Rayleigh criterion will be used as the chosen resolution metric. While it provides the most conservative estimate of an imaging system's resolution, it serves as a physically meaningful metric that is rooted in wave optics and diffraction theory.

The Rayleigh criterion offers a rigorous standard for comparison, particularly in imaging systems where optical quality approaches the diffraction limit. It establishes a resolution limit — beyond which any further improvement must come from advanced super-resolution imaging techniques.

3.2 System Response Functions

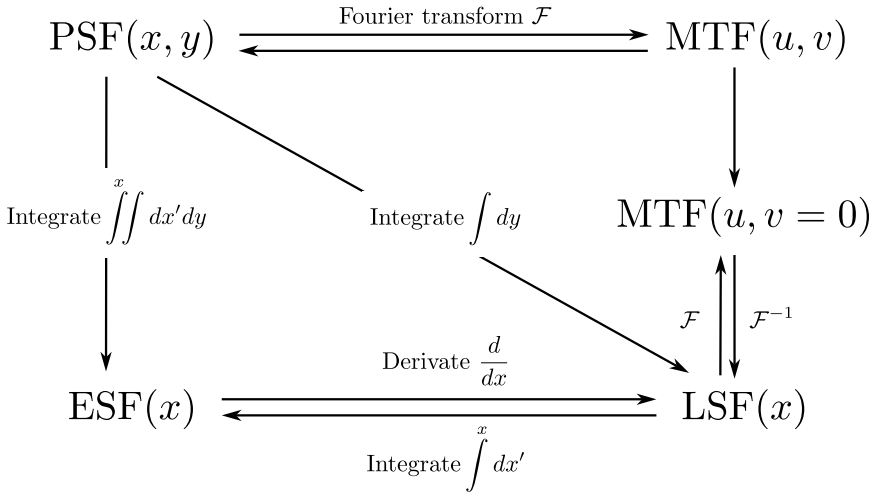

Figure 3.3: Mathematical relationship between various system response functions, including; the point-spread function (PSF), edge-spread function (ESF), line-spread function (LSF) and the modulation transfer function (MTF).

System response functions characterise the behaviour and performance of imaging systems. These functions describe how an imaging system reacts to an given input, such as a point or line, and helps quantify the system's ability to capture, process, and reproduce images. They can be used to provide insights into the resolution, contrast, and overall quality of the system's output.

3.2.1 Point Spread Function

The Point Spread Function (PSF) characterizes the response of an imaging system to a point source. The response represents how such a point of light becomes distributed or "spread" due to the limits of the imaging system such as diffraction, aberrations and detector imperfections. Mathematically, the PSF acts as a convolution kernel in the imaging process, where the observed image is a convolution of the object with the PSF.

The resultant image $I(x, y)$ is therefore

$$I(x, y) = \mathrm{PSF}(x, y) \otimes O(x, y) \ , \tag{3.8}$$

with $O(x, y)$ the object being imaged, $\mathrm{PSF}(x, y)$ the point spread function of the imaging system. We use $\otimes$ to denote the convolution operator.

For a well-performing imaging system, the dominating contribution to the PSF will be diffraction. Such an imaging system is referred to as diffraction-limited. In this case, the ideal PSF is characterized by the Airy function, which describes the diffraction of light through a circular aperture. This is given as,

$$\mathrm{PSF}_{airy}(\mathbf{r}) = I_0 \left[\frac{2J_1(k'r)}{k'r} \right]^2 \quad ; \quad k' = \frac{2\pi}{\lambda} \frac{\mathrm{NA}}{n} \ , \tag{3.9}$$

where $\mathbf{r}$ is the radial coordinate, I_0 a normalization constant, J_1 the Bessel function of the first kind, and k' the effective wavevector of the imaging system, accounting for the illumination wavelength λ, lens numerical aperture NA and refractive index n of the system (typically $n \approx 1$ for air). Figure 3.4 shows how a point-source, under the PSF response of an imaging system generates an Airy disc pattern.

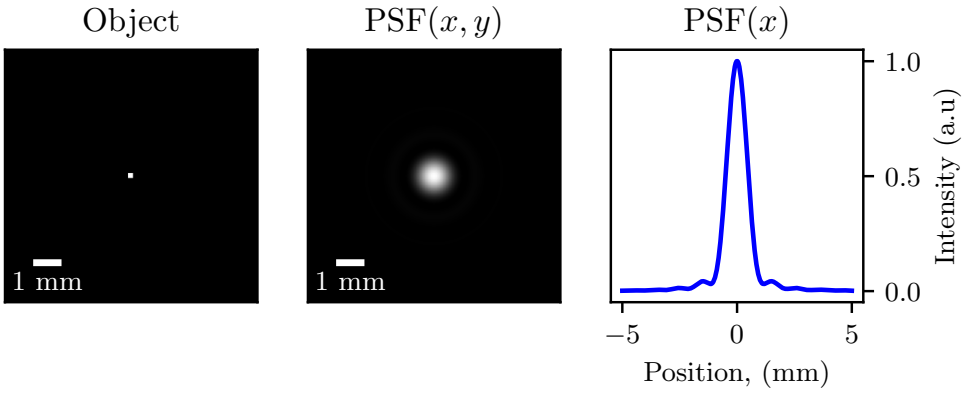

Figure 3.4: Simulation of a THz widefield image of a point-source, leading to an Airy disc pattern. This response is the $\mathrm{PSF}(x, y)$. A 1D profile of the PSF is also shown, demonstrating the characteristic Airy profile; a central peak with two smaller side peaks.

For practical analysis of the system and its resolution, the PSF can be approximated by a Gaussian function with variance σ^2.

$$\mathrm{PSF}_{gauss}(\mathbf{r}) = \exp\left(\frac{-r^2}{2\sigma^2}\right) , \tag{3.10}$$

Figure 3.5 compares the two PSF models, showing that the Gaussian approximation remain valid for the central portion of the Airy disc. The power of the Gaussian PSF model lies in the fact that under differentiation, integration, or the Fourier transform, a Gaussian remains as a Gaussian with appropriately modified parameters. This property enables straightforward derivation of related system response functions, such as the Modulation Transfer Function (MTF).

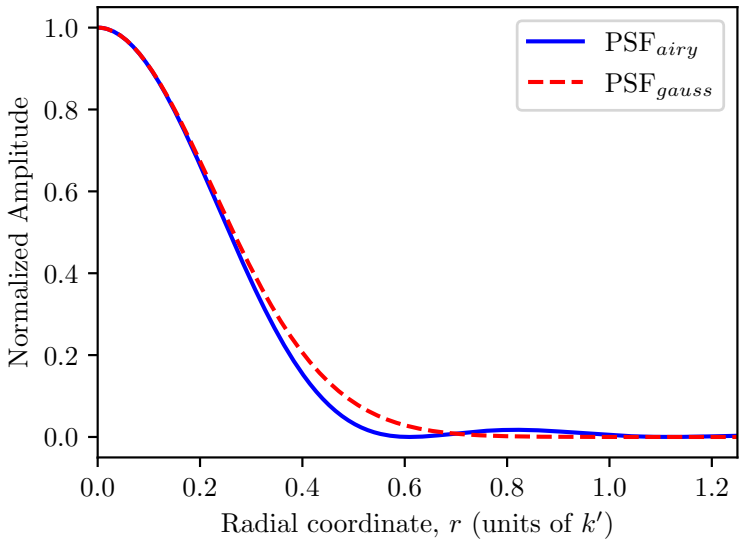

Figure 3.5: Comparison of the ideal Airy PSF and Gaussian PSF approximation. Both profiles are plotting against the normalised radial coordinates for comparison.

3.2.2 Edge Spread Function

The Edge Spread Function (ESF) represents the imaging systems response to an idealised sharp edge; an immediate transition from complete white to complete black, an edge with infinite contrast. It describes how the intensity transitions from one side of the edge to the other, revealing the effects of system limitations from diffraction and aberrations. Mathematically, the ESF is the cumulative integral of the Point Spread Function (PSF) along the direction perpendicular to the edge

$$\mathrm{ESF}(x) = \int_{-\infty}^{\infty} \mathrm{PSF}(x, y)\ dy\ . \tag{3.11}$$

The primary advantage of using the ESF lies in the practicality and simplicity of acquiring data from a sharp edge. Capturing an edge profile of a well-defined, high-contrast edge is easy to produce, image and process accurately.

However, the ESF is inherently one-dimensional, with a single evaluation providing information only about the dimension normal to the edge. This approach is valid for isotropic systems. But for anisotropic systems where the resolution may vary across different directions, such as those with high aberrations, additional measurements are necessary to fully characterize the system's performance.

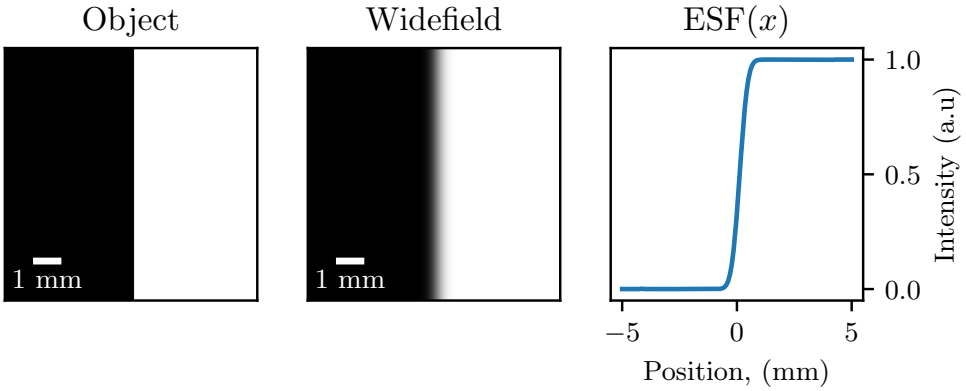

Figure 3.6: Simulation of a THz widefield image when imaging a high-contrast edge. The system's response is to spread and blur edge's transition. The measured perpendicular profile is shown demonstrating the loss of edge contrast.

3.2.3 Line Spread Function

The Line Spread Function (LSF) represents an imaging system's response to an idealised line object, an infinitely narrow, high-contrast line. It describes how the system spreads or blurs this line, revealing the effects of diffraction, aberrations, and other system limitations on spatial resolution along the direction perpendicular to the line.

Mathematically, the LSF is the integral of the Point Spread Function (PSF) over one spatial dimension

$$\mathrm{LSF}(x) = \int_{-\infty}^{\infty} \mathrm{PSF}(x, y)\ dy \tag{3.12}$$

where the integration is along the dimension to the line. Therefore the 2D PSF is collapsed into a 1D function, along a direction normal to the line. Here, Equation 3.12 assumes a horizontal line, and therefore integration along the vertical.

A key advantage of using the LSF is ease of measurement. It can be measured by imaging a slit with a width narrower than the diffraction-limit of the system and analysing the intensity profile perpendicular to the line. However, likewise with ESF, the LSF can only describe the system's response along one axis, and therefore cannot provide an isotropic measurement without repeat measurement at various orientations of the slit. Figure 3.7 shows a simulation of imaging a sub-diffraction wide slit with the resulting perpendicular intensity profile, which is a measurement of the LSF.

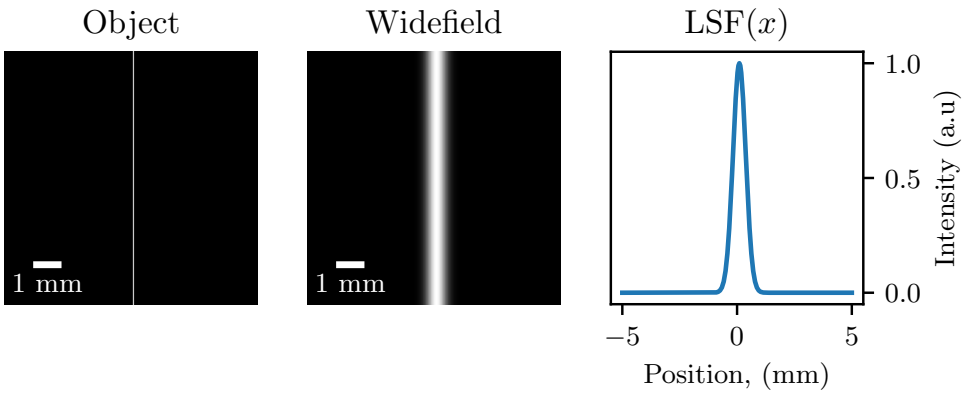

Figure 3.7: Simulation of a THz widefield image when imaging a sub-diffraction slit object. The system's response is to spread and blur the line. The measured perpendicular profile is also shown.

3.2.4 Modulation Transfer Function

The Modulation Transfer Function (MTF) characterizes the spatial frequency response of an imaging system. It describes how effectively various spatial frequencies in an object are transferred to the observed image. The MTF at a given spatial frequency represents the observed contrast associated with that spatial frequency. It provides insight into the system's ability to preserve image detail, including the maximum resolvable spatial frequency, allowing the resolution of a system to be quantified.

Mathematically, the MTF is the magnitude of the Fourier transform of the PSF.

$$\mathrm{MTF}(k) = |\mathcal{F}\{\mathrm{PSF}(r)\}| \ , \tag{3.13}$$

where $\mathcal{F}$ denotes the Fourier transform and k is the spatial frequency and r is the radial respectively. It is assumed in this case, the response of the system is the same in all directions, hence the radially averaged 1D PSF is used.

To determine the resolution from the MTF, we would ideally determine the cut-off frequency of the system, where the MTF of the system reaches zero. Practically, accurately determining the cut-off frequency is difficult as the MTF will have an

associated noise-floor that will dominate before the MTF reaches zero. This makes determination of the true cut-off spatial frequency difficult and unreliable.

Alternatively, we can define a threshold for the MTF. MTF50 is one common metric used, which is the spatial frequency at which the MTF has reached the 50% value. It is widely used in television and digital photography as it provides a good subjective perceptual metric for overall image sharpness [70], yet does not provide a good metric for resolution, in the sense of the absolute cut-off limit.

To consider resolution at its maximal limit, we can consider the MTF10 metric. MTF10 is considered the vanishing resolution limit that correlates with the conditions defined by the Rayleigh criterion [71]. This limit is therefore compatible with other definitions of resolution and can be determined easily as it should remain above the noise-floor of a well made MTF measurement. Both of these metrics are shown on Figure 3.8.

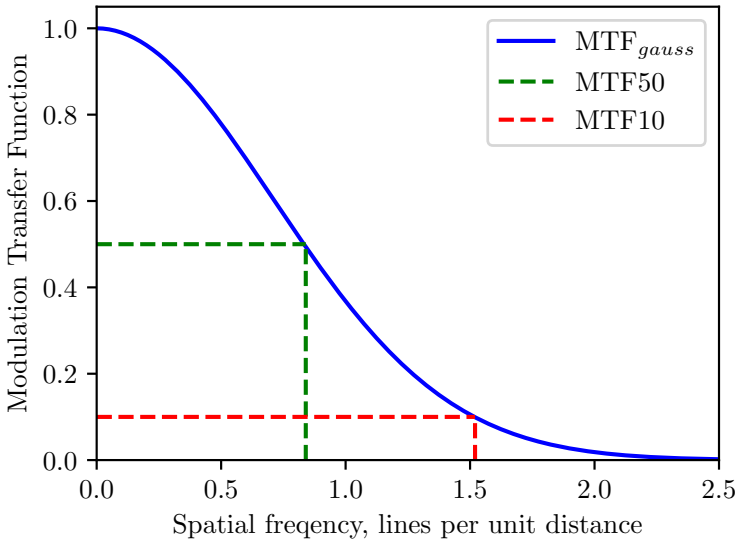

Figure 3.8: MTF curve of the Gaussian model. The common MTF50 and MTF10 resolution metrics are shown.

3.2.5 Outlook

System response functions provide crucial insight into the response of an imaging system, and can be used to draw quantitative measurements on the absolute resolution of the system.

The next section considers various experimental approach to directly measure the Edge Spread Function, Point Spread Function and Modulation Transfer Function of the THz imaging system. These three system response functions were chosen as an example of measurement of a 1D, 2D and Fourier based response function. In this case, measurement of the LSF has not be explored, as it is also a 1D system response function, but could easily be measured as described in Subsection 3.2.3.

3.3 Quantitative Resolution Measurements

Here we will explore a series of approaches to measuring and determining the resolution of our THz imaging system, and then compare and evaluate each method. Each resolution measurement method attempts to provide a quantitative measurement on the resolution limit of the system by directly measuring one of the system response functions. This allows the determination of the system's spatial cut-off frequency, which defines the finest detail the system can resolve. The cut-off spatial frequency, k_{cutoff}, and the system resolution, r_0 are inversely proportional, such that:

$$k_{\text{cutoff}} = \frac{1}{r_0} \tag{3.14}$$

Understanding the diffraction-limited performance of our THz imaging system is an essential baseline to support later super-resolution work.

3.3.1 1951 USAF target

The 1951 United States Air Force (USAF) resolution target (Figure 3.9) is one of many standardised resolution targets used as a basis for determining an imaging systems resolution. For microscopy and super-resolution imaging, the USAF resolution target has become the *de facto* standard. Out of all the methods we shall consider, it is the easiest and quickest method, as it requires no analysis of the taken image. However, in doing so, the USAF target can only provide upper and lower bounds for the resolution of the system. Nevertheless, this makes it a good starting point for quantifying the performance of any imaging system.

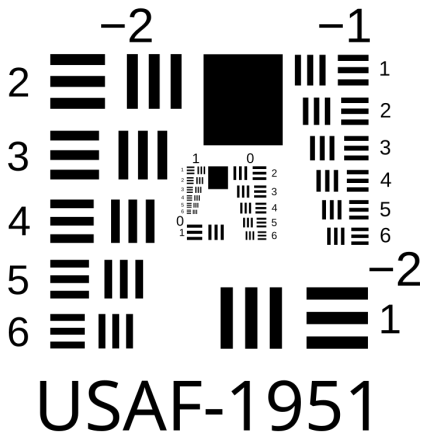

Figure 3.9: 1951 USAF Resolution Target. Attribution Leonhard Wimmer, CC BY-SA 3.0, via Wikimedia Commons

The target contains *groups* of six *elements*. Each group has a corresponding *group number* and each element within a group a corresponding *element number* from 1-6, with 6 denoting the smallest element in a group. The labelling defines the spatial frequency of the vertical and horizontal bars in a element, with a line spacing in lines per millimetre (lp/mm) via

$$\text{spatial frequency (lp/mm)} = 2^{\,\text{group}+(\text{element}-1)/6}. \tag{3.15}$$

The use of the target aims to determine an bounds on the cut-off spatial frequency of a system, and therefore bounds on the system's resolution. By finding the smallest element that can still be resolved, we can determine a lower-bound for the cut-off spatial frequency of our imaging system. The upper-bound is then therefore the spatial frequency of the next smaller element, which cannot be resolved. Therefore the cut-off spatial frequency of the system must reside between the spatial frequency of the two elements. This can be done through simple observation, and therefore requires no analysis of the taken image, which is a key advantage to this method.

USAF resolution targets are typically made from a glass substrate, patterned with a thin-film metal layer. This produces a high contrast target for use in optical imaing. For use in the THz band however, a more suitable choice is copper-clad

FR4 board, a material that is commonly used in making electronic circuit boards. FR4 is a fibreglass composite dielectric substrate that is more transparent than glass at THz frequencies [72]. The 35 μm thin film copper-layer on the other-hand is opaque and highly reflective. Copper-clad FR4 board can be readily machined using a CNC milling machine, allowing for micron sized features to be achieved easily. The produced USAF target for use in the THz is shown in Figure 3.10.

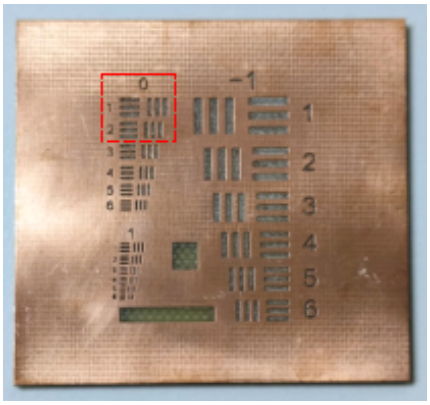

Figure 3.10: Photo of the USAF target manufactured for this work, the top 35 μm layer of copper is removed to produce a positive mask. At 0.55 THz the copper layer reflects the THz illumination whilst the underlying FR4 substrate is transparent, making it an ideal transmissive mask. The Group 0 Elements 1 and 2 which are imaged later are highlighted by the red dashed box.

Previous work [37] has demonstrated that the THz imaging system has a cut-off spatial frequency on the order of 1.00 mm^{-1}. This corresponds to Element 1 in Group 0 on the USAF target, therefore to verify this previous measurement and determine a better bounds of the cut-off spatial frequency, we image Element 1 and Element 2 from Group 0. These elements are highlighted in Figure 3.10 and the resulting widefield image is shown in Figure 3.11.

As can be seen from the widefield image, only Element 1 can be resolved, with clear vertical and horizontal bars. Element 2 is poorly resolved, with the vertical and horizontal bars being undistinguished. Just through this observation alone we can apply the bounds onto the spatial cut-off frequency of the THz imaging system.

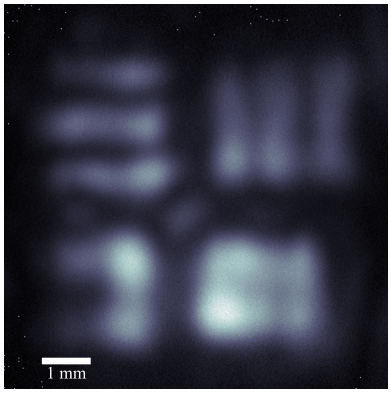

Figure 3.11: Widefield THz image of a portion of the USAF target, corresponding to Group 0, Elements 1 and 2. A 1 mm scale bar is included.

$$1.00 \text{ mm}^{-1} \leq k_{\text{cutoff}} < 1.12 \text{ mm}^{-1}$$

Where the lower-bound is derived from the spatial frequency of the resolved bars of Element 1, and the upper-bound is derived from the spatial frequency of the unresolved bars of Element 2. Using Rayleigh's criteria, we can further derive bounds for the system's *effective* numerical aperture which will prove useful for later simulations and design.

$$0.332 \leq \text{NA}_{\text{eff}} < 0.352$$

3.3.2 Single pinhole

A pinhole can be used to approximate, to good order, a point source when the diameter of the pinhole is smaller than the diffraction limit of the imaging system. Imaging such pinhole, can allow for a measurement of the system's point-spread function. For a non-aberrated imaging system, the resulting image will be the Airy disc profile (Equation 3.9) [68].

We can anticipate the size of the pinhole required by considering Rayleigh's criteria (Equation 3.6). Using our earlier estimate of the effective numerical aperture estimate of $\mathrm{NA}_{\mathrm{eff}} = 0.35$ and the illumination wavelength of $\lambda = 545$ μm, our pinhole must be sized on the order of $d_{\mathrm{pinhole}} \ll d_{\mathrm{rayleigh}} \approx 950$ μm. Therefore we opted to use a 250 μm pinhole, which was illuminated by the collimated THz illumination.

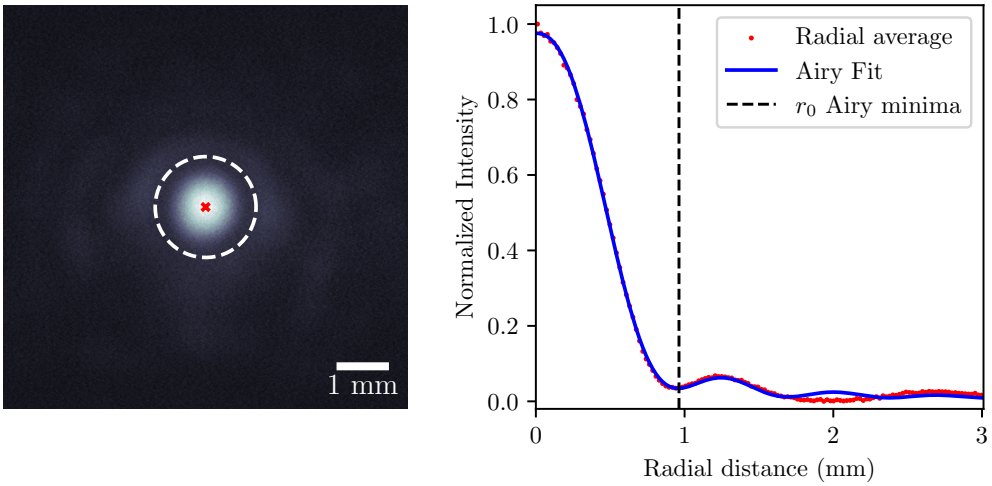

Figure 3.12: Measurement of the PSF through imaging a single pinhole. (Left) The widefield image of the resulting diffraction pattern through the pinhole, the center of the pinhole is marked by the red dot and the first Airy minima by the white dashed circle. (Right) The mean radial profile of the pinhole with a fitted Airy function, which is used to determine the resolution of the system.

The resultant widefield image of the pinhole, and the mean radial profile of the pinhole's diffraction pattern is shown in Figure 3.12. The widefield image shows the characteristic Airy disc pattern, demonstrating the pinhole is sufficiently small to behave as a point-source.

To characterize the resolution, the Airy diffraction profile (Equation 3.9) is fitted to the mean radial profile, allowing extraction of r_0, the position of the first Airy minimum. By definition of the Rayleigh criteria, the first Airy minium corresponds to the resolution of the system. Here, $r_0 = 0.96 \pm 0.03$ mm, where the uncertainty is derived from the uncertainty in the fit parameters of the Airy diffraction profile. This corresponds to a cut-off spatial frequency of $k_{\text{cutoff}} = 1.04 \pm 0.03$ mm^{-1}, which is within the bounds determined by the USAF resolution target.

3.3.3 Slanted Edge Method

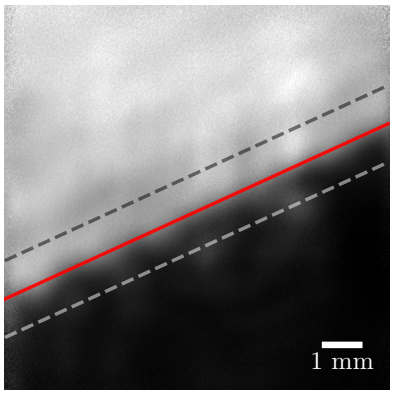

Figure 3.13: THz widefield image of a slanted edge. The red line denotes the leading edge and the centre position for sampling. The adjacent dashed lines indicate the sampling region of interest.

The slanted edge method aims to measure the Edge Spread Function (ESF) and subsequently derive the Modulation Transfer Function (MTF) of the system, and is a standardised method under ISO 12233 [73]. It involves capturing a widefield image of a slanted knife-edge, and measuring the gradient on the transition from black to white. The angled position ensures the knife edge does not align to the imaging sensors pixel grid so that the knife-edge transition can be over-sampled by the imaging sensor. This prevents aliasing artifacts in the image that arises from poor sampling [74]. By sampling perpendicular to the knife edge, the transition in contrast can be measured. This profile, by definition, is the ESF of the system.

Through the relationship between system response functions (Figure 3.3) we can

derive the Line Spread Function (LSF) by differentiation of the ESF, and then the MTF can be derived through the Fourier transform of the LSF. With the MTF, the system's spatial cut-off frequency and therefore resolution limit can be determined. This method provides a practical and reliable assessment of spatial resolution, as the imaging target is simple and easy to construct. The method is applicable for almost any imaging system and has been used in infrared [75], x-ray [76] and neutron imaging [77].

For THz imaging, a simple metal knife edge provides excellent contrast and fits easily into the camera's field of view. Figure 3.13 shows a widefield image of a knife edge in our THz imaging system. The transition line is highlighted in red, and the sampling region of interest is bound by the two dashed lines.

The intensity value of each pixel within the sampling region is plotted as a function of perpendicular distance from the transition line, as show in Figure 3.14. The mean profile could then be calculated before the Gaussian error function is fitted. We chose the error function to model the ESF, as we can analytically derive the MTF through the described relation,

$$\begin{aligned} \mathrm{MTF}(k) &= \mathcal{F}\left\{\frac{d}{dx}\mathrm{ESF}(x)\right\} \\ &= \mathcal{F}\left\{\frac{d}{dx}\,\mathrm{erf}(x,\sigma)\right\} \\ &= \mathcal{F}\left\{\,\mathrm{gaussian}(x,\sigma)\,\right\} \\ &= e^{-\pi^2 k^2 \sigma^2}\,. \end{aligned} \tag{3.16}$$

Where $\mathcal{F}$ denotes the Fourier transform, and σ is the standard deviation of the Gaussian function, and therefore the 'sharpness' parameter of the ESF. We can therefore determine an analytical Gaussian model of the MTF directly from the fit parameters of the error function. This allows the spatial cut-off frequency of the system to be analytically determined by calculating the MTF10 value, corresponding to the Rayleigh resolution (as show in Figure 3.14).

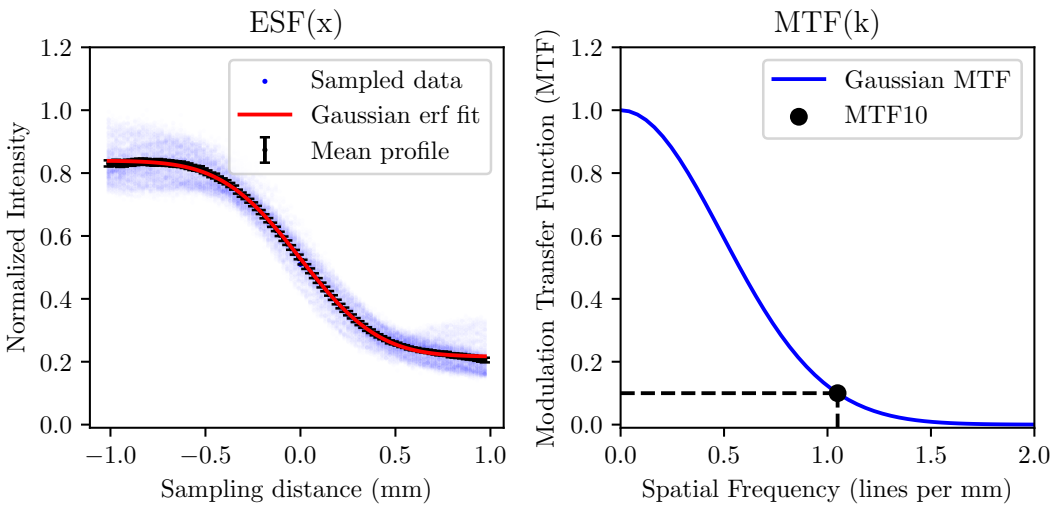

Figure 3.14: (Left) Experimental data taken from the slanted edge, many perpendicular samples are taken to generate a mean profile of the Edge Spread Function, ESF(x). A Gaussian error function model is fitted to the mean profile. (Right) The resultant Modulation Transfer Function, MTF(k). The MTF is a Gaussian as it is the derivative of the fitted ESF model. Using this Gaussian model of the MTF, the MTF10 value is determined to be $k_{\text{cutoff}} = 1.05 \pm 0.01$ mm^{-1}.

Using Equation 3.16 and our ESF fit parameters, we can determine the cut-off spatial frequency k_{cutoff}, such that MTF(k_{cutoff}) = 0.10. This results in a spatial cut-off frequency of $k_{\text{cutoff}} = 1.05 \pm 0.01$ mm^{-1} which corresponds to a resolution limit of $r_0 = 0.95 \pm 0.01$ mm.

3.3.4 Siemen Star

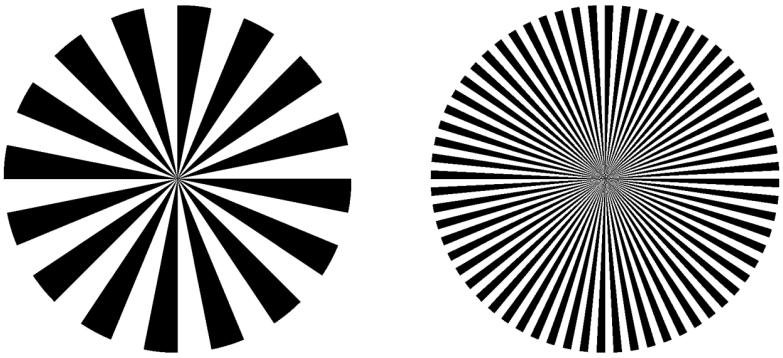

(a) 16 spokes **(b)** 64 spokes

Figure 3.15: Two Siemen stars with differing number of spokes, offering a different range of spatial frequencies that can be resolved and analysed.

The Siemen star (Figure 3.15) is an image target used to directly reconstruct the MTF of an imaging system. Made from alternating black and white spokes emanating from a central point, the Siemen star hosts a range of spatial frequencies that can be sampled by concentric sampling circles of radius, r. The sampled spatial frequency, k, is given by

$$k(r) = \frac{N}{2\pi r}, \tag{3.17}$$

where N is the number of (black) spokes the target has. The MTF will affect the contrast of the spokes fringes at different sampling radii, as the spatial frequency differs. By measuring the average fringe contrast for a given sampling circle, the MTF value at the corresponding spatial frequency can be determined. Sampling circles with smaller radii probe higher spatial frequencies which will exhibit lower fringe contrast as they are attenuated more by the system's MTF. At the spatial cut-off frequency of the system, the fringe contrast is zero as we reach the system's limit to resolve finer detail. Sampling across multiple radii, and therefore spatial frequencies, allows the reconstruction of the MTF.

For the Siemens Star target, the modulation contrast, also known as the Michelson contrast [78] or *visibility* is used, which is given as:

$$C = \frac{I_{\max} - I_{\min}}{I_{\max} + I_{\min}} . \tag{3.18}$$

Where I_{max} is the peak intensity value of a white spoke, and I_{min} the minimum intensity value of a black spoke. For N spokes, a total of $2N$ contrast values can be calculated, allowing for determination of the mean average and uncertainty in the contrast.

Selecting the number of spokes N is an important choice to ensure the measured MTF is well sampled across the relevant spatial frequency range. Too few spokes results in poor sampling at high spatial frequencies, whereas too many spokes will quickly sample spatial frequencies beyond the cut-off frequency of the MTF, resulting in a large portion of the target with zero fringe-contrast. Figure 3.16 shows an ideal case where only the smallest sampling radii have near-zero fringe contrast.

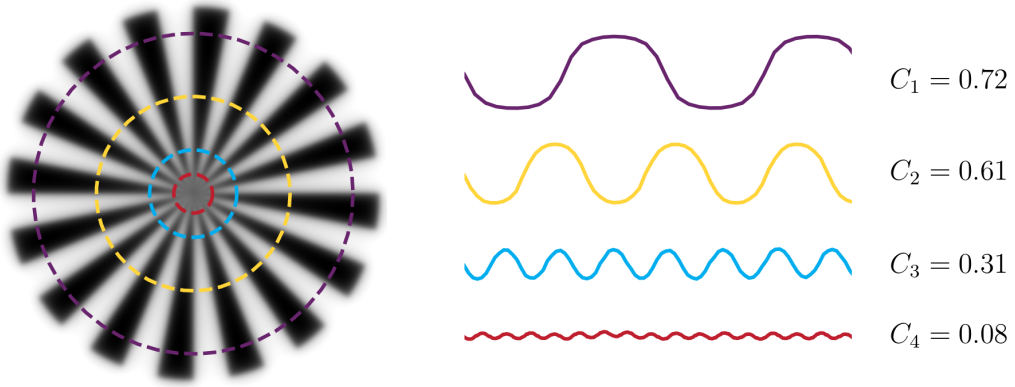

Figure 3.16: Sampling demonstration for a 16 spoke Siemen star that has been attenuated by an ideal MTF. Concentric circles sample increasing spatial frequencies with decreasing radii. For each sampling the fringe profile is shown with its calculated fringe contrast value.

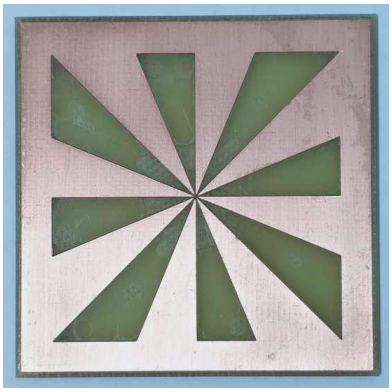

Figure 3.17: THz Siemen Star target with 8 spokes, manufactured from copper-clad FR4 board for this thesis. The number of spokes is optimized to sample across the expected MTF spatial frequency range.

For our THz imaging system, a $N = 8$ Siemens star target was produced by CNC milling FR4 copper-clad board, as shown in Figure 3.17. This produces a large range of spatial frequencies that can be sampled within the THz imagers field of view, which has a maximum sampling radius of $r = 5$ mm.

The target is placed at the imaging plane of the THz imaging lens with the THz illumination centred onto the centre of the Siemens star. The produced widefield image is shown in Figure 3.18, with annotations for the estimated centre-point of the star and the smallest ($r = 1.75$ mm) and largest ($r = 4.85$ mm) radii sampling circles used during analysis. The lower radii bound was chosen as the fringe contrast at lower radii quickly dropped to zero. The range of radii means a sampling spatial frequency range $0.26\ \text{mm}^{-1} \leq k \leq 0.73\ \text{mm}^{-1}$.

Fifteen sampling circles, of equally spaced radii, were used to cover between the upper and lower radii limits. For each of the sampling circles, the mean average contrast and standard error was calculated. The number of sampling circles was chosen to minimise the standard error in each measurement. The resulting contrast values are shown in the right-hand plot of Figure 3.18.

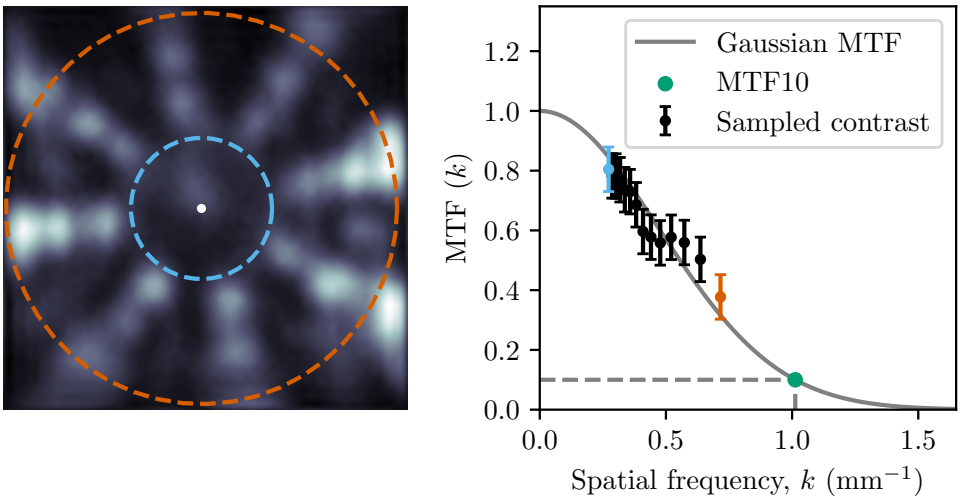

Figure 3.18: (Left) Widefield THz image of the N=8 Siemen star target, annotated with the center point, the smallest (blue) and largest (red) radii sampling circles. (Right) The measured MTF contrast values from each subsequent sampling radii, the two contrast values from the two shown radii extremes are colour coded accordingly. A Gaussian MTF model is fitted to the data and is used to evaluate the MTF10 value.

Like the slanted edge method, we fit the Gaussian MTF model to the data. From there, we can deduce the cut-off spatial frequency from the MTF10 level, this is indicated on the plot and resulting in a value of $k_{\text{cutoff}} = 1.01 \pm 0.23$ mm^{-1} which corresponds to a resolution of $r_0 = 0.99 \pm 0.24$ mm.

This follows the previous resolution measurements, but with significantly higher uncertainty as a result of the poorer fitting of the Gaussian MTF model, which is a result of the high uncertainty in each measured contrast value. This due to several factors. Firstly, the target needs to be uniformly illuminated, such that the contrast between of all spokes are equal. In our widefield image, this is clearly not the case, with some spokes being brighter than others. This effect is partially negated through the use of Michelson contrast, which accounts for the relative contrast between spokes, but this is still not ideal to ensure a tightly distributed set of contrast values per sampling circle.

Second, there is clear unwanted structured in the widefield image, especially in the form of dark bands along the illuminated spokes. This is a result of interference of

the coherent illumination. The interference is exacerbated by the THz illumination readily diffracting at the centre of the target, which is due to the spacing between the spokes approaching the scale of the illumination wavelength. As a result, the centre portion of the target acts as a diffraction grating. This could be negated by blocking the centre portion of the target with an annulus, which would reduce diffraction effects and potentially allow for smaller sampling circles to probe higher spatial frequencies.

Overall, the Siemens star target provides insight into the MTF of the THz imaging system with, in this instance, providing a spatial cut-off frequency measurement that broadly aligns with the other measurement methods. In order to provide a reliable measurement of the spatial cut-off frequency, a better design of such target for use in THz imaging is required. With a design to reduce diffraction and interference from coherent illumination, while still probing the appropriate spatial frequencies needed to reconstruct the MTF.

3.3.5 Comparison

Table 3.1: Comparison of the quantitative resolution measurements used to determine the widefield imaging performance of the THz imaging system.

Method	$\mathbf{k_{cut\text{-}off}}$ **(mm^{-1})**	**Resolution $\mathbf{r_0}$ (mm)**
USAF Target	$1.00 \leq k < 1.12$	$0.89 < r \leq 1.00$
Single Pinhole	1.04 ± 0.03	0.96 ± 0.03
Slanted Edge	1.05 ± 0.01	0.95 ± 0.01
Siemens Star	1.01 ± 0.23	0.99 ± 0.24

Table 3.1 summaries the measured cut-off spatial frequency and resolution for each explored method. All methods show consistent resolution values within their standard errors, except for the Siemens target, and therefore demonstrates good agreement to high precision. This provides confidence in the determined resolution values.

Since all measurements show good agreement, the slanted edge method results will be used to characterize the THz imaging system due to their lowest uncertainty.

Therefore the spatial cut-off frequency and spatial resolution of the THz imaging system will be taken as $k_{\text{cutoff}} = 1.05 \pm 0.01$ mm^{-1} and $r_0 = 0.95 \pm 0.01$ mm respectively. The effective numerical aperture can also be calculated to be $\text{NA}_{\text{eff}} = 0.35 \pm 0.01$.

3.4 Conclusion

To conclude, this chapter discussed how the resolution of an imaging system ultimately depends on the definition used, with the Rayleigh criterion being chosen due to its foundation in diffraction theory.

The chapter explored the concept of System Response Functions, which define how an imaging system responds or transforms an input. These definitions were tied to Rayleigh's definitions of resolution. This allowed the exploration of different methods for measuring the various system response functions directly, and make a determination of the spatial cut-off frequency of the THz imaging system and therefore a determination on the spatial resolution.

These methods were compared on their effectiveness, noting that all methods with the exception of the Siemen Star approach allowed for reliable measurement of resolution. This will provide a good baseline for the next chapters where were explore super-resolution imaging.

Chapter 4

Structured Illumination Super-Resolution Imaging

This chapter explores the concept of structured illumination super-resolution imaging and the Fourier-based mathematics behind how a structured illumination enables an imaging resolution that exceeds the diffraction limit. I then present simulation work that shows the technique remains feasible at the THz band, before demonstrating how to implement the technique experimentally.

4.1 The Structured Illumination Concept

Super-resolution imaging through structured illumination was first conceived by Gustafsson in 2000 [46] for use in microscopy, demonstrating a two-fold resolution improvement over conventional wide-field imaging and therefore beating the diffraction limit. Now known as Structured Illumination Microscopy, SIM has had a profound impact on fluorescence microscopy, enabling high-resolution imaging of live cells with low phototoxicity and fast acquisition speeds, making it a crucial tool for studying dynamic biological processes at the subcellular level [79, 80]. While SIM becomes a misnomer when used outside the context of microscopy, we shall refer to the technique as such for clarity.

SIM is easy to understand conceptually, as it is the application of the moiré effect.

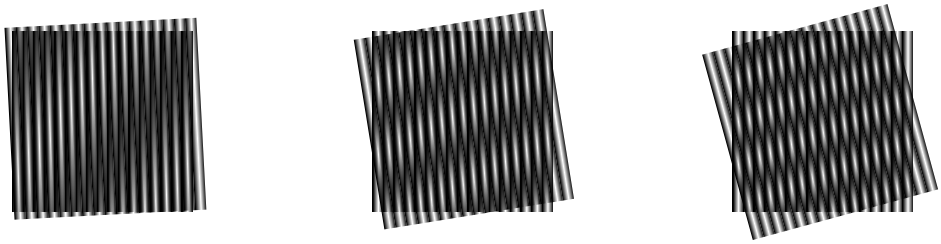

Figure 4.1: Moiré fringes from two similar patterns at differing angles. The change in angle shows different generated spatial frequency fringes through spatial frequency beating.

When two fine pattern are superimposed on top of each other, their (multiplicative) overlap results in a spatial frequency beat pattern, known as moiré fringes. For the case in Figure 4.1, moiré fringes can be generated from two identical patterns overlapping with an orientation offset. A larger offset angle resulting in finer moiré fringes. Overall, the moiré fringes that are produced have much coarser detail than either of the two overlapping input patterns. For an imaging system where the detail of either (or both) input patterns are too fine to be resolved, the much coarser moiré fringes may be. Therefore the moiré fringes encode the finer unresolvable detail of the input patterns, which are made accessible through resolvable coarser fringes. To recover this fine, high resolution information about our sample object, the structure of our patterned illumination must be precisely known.

4.2 Theory

For any widefield imaging system, the formed image at our detector plane, $D(\mathbf{r})$ is

$$D(\mathbf{r}) = [S(\mathbf{r}) \cdot I(\mathbf{r})] \otimes H(\mathbf{r}) + N(\mathbf{r}) \ . \tag{4.1}$$

Where $\mathbf{r} \equiv (x, y)$ is the spatial position vector, and $\otimes$ is the 2D convolution operator. $S(\mathbf{r})$ is the sample object being imaged, and $I(\mathbf{r})$ is the incident illumination on the sample. $S(\mathbf{r}) \cdot I(\mathbf{r})$ therefore represents the optical response of the illuminated sample, which may occur through transmission, reflection, or fluorescence.

$H(\mathbf{r})$ is the Point Spread Function (PSF) of the imaging system, defining how the optical response information is transformed as it passes through the system. $N(\mathbf{r})$ is the cumulative additive Gaussian noise, associated with stochastic processes in the imaging process, primarily arising from detector read-out noise. We can understand the imaging equation schematically in Figure 4.2.

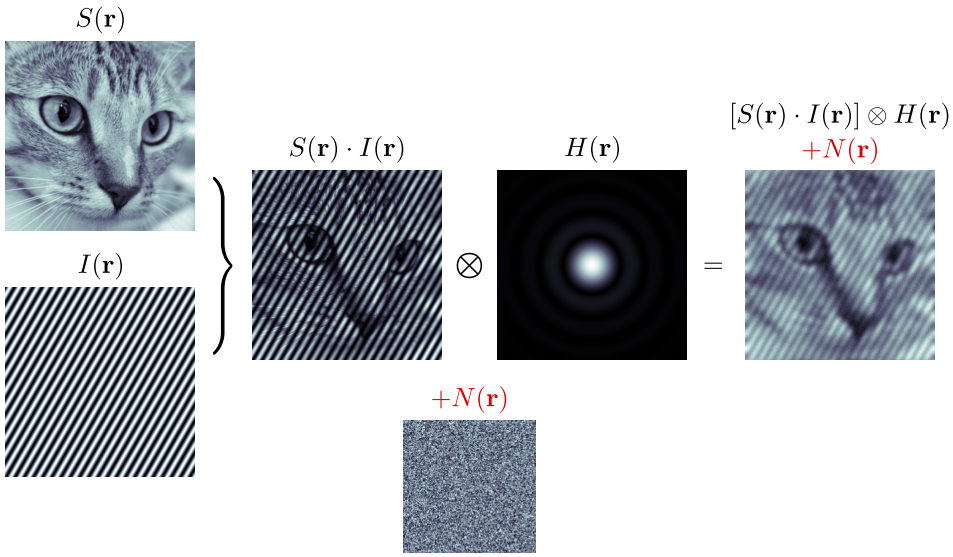

Figure 4.2: Pictorial representation of the *imaging equation* as define by Equation 4.1 when applied with a sinusoidal structured illumination and convolved with an example point spread function.

This *imaging equation* (Equation 4.1) serves as the starting point to understand the SIM concept. Ultimately the power of the SIM technique lies in the structured illumination incident on the sample. Traditionally, SIM uses a sinusoidal patterned illumination:

$$I_{\theta,\phi}(\mathbf{r}) = I_0 \left[1 - \frac{1}{2}\cos\left(2\pi \mathbf{p}_\theta \cdot \mathbf{r} + \phi\right)\right] . \tag{4.2}$$

Here $\mathbf{p}_\theta \equiv (p{\cdot}\cos\theta,\ p{\cdot}\sin\theta)$ is the spatial frequency vector of the sinusoidal illumination and I_0 is the peak intensity of the illumination. The illumination is defined by two angles: θ, which sets the orientation of the illumination pattern, and ϕ, the phase of the illumination. To avoid the need for 'negative-light', the illumination

includes a DC offset, ensuring that the intensity remains strictly positive across the field of view.

In order to recover the higher resolution information encoded within the generated moiré patterns, we must move from the *real space domain* to the *spatial frequency domain* by taking the Fourier transform. This is essential, as it allows for the separation of the various spatial frequency components which are needed to reconstruct our super-resolution image. For our Fourier transformed quantities, we denote them with a tilde $\sim$ and note the change of variable $\mathbf{r} \rightarrow \mathbf{k}$ from the spatial coordinate to the spatial frequency coordinate.

The Fourier transform of our *imaging equation* is given as:

$$\tilde{D}_{\theta,\phi}(\mathbf{k}) = \left[\tilde{S}(\mathbf{k}) \otimes \tilde{I}_{\theta,\phi}(\mathbf{k})\right] \cdot \tilde{H}(\mathbf{k}) + \tilde{N}(\mathbf{k}) \ , \tag{4.3}$$

where $\tilde{S}(\mathbf{k})$ is the Fourier spectrum of the object, $\tilde{I}_{\theta,\phi}(\mathbf{k})$ is the Fourier spectrum of the illumination , $\tilde{H}(\mathbf{k})$ is the Optical Transfer Function (OTF) of the system and $\tilde{N}(\mathbf{k})$ is the noise.

We note that under a Fourier transform, multiplication in real space corresponds to convolution in Fourier space, and *vice versa*. Therefore in the Fourier domain, the object $\tilde{S}(\mathbf{k})$ and illumination $\tilde{I}_{\theta,\phi}(\mathbf{k})$ undergo a convolution with each other leading to moiré-like spatial frequency mixing.

In the Fourier domain, our structured illumination is given as,

$$\tilde{I}_{\theta,\phi}(\mathbf{k}) = \frac{I_0}{2}\left[\delta(\mathbf{k}) + \frac{1}{2}\delta(\mathbf{k}+\mathbf{p}_\theta)e^{i\phi} + \frac{1}{2}\delta(\mathbf{k}-\mathbf{p}_\theta)e^{-i\phi}\right] \ , \tag{4.4}$$

where $\delta(\mathbf{k})$ arises from the DC component of the illumination, and $\delta(\mathbf{k} \pm \mathbf{p}_\theta)e^{\pm i\phi}$, from the cosine component.

Pairing the structured illumination with our imaging equation (combining Equation 4.3 with Equation 4.4) we find,

$$\tilde{D}_{\theta,\phi}(\mathbf{k}) = \frac{I_0}{2}\left[\tilde{S}(\mathbf{k}) + \frac{1}{2}\tilde{S}(\mathbf{k}+\mathbf{p}_\theta)e^{i\phi} + \frac{1}{2}\tilde{S}(\mathbf{k}-\mathbf{p}_\theta)e^{-i\phi}\right]\cdot\tilde{H}(\mathbf{k}) + \tilde{N}(\mathbf{k}) \ , \quad (4.5)$$

Here, our detected image is the result of a linear combination of spatial frequency content bands; a central unshifted band $\tilde{S}(\mathbf{k})\tilde{H}(\mathbf{k})$ and two shifted bands $\tilde{S}(\mathbf{k} \pm \mathbf{p}_\theta)\tilde{H}(\mathbf{k})$. This is a consequence of the convolution shifting property of the δ-function (see Appendix A). We therefore have encoded higher spatial frequency information, from the shifted Fourier bands, into our detected widefield image. Subsequent steps will explain how we can recover this encoded information to reconstruct a super-resolution image.

4.2.1 Fourier Band Separation

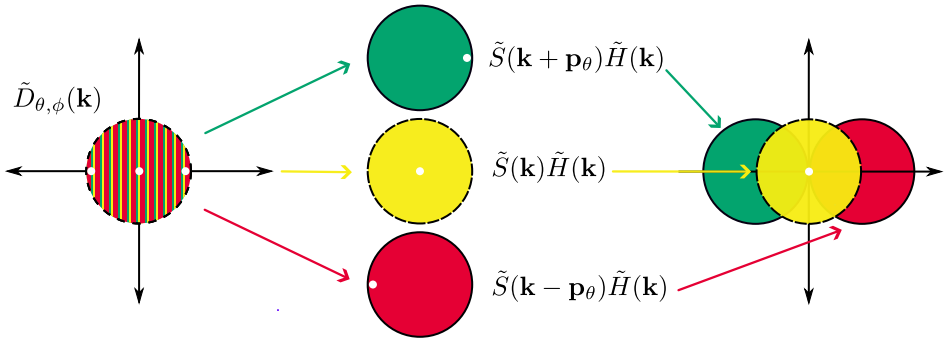

Figure 4.3: SIM reconstruction schematic. The detected image $\tilde{D}_{\theta,\phi}(\mathbf{k})$ is a linear combination of three shifted Fourier bands, that once separated can be combined to produce a Fourier spectrum of increased extent.

The aim of the reconstruction process is to successfully separate the three, currently overlapping, Fourier bands $\tilde{S}(\mathbf{k})$, $\tilde{S}(\mathbf{k}+\mathbf{p}_\theta)$ and $\tilde{S}(\mathbf{k}-\mathbf{p}_\theta)$ from our recorded image $\tilde{D}_{\theta,\phi}(\mathbf{k})$. These separated Fourier bands can then be accurately shifted to their correct locations and combined to reconstruct a larger Fourier spectrum of our sample, including higher spatial-frequency content and therefore producing an image with enhanced resolution.

To solve for the three distinct Fourier bands, we can use Equation 4.3 with its free parameter ϕ, the phase of the illumination, to form a set of three linear equations. Using matrix notation,

$$\begin{bmatrix} \tilde{D}_{\theta,\phi_1}(\mathbf{k}) \\ \tilde{D}_{\theta,\phi_2}(\mathbf{k}) \\ \tilde{D}_{\theta,\phi_3}(\mathbf{k}) \end{bmatrix} = \frac{I_0}{2} \underbrace{\begin{bmatrix} 1 & \frac{1}{2}e^{i\phi_1} & \frac{1}{2}e^{-i\phi_1} \\ 1 & \frac{1}{2}e^{i\phi_2} & \frac{1}{2}e^{-i\phi_3} \\ 1 & \frac{1}{2}e^{i\phi_3} & \frac{1}{2}e^{-i\phi_2} \end{bmatrix}}_{\mathbf{M}} \begin{bmatrix} \tilde{S}(\mathbf{k})\tilde{H}(\mathbf{k}) \\ \tilde{S}(\mathbf{k}+\mathbf{p}_\theta)\tilde{H}(\mathbf{k}) \\ \tilde{S}(\mathbf{k}-\mathbf{p}_\theta)\tilde{H}(\mathbf{k}) \end{bmatrix} + \begin{bmatrix} \tilde{N}_1(\mathbf{k}) \\ \tilde{N}_2(\mathbf{k}) \\ \tilde{N}_3(\mathbf{k}) \end{bmatrix} \tag{4.6}$$

To recover the three distinct bands requires three images of the sample, under structured illumination with differing phases. Typically the chosen phases are equidistant with $\phi_1 = 0$, $\phi_2 = \frac{2\pi}{3}$ and $\phi_3 = \frac{4\pi}{3}$.

Solving the system of equations, under the matrix notation, requires the inverse matrix $\mathbf{M}^{-1}$.

$$\begin{bmatrix} \tilde{S}(\mathbf{k})\tilde{H}(\mathbf{k}) \\ \tilde{S}(\mathbf{k}+\mathbf{p}_\theta)\tilde{H}(\mathbf{k}) \\ \tilde{S}(\mathbf{k}-\mathbf{p}_\theta)\tilde{H}(\mathbf{k}) \end{bmatrix} = \mathbf{M}^{-1} \begin{bmatrix} \tilde{D}_{\theta,\phi_1}(\mathbf{k}) \\ \tilde{D}_{\theta,\phi_2}(\mathbf{k}) \\ \tilde{D}_{\theta,\phi_3}(\mathbf{k}) \end{bmatrix} \tag{4.7}$$

For now, we have ignored the noise terms, which can be accounted for with later processing. It has been shown that $\mathbf{M}^{-1}$ has the analytical solution [81]

$$\mathbf{M}^{-1} = \frac{1}{\Delta} \begin{bmatrix} e^{i\Delta\phi_{23}} - e^{-i\Delta\phi_{23}} & e^{i\Delta\phi_{31}} - e^{-i\Delta\phi_{31}}) & e^{i\Delta\phi_{21}} - e^{-i\Delta\phi_{21}} \\ 2(e^{i\phi_3} - e^{i\phi_2}) & 2(e^{i\phi_1} - e^{i\phi_3}) & 2(e^{i\phi_2} - e^{i\phi_1}) \\ 2(e^{-i\phi_3} - e^{-i\phi_2}) & 2(e^{-i\phi_1} - e^{-i\phi_3}) & 2(e^{-i\phi_2} - e^{-i\phi_1}) \end{bmatrix} \tag{4.8}$$

where

$$\Delta = e^{i\Delta\phi_{21}} - e^{-i\Delta\phi_{21}} - e^{i\Delta\phi_{31}} + e^{-i\Delta\phi_{21}} + e^{i\Delta\phi_{32}} + e^{-i\Delta\phi_{32}}$$

$$\Delta\phi_{23} = \phi_2 - \phi_3$$

$$\Delta\phi_{31} = \phi_3 - \phi_1$$

$$\Delta\phi_{21} = \phi_2 - \phi_1$$

4.2.2 Deconvolution

Through the inverse, $\mathbf{M}^{-1}$, we can solve the system of equations and separate the three distinct Fourier bands. Each band, while separated, is attenuated by the OTF of system, which reduces the amplitudes of the higher spatial frequencies in the band. This leads to suppression of finer details and therefore limits the resolution. Therefore, in order to achieve a two-fold improvement in resolution, a deconvolution step is employed to recover the attenuated spatial frequencies in each Fourier band.

However, the convolution operator in non-invertible, that is, it has no direct inverse. As a result, deconvolution is instead approximated through algorithmic techniques.

$$\tilde{S}(\mathbf{k}) = \text{deconvolve}\left\{ \tilde{S}(\mathbf{k})\tilde{H}(\mathbf{k}) \right\} , \tag{4.9}$$

$$\tilde{S}(\mathbf{k} \pm \mathbf{p}_\theta) = \text{deconvolve}\left\{ \tilde{S}(\mathbf{k} \pm \mathbf{p}_\theta)\tilde{H}(\mathbf{k}) \right\} . \tag{4.10}$$

These algorithms attempt to estimate the non-attenuated signal when provided with an estimate of the Optical Transfer Function. Many deconvolution algorithms have been adapted and demonstrated for the use in SIM [82–86] including Wiener filtering [87] and the Richardson-Lucy algorithm [88]. These algorithms also provide a denoising effect, which helps suppress noise present in the Fourier bands that we ignored during the band separation step.

4.2.3 Band Shifting

Before each Fourier band can be combined to form a super-resolution image, each band must be properly shifted to its true positions. For $\tilde{S}(\mathbf{k} \pm \mathbf{p}_\theta)$ the true position of the bands are centred at $\pm\mathbf{p}_\theta$. The bands are shifted by using the *Fourier shift theorem* [68], which states:

$$\tilde{S}_s(\mathbf{k} \pm \mathbf{p}_\theta) = \mathscr{F}\left[\mathscr{F}^{-1}\left\{\tilde{S}(\mathbf{k} \pm \mathbf{p}_\theta\right\} \cdot e^{\pm i2\pi(\mathbf{p}_\theta \cdot \mathbf{r})}\right] \ . \tag{4.11}$$

Where $\mathscr{F}$ and $\mathscr{F}^{-1}$ represents the Fourier transform and the inverse Fourier transform respectively. Shifting the bands mathematically allows for sub-pixel positioning, which is crucial for avoiding reconstruction artefacts to the final image.

4.2.4 Reconstruction

Lastly, the different Fourier bands can be combined to produce an extended Fourier spectra. We achieve maximum shifting of the Fourier bands when the illumination spatial frequency equals the cut-off spatial frequency of the system $|\mathbf{p}_\theta| = \mathrm{k}_{\mathrm{cutoff}}$. Under this condition, the extent of the Fourier spectra is increased two-fold along one axis, leading to a two-fold improvement in resolution. To improve the extent in all directions, such that there is an isotropic resolution improvement, we must change the illumination orientation, θ, to acquire additional distinct Fourier bands along additional axes. Three angular orientations are often used, $\theta = 0°, 120°, 240°$, which enables the construction of complete Fourier spectra with up-to twice the extent than would be possible from widefield imaging alone. Through the use of three orientations, each with three phases means a standard SIM reconstruction requires nine raw input images. These nine raw images results in seven distinct Fourier bands, as the central Fourier band is recovered once per orientation. Additional orientations can be used, however with diminishing returns, as the gains in new spatial information is marginal [89].

Figure 4.4 shows the seven distinct recovered Fourier bands and how they combine to reconstruct a Fourier spectrum of increased extent. Theoretically, SIM can produce a two-fold improvement in image resolution as the extent of the image's Fourier spectra is doubled. This requires the illumination spatial frequency to be equal to the system's cut-off spatial frequency to produce a maximal shifting of the additional Fourier bands. In practice, this is challenging as the illumination

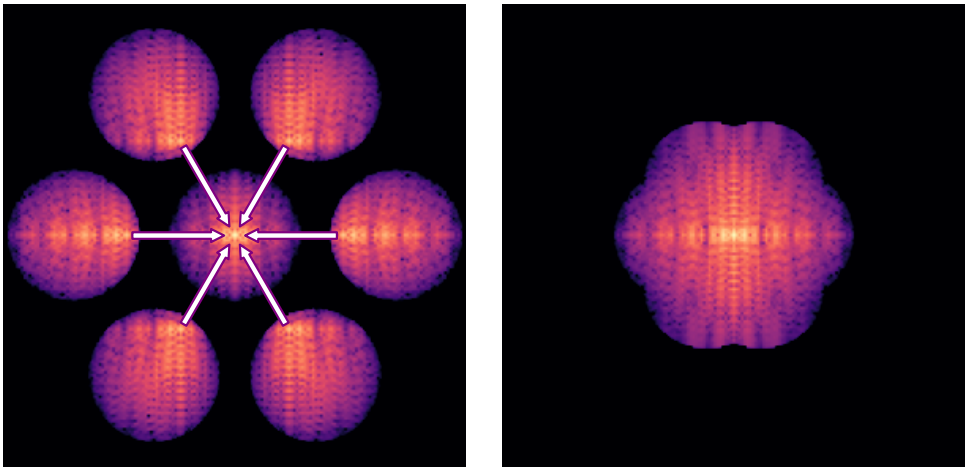

Figure 4.4: The seven recovered Fourier bands - each band contains a shifted zero-frequency peak that helps position each band correctly to produce a complete super-resolution Fourier spectrum.

pattern becomes poorly resolved due to strong attenuation of the higher spatial frequencies passing through the imaging system. This leads to low signal-to-noise and poor recovery of the encoded high spatial frequency information. Therefore, the optimal illumination frequency will be lower than the theoretical maximum, leading to a reduction in resolution improvement.

Under low-noise conditions, the distinct Fourier bands can be combined through simple addition,

$$\tilde{D}_{\mathrm{SIM}}(\mathbf{k}) = \sum_{\theta=\theta_1}^{\theta_3} \frac{1}{3}\tilde{S}_\theta(\mathbf{k}) + \tilde{S}_s(\mathbf{k}+\mathbf{p}_\theta) + \tilde{S}_s(\mathbf{k}-\mathbf{p}_\theta) \tag{4.12}$$

Finally, the inverse Fourier transform of the extent Fourier spectra can be taken, producing the super-resolution result.

$$D_{\mathrm{SIM}}(\mathbf{r}) = \mathscr{F}^{-1}\left[\tilde{D}_{\mathrm{SIM}}(\mathbf{k})\right] \tag{4.13}$$

4.2.5 Additional Comments

The outlined theory and reconstruction provides an initial and functional overview of the SIM process, highlighting the key concepts to understanding how super-resolution is attained. While, as a concept, SIM appears straightforward, in practice successful SIM reconstruction from experimental data is a highly nuanced and sensitive process. The most common problem faced with SIM, is the formation of reconstruction artefacts in the final super-resolution image. These include *ghosting*, where faint duplicates of an image structure are imposed on top of each other, and *ringing* where oscillatory patterns occur around sharp, high contrast edges. This is due to inaccuracies in determined parameters, such as the spatial frequency and phase of the illumination.

Throughout the history of SIM, there has been an on going effort for developing reconstruction techniques that are more robust under a variety of real-world conditions. This includes better algorithms that can determine the illumination spatial frequency and phase to accuracies as high as $\lambda/500$ [90], parameter-free deconvolution algorithms [88] and additional post-reconstruction filtering to suppress remaining image artefacts [91].

This has led to a highly subjective reconstruction process, dependent on the user's imaging requirements. For this chapter, a more fundamental implementation will be followed to demonstrate THz super-resolution imaging with minimal reliance on post-reconstruction processing. Allowing for a better evaluation of the SIM technique.

4.3 Simulation

A key aspect of structured illumination microscopy (SIM) that remains unexplored is the range of spatial scales over which the technique remains valid. While extensively demonstrated in the optical domain across various imaging modalities, SIM theory does not inherently define constraints on its applicability to the THz band.

With wavelengths spanning 10−100 μm, the THz wavelength range is three orders of magnitude larger than optical wavelengths. Therefore despite the larger FOV when compared to a typical optical microscope, when compared in units of the illumination wavelength, the THz imaging system operates on a much small relative FOV, as shown in Table 4.1. This raises the fundamental question: is there a spatial scale beyond which the SIM concept breaks down, potentially restricting its feasibility for our THz imager?

As seen in Table 4.1, the relative FOV of the THz imaging system is ~ 2.28 small in the linear dimension when compared to optical SIM, and therefore samples a relative area that is ~ 5.2 smaller. The numerical aperture of the THz imaging lens is also much smaller than those used in SIM. With a NA of 0.35 results in a much larger widefield resolution of 1.74 λ. In comparison, optical SIM takes advantage of commercial high-performance microscope objectives which can operate with a NA as high 1.2 leading to a widefield resolution limit of 0.51 λ.

This difference not only affects the THz system's ability to resolve finer details in widefield images, it also restricts the highest possible resolved spatial frequency of the structured illumination. While this alone should not impact the $\times 2$ gain

Table 4.1: Comparison of properties and scales for typical widefield SIM and our THz imaging system. Including the Field of View (FOV), Numerical Aperture (NA) and the Rayleigh Limit for resolution.

	λ	**FOV**	**FOV (λ)**	**NA**	**Rayleigh Limit**
Optical SIM [92]	488 nm	20×20 μm	$\sim 41 \times 41$	1.2	$0.51\,\lambda$
THz Imaging [37]	545 μm	10×10 mm	$\sim 18 \times 18$	0.35	$1.74\,\lambda$

in resolution through SIM, it may introduce sampling errors, due to the limited number of resolved fringes within the FOV, such that the SIM technique breaks down.

We can calculate the maximum number of fringes across the FOV by considering each system resolution limit. For optical SIM, with a fringe spacing of 0.51λ a maximum total of ~ 80 bright and dark sinusoidal stripes can fit within the FOV. For the THz imager, this is limited to approximately ~ 10.

This significantly reduces the spatial frequency content available for super-resolution reconstruction. While this is to be expected, as we are inherently sampling lower spatial frequencies in the THz regime, the reduced density of illumination fringes could impact the reconstruction process, particularly in terms of Fourier sampling. The extreme limit to this would be a sample illuminated by a single sinusoidal fringe, in which case, the three phase shifts would only modulate the overall image intensity rather than provide meaningful spatial frequency information, rendering SIM ineffective.

Therefore, through simulation, we need to validate whether our THz imaging system can support a sufficient fringe density to ensure adequate Fourier sampling and enable accurate super-resolution reconstruction.

4.3.1 Implementation Details

A simulation, based on the physical properties of the THz imaging system (shown in Table 4.1) was produced to demonstrate the effectiveness of the SIM technique at 0.55 THz. For this simulation, noise is ignored, as the primary focus is to validate the SIM method at THz frequencies. To model the properties of the THz imaging system, we use an ideal Optical Transfer Function (OTF) model that accounts for spatial cut-off frequency of the system.

The ideal OTF [93, 94] is given as,

$$\mathrm{OTF}(\nu) = \frac{2}{\pi}\left(\arccos(|\nu| - |\nu|\sqrt{1-\nu^2}\right) \tag{4.14}$$

where ν is the normalized spatial frequency $\nu = \mathrm{k} \,/\, \mathrm{k}_{\mathrm{cutoff}}$, with $\mathrm{k}_{\mathrm{cutoff}}$ being the maximum spatial frequency the OTF supports.

The sample object is the simulations input image, and is defined on a 500×500 pixel grid and represents the 10×10mm field of view. This therefore corresponds to a pixel size of 20μm. This similar to the pixel scale of the optical camera used in the THz imaging system.

For this simulation, we opted to use a binary mask as the sample object, representing a simple transmission mask. However, the simulation is not restricted to binary inputs and can represent more complex sample objects through greyscale input images. The input image illuminated by a perfect structured illumination, as described in Equation 4.2. The spatial frequency of the illumination was chosen to be $p = 1$ mm^{-1} which corresponds to a fringe spacing of $d = 1$ mm for a total of ten fringes across the FOV.

For given illumination orientation, three illumination phases of $\phi = 0°, 120°, 240°$ were used to generate three raw SIM images. The Fourier bands for the given orientation are then recovered using the inverse of the matrix that describes the system of equations laid out by Equation 4.6. Rather than computing the inverse matrix using the analytical form given by Equation 4.8, it is numerically computed for convenience.

As the simulation is noise-free, and the OTF is known exactly, the deconvolution step can be approximated through simple division of the Fourier band by the OTF. A small value $\epsilon = 10^{-6}$ is added to the OTF to avoid divide-by-zero errors.

The two shifted Fourier bands corresponding to $\tilde{S}(\mathbf{k} \pm \mathbf{p}_\theta)$ are then shifted to their true positions in Fourier space via the Fourier shift theorem (Equation 4.11).

Applying sub-pixel shifts to the Fourier bands, which are necessary for precise reconstruction, introduces interpolation artifacts. This occurs because the Fourier bands are represented on a discrete pixel grid and therefore applied Fourier transform discrete also. When a sub-pixel shift is applied, it corresponds to a fractional displacement that does not align with the sampling grid. Consequently, interpolation is required to estimate values between grid points. The existing discontinuity at the boundary edge of the Fourier band, is one such interpolation artefact, causing spectral information to "bleed" beyond the extent of the OTF, as shown in Figure 4.5.

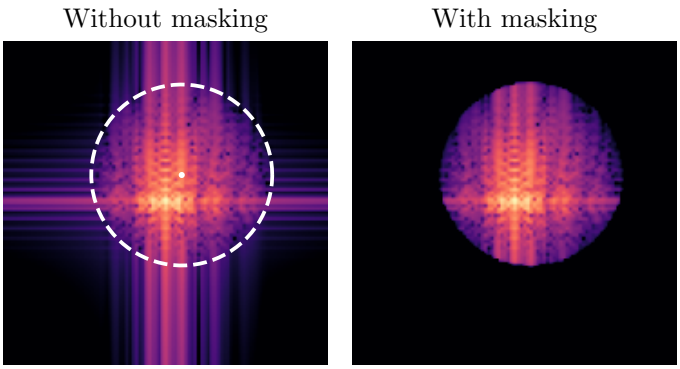

Figure 4.5: "Bleed-through" effect in the Fourier band due to sub-pixel shifting and how it can be cleaned through appropriate masking. The chosen masking is shown by the dashed white line. Note how the masking is centred around the position shifted OTF not the centre of the Fourier spectrum.

Reducing the discontinuity through apodization [81] can alleviate interpolation artifacts. However, since the bleed-through of spectral information occurs outside the OTF, it can be effectively removed by applying a circular mask with a radius equal to the OTF's extent.

The process is then repeated for a total of three orientations $\theta = 0°, 60°, 120°$, producing seven distinct Fourier bands (one central band and six additional bands). These bands can be combined to produce the near-isotropic super-resolution Fourier spectrum. A weighted mean is used to merge the bands, properly accounting for the overlapping regions of the Fourier bands.

Finally, the super-resolution image is acquired by taking the inverse Fourier trans-

form of the extended Fourier spectrum. The increased extent of the spectrum corresponding to higher spatial frequency detail and therefore improved resolution.

4.3.2 Results

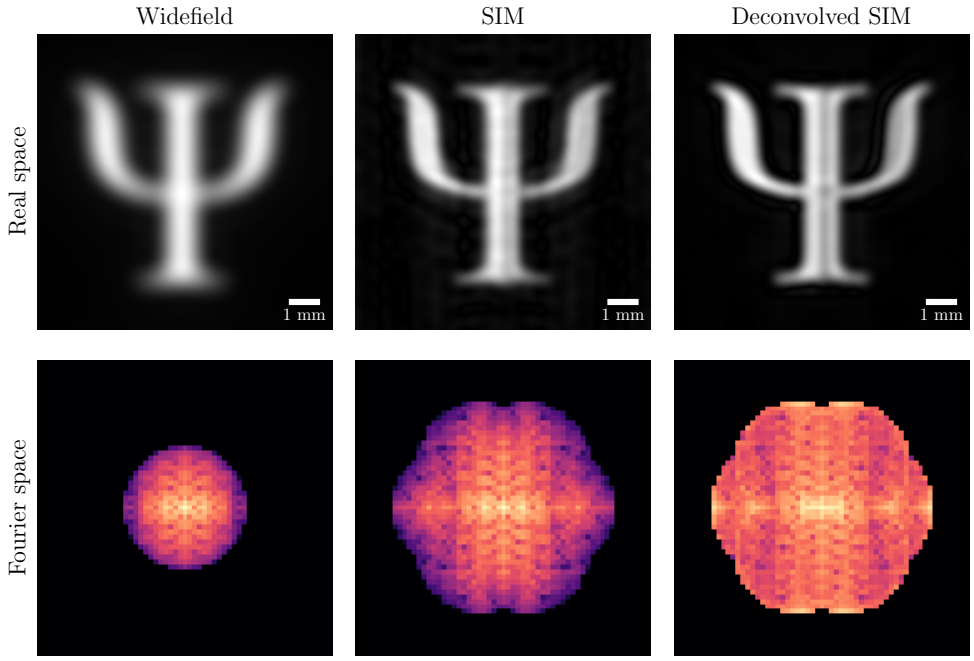

Figure 4.6: Simulation results for a test target of the Greek letter Ψ at 0.55 THz. Widefield, super-resolved, and deconvolved super-resolved images are presented, each accompanied by their corresponding Fourier spectra. The super-resolved images exhibit an extended Fourier spectrum, indicating enhanced spatial frequency content and, consequently, improved spatial resolution when compared to the widefield image.

The results of the simulation are presented in Figure 4.6, where a binary mask of the Greek letter Ψ is used as the sample object.

A total of nine raw SIM images—captured at three orientation angles, each with three phase shifts—are simulated and subsequently used to reconstruct a super-resolution image.

Three simulated images are shown: a widefield image, a reconstructed SIM image, and a deconvolved SIM image. Each is accompanied by its respective Fourier spectrum to illustrate the spatial frequency content.

The widefield image represents the expected appearance of the mask under uniform illumination, formed by the product of the mask and the system's OTF. At 0.55 THz, sharp edges are poorly resolved as the high spatial frequency information of the object is cut off by the low-pass filtering of the OTF. This is reflected by the Fourier spectrum's limited circular extent, which cuts off the higher spatial frequency information.

The SIM image exhibits sharper edges around the Ψ mask, demonstrating the resolution enhancement achieved through structured illumination. Some artifacts, such as added texture within the Ψ, arise due to errors introduced by Fourier interpolation during band shifting. However, the overall reconstruction remains accurate. The completed SIM reconstruction integrates seven Fourier bands, resulting in a spectral extent almost $\times 2$ larger than that of the widefield image. The two-fold increase in spatial extend allows for a theoretical two-fold improvment in resolution.

Despite the increased spectral extent, the finest details in the image suffer contrast loss due to attenuation of the Fourier bands. This is corrected in the deconvolved SIM image, which features the sharpest edges but introduces additional artifacts, such as a dark shadow line along the mask's center. While the spectral extent remains unchanged from the standard SIM image, deconvolution compensates for the OTF's attenuation of high spatial frequencies, enhancing contrast in fine details. The result is sharper, better resolved mask edges.

The simulation results demonstrate that SIM is effective at THz wavelengths. Despite initial skepticism, the technique achieves nearly a twofold increase in spectral extent compared to widefield imaging, successfully recovering high spatial frequencies and enhancing image resolution. While minor artifacts are introduced through Fourier interpolation and deconvolution, these do not compromise the overall accuracy and contrast of the reconstructed images. Thus, SIM presents a viable approach to overcoming the resolution limitations inherent in conventional THz imaging systems.

4.4 Generating Structured THz Illumination

Arguably, the most important requirement for Structured Illumination Microscopy is the precise generation of structured illumination itself.

The development of SIM has seen a multitude of techniques developed for generating high quality sinusoidal illumination [95–98]. Gustafsson's original implementation [46], now known as two-beam SIM, relied on two-beam interference to produce a sinusoidal fringe pattern. This is achieved using a diffraction grating to split an incident laser beam into multiple diffraction orders. Only the ± 1 orders are retained, while all others are blocked. The resulting beams are then focused onto the sample, where they interfere to form the structured pattern. Control over the illumination's phase and orientation was achieved by translating and rotating the diffraction grating. Through this approach, Gustafsson could produce fine, high quality fringes with a contrast $> 70\%$.

A key challenge in generating structured THz illumination is the precise alignment of optical components, essential for achieving well-controlled, high-quality structured patterns. Unlike optical and infrared imaging, THz imaging lacks direct visual alignment methods, as conventional aids like beam cards and viewing screens are ineffective. Without such tools, alignment must be inferred entirely from observations at the detector plane.

As a result, Gustafsson's approach becomes impractical at the THz band, as it requires precise polarisation control, diffraction grating alignment, diffraction order masking, and two-beam focusing on the sample plane to ensure high-quality structured illumination. A crucial design objective for THz structured illumination generation, therefore, is to ensure that precise alignment can be easily attained and reliably inferred from measured images.

4.4.1 Imaged Grating

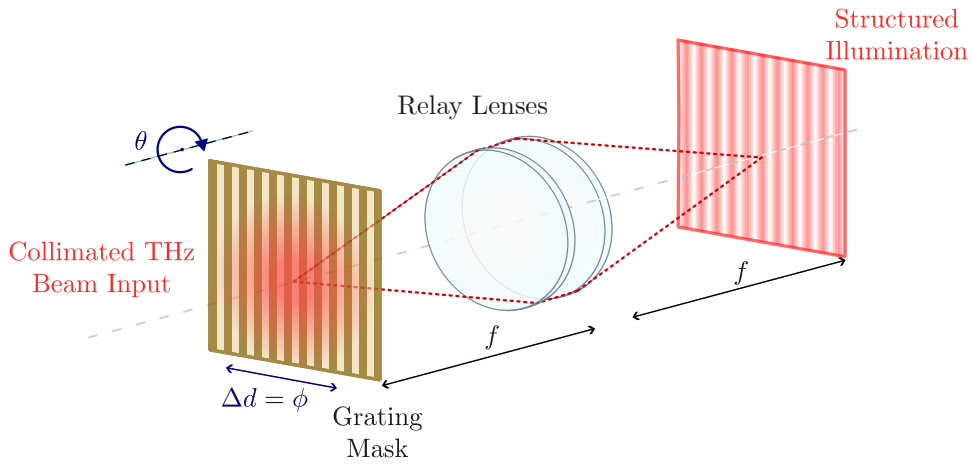

Figure 4.7: Structured illumination generated from a re-imaged grating. The phase of the illumination can be adjusted by laterally shifting the grating mask, where the orientation of the illumination can be adjusted by rotating the grating mask.

One simple method to generate a sinusoidal illumination pattern is to mask the illumination using a grating and employ a lens relay to map the structured pattern onto the object plane. At the grating plane, the illumination is structured as a perfect square wave. For a transmissive mask, if perfect absorbing or reflecting material is used, the illumination exhibits perfect contrast. Through the relay lens, the grating pattern is not only mapped onto the object plane but also low-pass filtered, converting the illumination into a sinusoidal pattern. This method approach several advantages.

The first is the effective alignment procedure. We project the structured illumination onto the object plane, which in turn is also the imaging plane of the THz system. Therefore if we image high-quality fringes on our THz system, we can infer correct alignment of the relay lens and grating. Further, if the relay lens is composed of two plano-convex lenses (as shown in Figure 4.7), we gain independent alignment control of each plane on either side of the relay. This enables the optimization of the positions of the relay lens elements and the grating mask.

Second, both the orientation and phase of the structured illumination can be easily controlled. The orientation can be adjusted by rotating the mask, while the phase is controlled through the lateral linear translation of the mask. For sub-millimetre grating spacing, achieving high phase precision ($> \lambda/100$) is easily attainable with the precision from inexpensive motorized translation stages.

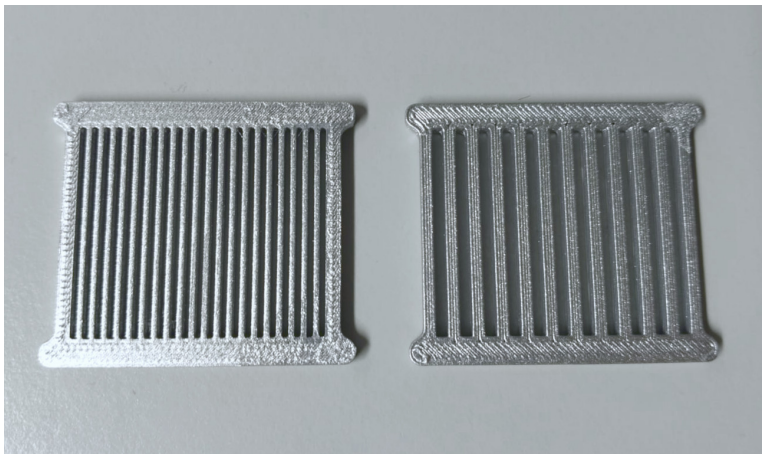

Figure 4.8: 3D printed, silver metallized structured grating masks, with periods of $d = 1.0$ mm (left) and $d = 2.0$ mm (right). This corresponds to a spatial frequency of k = 1.0 mm^{-1} and k = 0.5 mm^{-1} respectively.

Manufacture of the transmissive grating is straightforward. Through FDM (Fused Deposition Modeling) 3D printing. The lateral resolution of modern FDM 3D printers, which is on the micron scale, makes them ideal for producing sub-mm structures. Two 3 mm thick transmission masks (shown in Figure 4.8), with grating periods $d = 1.0$ mm and $d = 2.0$ mm were produced in PLA plastic, a commonly used material in 3D printing. While PLA is convenient for 3D printing, the transmission of 0.55 THz [99] through 3 mm of PLA is still high and would therefore lead to poor fringe contrast. To address this limitation, the printed gratings were spray coated with a layer of silver metallized paint, to enhance their ability to block and reflect the incident THz radiation.

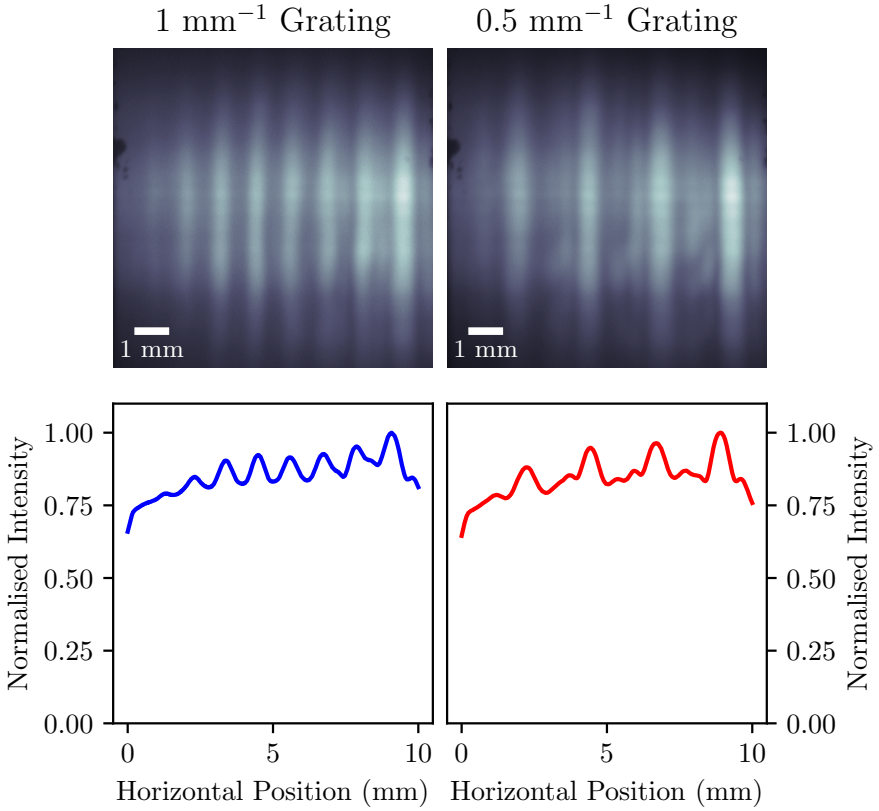

Figure 4.9: Observed structured illumination from the two 3D printed PLA masks of spatial frequencies k = 1.0 mm^{-1} which has an average fringe visibility of 13% and k = 0.5 mm^{-1} with an average fringe visibility of 16%. While the fringe visibility is slightly greater for the finer 0.5 mm^{-1} grating, only some of the fringes are resolved as the spatial frequency is greater than the imaging system's cut off spatial frequency.

To evaluate the optimal performance of the gratings, the gratings were illuminated by a collimated THz beam and place directly at the object plane of the imaging system, forgoing the need for the relay lens which would reduce fringe contrast. Figure 4.9 shows both the imaged fringes and cross-section profiles for both gratings.

Both masks show a periodic illumination profile, however the coarser 0.5 mm^{-1} is far from an ideal sinusoidal profile, with additional feature in the troughs of the illumination. This is a result of the spatial frequency of the grating being much lower than the spatial cut-off of the imaging system, therefore the square-wave nature of the grating is better resolved. This leads to additional higher-frequency

sinusoidal contributions to the profile. In comparison, the finer 1.0 mm^{-1} grating has a more fundamental sinusoidal profile, as the spatial frequency is closer to the cut-off frequency of the system. With an average contrast of the fringes is 10%, the illumination contrast is relatively high as the spatial frequency of the grating is close to the cut-off spatial frequency of the imaging system, and therefore is close to being unresolved. Therefore the grating is performing close to the theoretical maximum.

However, despite this, there are notable caveats to consider. For one, the fixed spatial frequency of the generated sinusoidal illumination requires prior knowledge of the system's cut-off frequency. This constraint limits the flexibility of the approach, as the spatial frequency cannot be easily adjusted for different imaging conditions. Additionally, while the alignment is made easier due to observable fringes at the detector plane, the system remains sensitive to misalignment. Precise positioning of the all elements, the grating, mask, and relay lens, is critical to ensure formulation of high quality fringes. Minor misalignments can distort and defocus the illumination and negatively impact the overall performance of the technique.

4.4.2 Fresnel Biprism

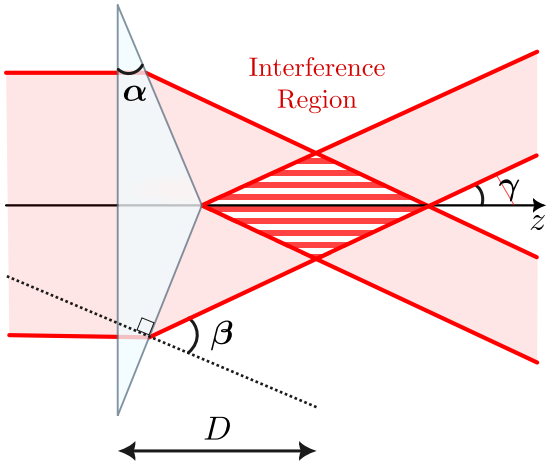

Figure 4.10: Diagram demonstrating how a Fresnel biprism generates two coherent beams, that overlap to produce a region of interference. A larger biprism angle α leads to a smaller overlap angle γ and therefore leads to finer fringes.

A more ideal approach would be to retain the two-beam interference setup to generate fringes with high contrast between the bright and dark regions (typically >80% in SIM [100]), but reduce the number of elements to reduce alignment complexity. This can be achieved through a Fresnel biprism [97], as shown in Figure 4.10. Through refraction of an incident collimated beam a Fresnel biprism generates two coherent beams that converge to produce a region of sinusoidal interference fringes.

This method offers one key advantage over the imaged grating: the structured illumination is produced by a single element, making it significantly easier to align the interference pattern onto the object plan and subsequently the imaging plane. As the biprism is illuminated by a collimated beam, the distance from the THz source and the biprism is not critical, which vastly simplifies the alignment.

4.4.2.1 Biprism Design

The fringe spacing, d, produced by the two interfering beams is dependent on the wavelength of the illumination, λ, and the intersection half-angle γ:

$$d = \frac{\lambda}{2\sin\gamma} \ . \tag{4.15}$$

γ can be determined from the biprism's refractive index, n and apex angle α [101].

$$\begin{aligned} \gamma &= \beta - \alpha \\ &= \arcsin(n\sin\alpha) - \alpha \end{aligned} \tag{4.16}$$

Where β is the angle between the refracted beam and the normal to the inclined surface of the biprism, as shown in Figure 4.10. Care must be taken to ensure that the angle α remains less than the critical angle, $\alpha < \arcsin\left(\frac{1}{n}\right)$, to prevent total internal reflection and ensure refraction of the incident beam through the biprism.

Figure 4.11 shows the expected fringe separation for varying pitch angles for common THz optic materials. With the use of high refractive index materials, or high prism angles, it is possible to generate the millimetre scale fringes required to approach the cut-off spatial frequency limit of our imaging system.

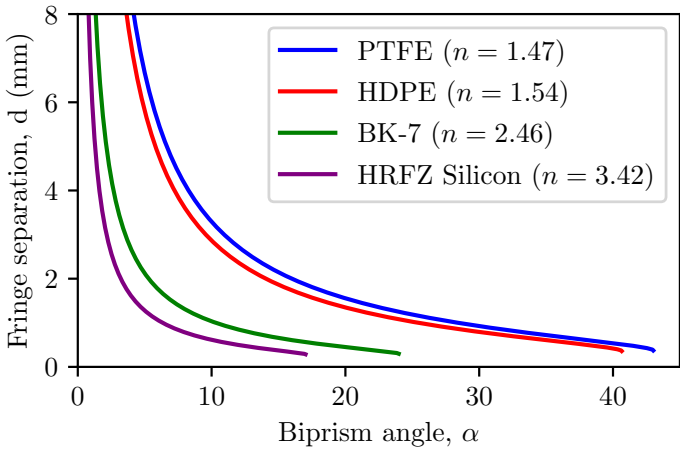

Figure 4.11: Fringe separation as a function of biprism pitch angle. Four common THz optics materials are considered for an illumination frequency of 0.55 THz.

4.4.2.2 Biprism Manufacture

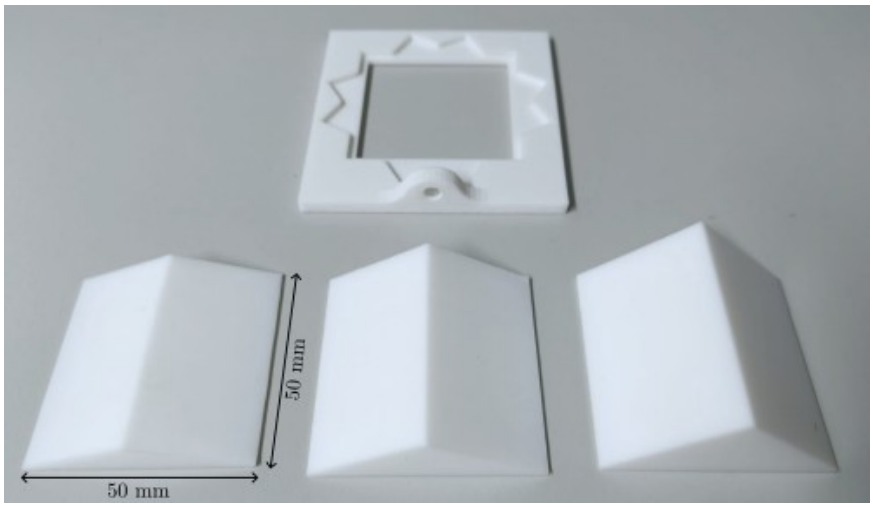

Figure 4.12: Three 50×50 mm PTFE Fresnel biprisms with varying pitch angles (left-to-right) $\alpha = 20°, 30°, 40°$. The fixed angle biprism mount is shown at the top.

PTFE, with a refractive index of $n = 1.47$ [38], was chosen as the material to fabricate several Fresnel biprism. This is due to its excellent transmittance at 0.55 THz [38], availability and machinability. Using conventional machining, three Fresnel biprisms was fabricated with a square base measuring 50×50 mm to match the diameter of the optics used in the THz imager. Each biprism was produced was a different biprism angle of $\alpha = 20°$, $30°$, $40°$ in order to evaluate varying fringe separations. The angles of the biprisms were chosen for ease of manufacturing, rather than targetting any specific fringe spacing. However, using Equation 4.15, we can calculate the expected fringe spacing to be $d = 1560,\ 927,\ 540$ μm respectively.

To hold and orientate the biprisms, a simple push-fit mount was 3D printed. The mount allowed the biprism to be orientated at the three required illumination angles $\theta = 0°$, $60°$, $120°$. The biprisms and mount are shown in Figure 4.12.

4.4.2.3 Characterising Biprism Performance

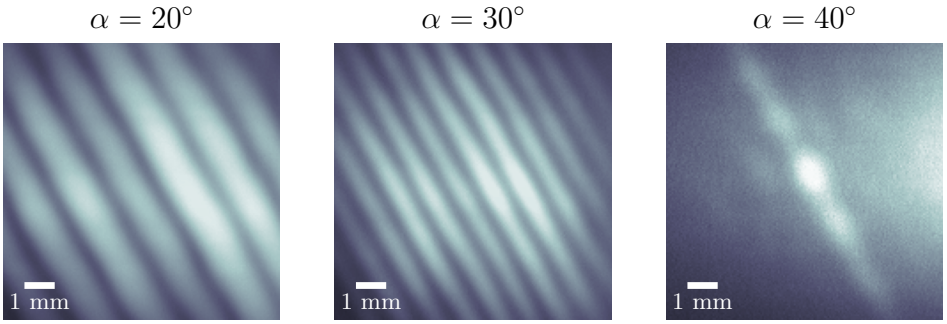

Figure 4.13: Comparison of interference fringes generated by Fresnel biprisms of varying pitch angles, leading to variable fringe size and spacing.

To characterize the performance of the produced biprisms, each biprism was placed within the THz imaging system as shown in Figure 4.10 and illuminated by a collimated THz input. The position along the optical axis was optimized such that the largest interference region produced by the biprism occurred at the imaging plane of the THz imaging lens. Each biprism was orientated at $\theta = 60°$ to check the produced fringes extend across the full 10×10mm FOV. These images are shown in Figure 4.13.

Both the $\alpha = 20°$ and $\alpha = 30°$ biprism show uniform fringes with visible contrast, that extend across the entire FOV which demonstrates the extent of the fringes is sufficient for full-field imaging. With the $\alpha = 30°$ biprism producing finer fringes, with a total of 12 complete fringes across the field of view compared to the shallower angled $\alpha = 20°$ biprism which produces 7 complete fringes across the field of view.

For $\alpha = 40°$ biprism, no visible fringe pattern could be observed. With the steepest biprism angle, the 40° biprism should produce the finest fringes with a separation of $d = 0.540$ mm and therefore spatial frequency of $p = 1.85$ mm^{-1}. Which falls beyond the cut-off frequency of the imaging lens, therefore the produced fringes cannot be resolved.

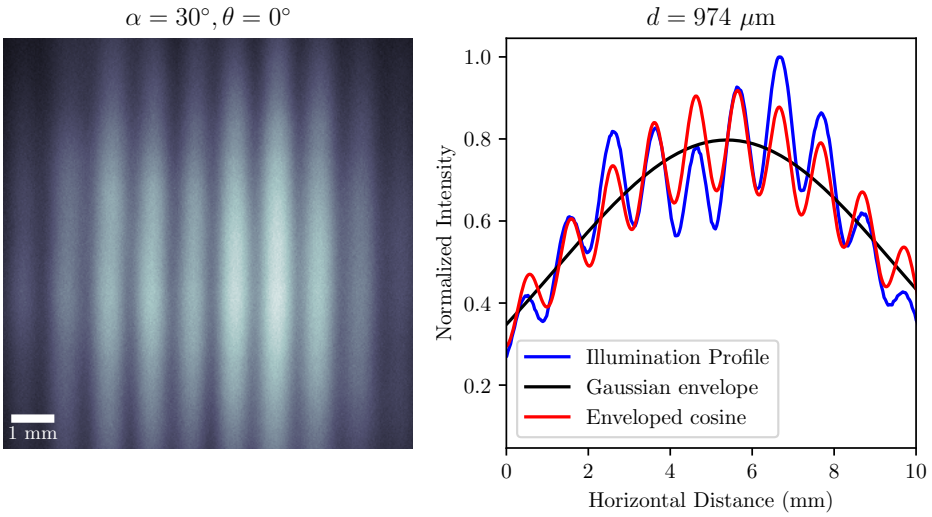

Figure 4.14: Fringe profile of horizontal fringes produced by the $\alpha = 30°$ biprism. (Left) Widefield THz image of the fringes generated by the biprism. (Right) The resulting horizontal cross-section profile, showing the sinusoidal structure imposed on a Gaussian envelope.

Further analysis of the vertical fringes produced by the $\alpha = 30°$ biprism is shown in Figure 4.14. A mean horizontal cross-section shows the profile of the structured illumination. The sinusoidal fringes of the illumination is ultimately enveloped by a Gaussian profile. This Gaussian envelope arises from the collimated Gaussian illumination of the THz source, suggesting that a larger diameter collimated beam would produce more uniform fringes. Accounting for the Gaussian profile, a fitted cosine function yields a fringe spacing of $d = 974 \pm 3\ \mu$m and an average fringe contrast of 21%. This fringe contrast is greater than the contrast of the imaged grating. The fringes are more uniform and don't feature any higher harmonic features.

The observed fringe spacing is larger than the estimate of 927 μm. This difference may be attributed to a convergence of the input THz beam, which reduces the convergence angle γ, leading to the formation of coarser fringes. This is not a significant issue for use in SIM, as long as the spatial frequency of the illumination is properly calibrated and known at the time of imaging.

4.4.3 Choice of Structured Illumination

In summary, both the re-imaged grating approach and the Fresnel biprism method generate structured illumination with a fringe contrast of approximately 20%. However, the Fresnel biprism offers a clear advantage in alignment. Unlike the grating, which requires multiple optical elements to form the structured illumination, the Fresnel biprism only requires a collimated beam and provides a region of maximum interference that can be easily positioned onto the imaging plane by alignment of the biprism. This simplifies the alignment process, as only a single optical element needs to be positioned. Given the comparable fringe contrast, the Fresnel biprism is the preferable choice for its ease of alignment and consistent fringe quality.

4.5 Experimental Implementation

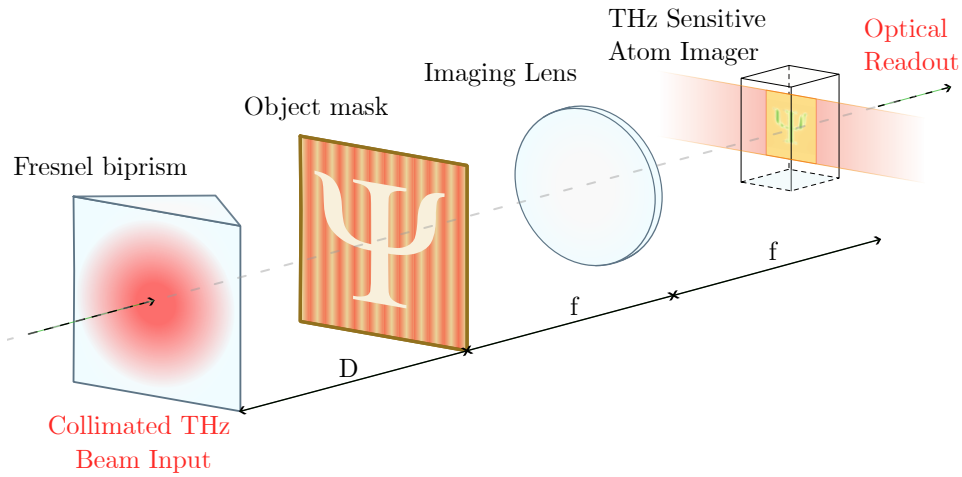

Figure 4.15: Experimental layout for THz SIM using a Fresnel birprism. The birprism, illuminated by an incoming collimated THz beam, generates the sinusoidal fringes at the object plane. The structured illuminated object is then imaged by the silicon imaging lens, which focuses the THz image onto the THz sensitive thermal vapour.

The experimental layout is shown in Figure 4.15, laying out the THz optics used. For clarity the THz source, laser systems and optical readout parts of the experiment are omitted, however they remain as described in Chapter 2.

A collimated Gaussian THz beam, with a beam diameter of $\sim$ 22mm, is used to illuminate the 50×50 mm base side of the Fresnel biprism. Informed by the biprism characterization, the $\alpha = 30°$ was used. Prior to imaging, the biprisms alignment was optimized to produce the highest contrast fringes. To aid positioning along the optical axis, the biprism and the biprism mount were affixed to a manual translation stage.

Unlike optical SIM, where the illumination optics undergo some translation in order to produce the required illumination phase shifts, we opt to instead translate the object through the illumination. This is to ensure the illumination remains stable and well aligned. This reduces the FOV by $\frac{2}{3}$ the fringe spacing, which leaves sufficient FOV to image the whole target mask.

The target mask was mounted to two Thorlabs electronic translation stages (also omitted from Figure 4.15) providing control over the masks positioning. For each illumination orientation θ, three equidistant illumination phases ($\phi = 0, 2\pi/3, 4\pi/3$) were used, resulting in an object translation of $\frac{d}{3}$ along the direction of the illumination orientation for each phase.

The power of the THz source was set to ensure maximum intensity without saturating the fluorescence from the atomic vapour, and the exposure of the optical readout camera was set to 500 ms to maximise signal-to-noise without saturation of the sensor.

To first demonstrate super-resolution from structured illumination, a single orientation $\theta = 0°$ was used. Therefore the mask was only translated along the horizontal direction. This resulted in 3 raw SIM images ready for reconstruction. To evaluate the effectiveness of the super-resolution technique, we omit the described deconvolution step.

4.5.1 Target Mask

A simple binary mask was used as the target, fabricated by machining the desired shape into a brass sheet. The brass reflects incident THz illumination, resulting in a high-contrast transmission image of the machined shape.

For this experiment, we opted to image a mask of the Durham University shield, which features a central cross as shown in Figure 4.16. While the cross can be resolved by widefield THz imaging, the low contrast of the cross is a result of it being close to the widefield resolution limit of the system. The Durham shield measures 8×9.1 mm and therefore fills the imaging system's FOV.

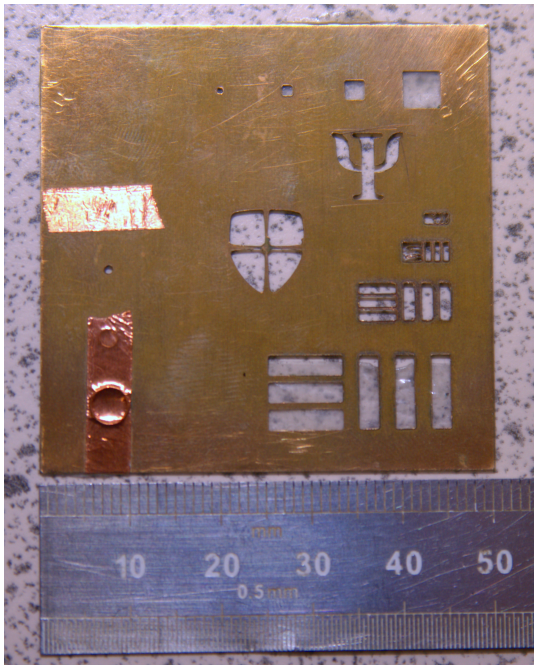

Figure 4.16: Photo of the brass binary transmission mask with the chosen Durham University shield target at the masks centre.

4.5.2 Calibration

Prior to imaging, the system must be calibrated to ensure that the object is translated by the correct distance to achieve the intended phase shift. First, the effective pixel size and therefore spatial scaling of the imaging system must be determined. This is achieved by translating a pinhole across the field of view by a known distance, allowing calibration of the effective pixel size and a check for linearity while translating across the FOV. For this experiment, a pinhole mask is mounted on the translation stages and moved in 1 mm intervals. This process is done for both horizontal and vertical axes. This is performed without biprism illumination, using only the collimated THz beam. Second, the fringe separation (or spatial frequency) of the illumination must be determined. This follows the same procedure used to characterize the biprism fringe profile, as shown in Figure 4.14, and is performed before introducing the target mask. Since this step relies on accurate spatial scaling, it depends on the first calibration.

4.5.3 Additional Image Processing

As we are translating the object, rather than phase shifting our illumination, the captured images must be 'shifted' digitally such that the object's positions remains fixed across the three images. In doing so, this leads to an illumination that effectively varies in phase.

This can be achieved using the applying the same Fourier shift theorem that is used during the SIM reconstruction process (as defined in Equation 4.11). The required lateral shift along the illumination axis, Δx, for a given image is given by:

$$\Delta x = d\frac{\phi}{2\pi} \ , \tag{4.17}$$

where d is the fringe spacing and ϕ is the phase shift in radians.

4.6 Results

The resulting SIM reconstruction and comparative widefield are show in Figure 4.17 with their respective Fourier spectra.

The comparative widefield show the expected image of the Durham University shield, as the cross of the shield is on the scale of $\sim$ 1 mm, it is just resolved by the THz imager. The Fourier spectra of the widefield image is masked by the theoretical OTF of the imaging system. This offers noise rejection while not affecting the spatial resolution of the widefield image.

The SIM image has two significant features. Firstly, both the vertical edges of the shield and internal cross are visibly sharper, demonstrating at improved contrast and therefore resolution from the reconstruction. In comparison the horizontal section of the cross remains poorly resolved when compared to the widefield, as the Fourier extent in the vertical direction is the same for both images.

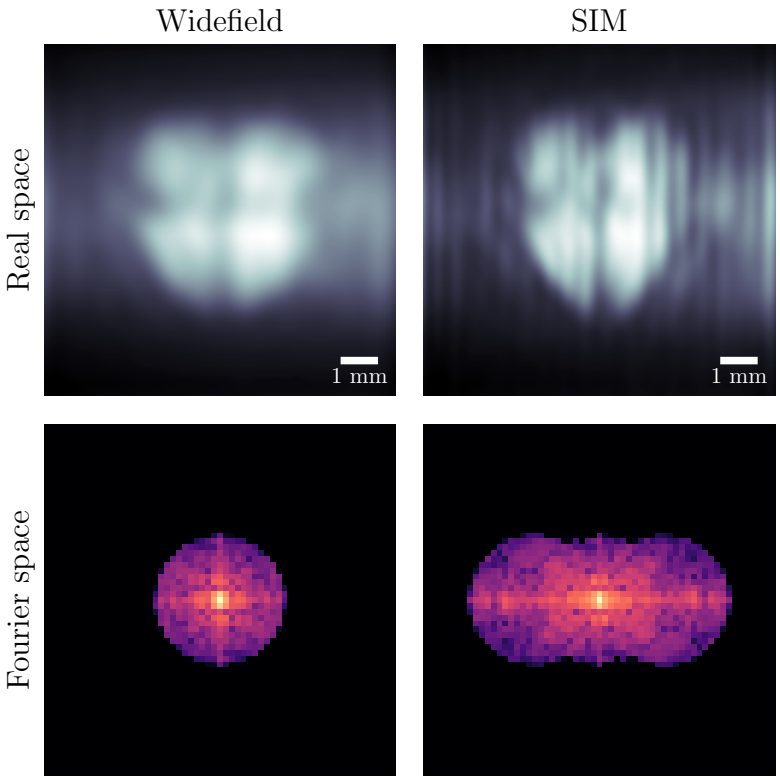

Figure 4.17: Images of the shield mask from widefield imaging and through super-resolution reconstruction. For both images, their respective Fourier spectra are shown, by comparing the Fourier spectra we can see the super-resolution image has an extended domain which provides access to higher spatial frequency information. While the super-resolution image shows promising improvement on edge contrast, significant fringing artefacts from a poor reconstruction exists. The possible causes of this are discussed further later.

The second significant feature of the SIM image is the significant image artefacts, which limits the success of the reconstruction. These artefacts take the form of high frequency fringes, and suggests some issue with the input raw SIM images. These issues are explored the the following sections, where the raw SIM images are validated in order to deduce the source of the strong fringe artefacting.

As a result, while qualitiative comments can be made with regards to the improvement in contrast and resolution in the super-resolution image. The strong artefacting makes it impractical to draw quantitative resolution measurements. This hinders the ability to conclusively declare this SIM approach as an effective super-resolution result, however this is a known risk in the reconstruction process

of SIM images.

4.6.1 Incorrect Phase

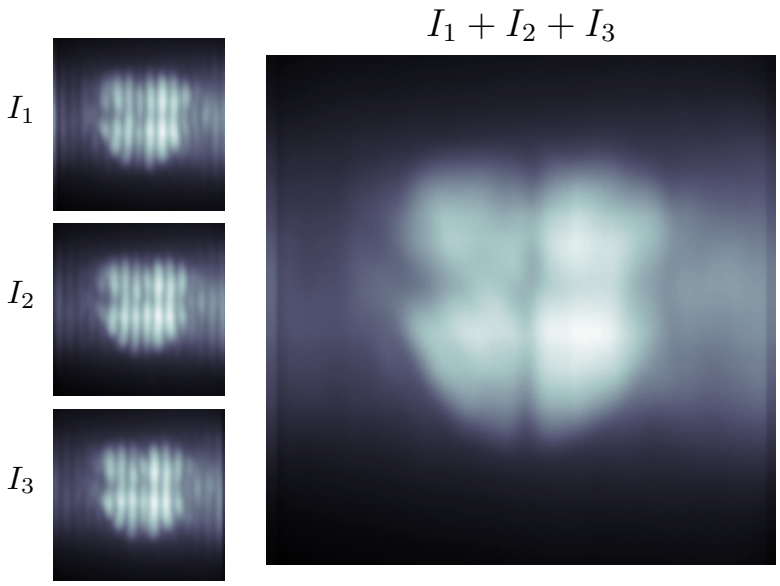

Figure 4.18: Validation of the phases being equidistant, as the summation of the three phases $I_1+I_2+I_3$ leads to a reconstructed widefield image. As the summation image contains no residual sinusoidal structure, we can be confident that the three phase angles are equidistant.

One possible issue with the reconstruction is calculated phases of the illumination, ϕ are incorrect. This is a particular possibility for our approach of shifting the object, as either the physical translation of the object or digital translation back could induce such errors.

As our phases are chosen to be equidistant, we can validate the phases are correct through a simple summation of the three SIM images. The sum of the three sinusoidal illuminations results in a uniform illumination [102]. Therefore, the sum of the three SIM images should generate an effective widefield image. Any deviation from equidistant phases, however, should introduce residual sinusoidal structure into the summed image. As a result, the summation of the three phase $I_1+I_2+I_3$ shown in Figure 4.18 validates the assumption that the three phases are equidistant as the summed image does not contain any residual sinusoidal structure.

While the phases are equidistant, there may be a phase offset present. We can show this does not affect the final image reconstruction by considering Equation 4.6. If all three phases are shifted by $\Delta\phi$, the phase offset factorizes out as a global phase.

$$\begin{bmatrix} e^{i\Delta\phi} & \frac{1}{2}e^{i(\phi_1+\Delta\phi)} & \frac{1}{2}e^{-i(\phi_1+\Delta\phi)} \\ e^{i\Delta\phi} & \frac{1}{2}e^{i(\phi_2+\Delta\phi)} & \frac{1}{2}e^{-i(\phi_2+\Delta\phi)} \\ e^{i\Delta\phi} & \frac{1}{2}e^{(\phi_3+\Delta\phi)} & \frac{1}{2}e^{-i(\phi_3+\Delta\phi)} \end{bmatrix} = e^{i\Delta\phi}\,\mathbf{M} \tag{4.18}$$

Therefore we can be confident that the phases of the three SIM images are correct.

4.6.2 Incorrect Spatial Frequency

Another possibility, is the measured spatial frequency of the illumination is incorrect. However the same argument with the correct phases holds, as the correct phases require the lateral translation of the object to be correct. This in turn requires the spatial frequency of the illumination must be known and correct. See Equation 4.17.

4.6.3 Additional spatial frequencies

The primary source of image artifacts in SIM reconstructions is high-frequency fringes. These fringes exhibit spatial frequencies comparable to or exceeding the fundamental illumination frequency. The source of the unwanted fringes remains unknown.

One possible cause could be from an illumination with additional unwanted spatial frequencies. If the illumination was not just of one spatial frequency $\mathbf{k}$, but a summation of spatial frequencies $\mathbf{k} \pm \delta\mathbf{k}$ then the additional spatial frequencies would constitute as unwanted noise that would propagate through the reconstruction process and lead to unwanted high-frequency fringes in the final image.

Ultimately, the image artefacts highlight the importance of high quality illumination and the sensitivity of the SIM reconstruction algorithm.

4.7 Conclusion

This chapter outlined the concept and theory of Structured Illumination Microscopy that leads to a theoretical two-fold increase in spatial resolution. It considered how the differing spatial scales between optical microscopy and widefield THz imaging may impact the effectiveness of the technique when applied to the THz band. Through simulation, it was shown that there is no discernable limit to SIM that would prevent implementation at THz frequencies.

Methods to generate THz structured illumination were explored, with the Fresnel biprism approach chosen for its low complexity and ease of alignment. Applying structured illumination to a binary mask target produced a SIM reconstruction that demonstrated super-resolution potential but was ultimately too corrupted by image artefacts. Possible causes of these artefacts were briefly discussed, highlighting the sensitive nature of the SIM reconstruction process.

Chapter 5

Virtually Structured Detection

This chapter introduces the Virtually Structured Detection (VSD) concept, a variation on SIM. It explores the differences with VSD and demonstrates how this approach removes the need for a perfect widefield structured illumination. Using SIM as the foundation, the theory associated with VSD is presented. I validate the use of the technique at the THz band through simulation, before evaluating the best experimental approach. Experimental results are then presented, showing quantitive super-resolution at 0.55 THz.

5.1 Concept

Virtually Structured Detection (VSD) was initially developed as an ophthalmoscopy technique to image the retina with high detail [103–105]. Unlike SIM, which requires widefield structured illumination, VSD is a spot or line scanned approach. This avoids the potential distortion of a structured illumination as it passes through the thick and/or complex media, such as the eye. Therefore enabling robust super-resolution imaging under challenging clinical conditions. As a result, VSD provides a method of super-resolution under conditions where generating reliable widefield structure illumination is challenging.

The VSD concept arises from the idea that structured illuminated images can

be computationally synthesized from a series of widefield images captured while the sample is scanned with a point or line illumination. These computationally generated structured images are then processed and reconstructed like regular SIM images to produce a super-resolution result.

At first glance, this approach may seem fundamentally flawed — how can higher-resolution details of the sample be extracted by simply applying post-detection processing? As with SIM, VSD exploits spatial frequency mixing between the illumination and sample structure. However, instead of a widefield structured illumination creating a global Moiré pattern, a single-point or line illumination interacts locally with the sample. Therefore the resultant image inherently contains high-frequency spatial information of the sample, though it remains inaccessible in its raw form. By computationally imposing structure onto the data through digital modulation, higher-resolution details that would otherwise remain unresolved can be decoded and reconstructed.

This process is analogous to lock-in detection, where a known reference signal is used to extract weak signals from noise. In VSD, the computationally imposed virtual structure acts as the reference, enabling selective extraction of high-frequency information embedded within the raw image data. Through this technique, super-resolution is achieved without the need for physically structured illumination.

5.2 Theory

As with widefield SIM, understanding VSD starts by considering the *imaging equation*, with the detected image $d(\mathbf{r})$ as,

$$d(\mathbf{r}) = [i(\mathbf{r}) \cdot s(\mathbf{r})] \otimes h_{de}(\mathbf{r}) \ , \tag{5.1}$$

with $\mathbf{r} \equiv (x, y)$ the spatial position vector and $\otimes$ being the 2D convolution operator. $s(\mathbf{r})$ is the target sample, $i(\mathbf{r})$ the illumination field and $h_{de}(\mathbf{r})$ the Point Spread Function (PSF) of the imaging optics on the detection portion the imaging system. For a diffraction-limited line-profile illumination, it is found that

$$\begin{aligned} i(\mathbf{r}) &= i(x, y) \\ &= \delta(x) \otimes h_{il}(x, y) \\ &= h_{il}(x, y) \\ &= h_{il}(\mathbf{r}) \end{aligned} \tag{5.2}$$

where $h_{il}(x, y)$ is the PSF of the illumination system. The delta function $\delta(x)$ localises the illumination along the x-axis, and when convolved with the PSF produces a diffraction-limited line illumination. Thus, the illumination profile is strictly determined by the illumination PSF.

Therefore by substituting Equation 5.2 into Equation 5.1,

$$d(\mathbf{r}) = [h_{il}(\mathbf{r}) \cdot s(\mathbf{r})] \otimes h_{de}(\mathbf{r}) \ , \tag{5.3}$$

Where $d(\mathbf{r})$ is one acquired widefield image of the line-scanning process. With this, the VSD processing can be applied to our image; this involves two important steps.

First, the image is multiplied by a digital modulation mask $m(\mathbf{r})$ before second, being spatially integrating across the scan axis. The result is a one pixel wide 'picture', $p_i(\mathbf{r})$:

$$\begin{aligned} p_i(\mathbf{r}) &= \iint m(\mathbf{r}) \cdot d(\mathbf{r})\ d\mathbf{r} \\ &= \iint m(r) \cdot [h_{il}(\mathbf{r}) \cdot s(\mathbf{r})] \otimes h_{de}(\mathbf{r})\ d\mathbf{r} \end{aligned} \tag{5.4}$$

The picture is indexed by i, as it represents a single captured image during the image scanning process. By integrating spatially, Equation 5.4 becomes a convolution integral (see Appendix B), and therefore can be rewritten as

$$p_i(\mathbf{r}) = [\{m(r) \otimes h_{il}(\mathbf{r})\} \cdot s(\mathbf{r})] \otimes h_{de}(\mathbf{r}) \tag{5.5}$$

Based on the inherent properties of convolution [105], the image can be equivalently expressed as

$$p_i(\mathbf{r_i}) = h_{il}(\mathbf{r}) \otimes \{[h_{de}(\mathbf{r}) \otimes m(\mathbf{r})]\, s(\mathbf{r})\}\ , \tag{5.6}$$

Which is the exact expression for acquired images from widefield SIM, therefore VSD can be used to digitally construct the required raw images by stacking successive scans to produce one single raw SIM image $p(\mathbf{r}) = [p_1(\mathbf{r_1}) \cdots p_n(\mathbf{r_n})]$.

Similar to widefield SIM, the modulation applied is sinusodial

$$m(\mathbf{r}) = \cos\left(2\pi \mathbf{p}_\theta \cdot \mathbf{r} + \phi\right)\ , \tag{5.7}$$

where $\mathbf{p}_\theta \equiv (p\cos\theta, p\sin\theta)$, p is the modulation frequency, θ is the scan angle, and ϕ is the modulation phase. The scan direction and modulation direction are aligned, with the modulation oriented along the scan angle. It should be noted, that unlike widefield SIM, the modulation does not need to include a constant

offset as the mask is applied digitally therefore negative modulation is permitted. Therefore the Fourier transform of the modulation is,

$$\tilde{M}(\mathbf{k}) = \delta\left(\mathbf{k} + \mathbf{p}_\theta\right) e^{i\phi} + \delta\left(\mathbf{k} - \mathbf{p}_\theta\right) e^{-i\phi} \ . \tag{5.8}$$

which comprises of the expected delta functions $\delta\left(\mathbf{k} \pm \mathbf{p}_\theta\right)$, which through convolution shifts the content of $\tilde{S}(\mathbf{k})$, the Fourier spectrum of the sample by $\pm\mathbf{p}_\theta$. This follows the same behaviour as with SIM, therefore when applied to Eq. (5.6) the resultant Fourier spectra is

$$\tilde{P}(\mathbf{k}) = \tilde{H}(\mathbf{k}) \left[\tilde{S}(\mathbf{k} + \mathbf{p}_\theta)e^{i\phi} + \tilde{S}(\mathbf{k} - \mathbf{p}_\theta)e^{-i\phi}\right] \ . \tag{5.9}$$

Where $\tilde{S}(\mathbf{k} \pm \mathbf{p}_\theta)$ are the shifted Fourier bands of the sample object, which contain higher spatial frequency information that would otherwise be cut-off by the optical transfer function (OTF) of the imaging system $\tilde{H}(\mathbf{k}) = \tilde{H}_{il}(\mathbf{k})\tilde{H}_{de}(\mathbf{k})$.

To separate the two shifted Fourier bands, Eq. (5.9) can be solved by changing the phase of the digital modulation.

$$\tilde{H}(\mathbf{k})\tilde{S}(\mathbf{k} \pm \mathbf{p}_\theta) = \tilde{P}(\mathbf{k}, \phi = 0) \pm i\tilde{P}(\mathbf{k}, \phi = \pi/2) \ . \tag{5.10}$$

It is also advantageous to have access to the non-shifted Fourier spectra of the sample object, $\tilde{S}(\mathbf{k})$, for better super-resolution reconstruction. The central band is recovered when the modulation frequency is zero,

$$\tilde{H}(\mathbf{k})\tilde{S}(\mathbf{k}) = \tilde{P}(\mathbf{k}, \mathbf{p}_\theta = 0) \ . \tag{5.11}$$

With all three Fourier spectra separated, standard SIM reconstruction can now follow; including deconvolution, band shifting and combining, as outlined in Chapter 4. As with SIM, to produce an isotropic resolution improvement requires at least three scan angles of $\theta = 0°, 60°, 120°$.

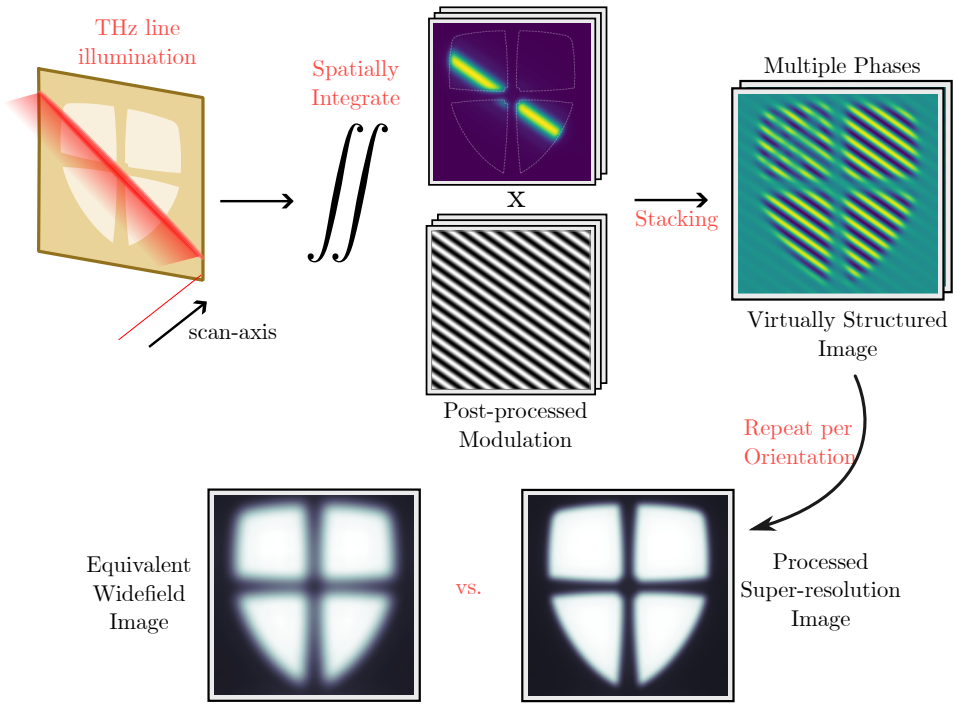

Figure 5.1: Schematic diagram outlining the VSD process. Briefly, the sample object is line scanned by the illumination with a full-frame image taken at each scan position. These full-frame images are then multiplied by a digital modulation before being spatially integrated and stacked. This in effect produces one of the virtually structured images. Through the use of three scan orientations $\theta = 0°, 60°, 120°$ and two phases per orientation $\phi = 0, \pi/2$ an isotropic super-resolved image can be constructed.

The outlined VSD process is shown diagrammatically in Figure 5.1. This demonstrates how multiple image scans are individually digitally modulated before spatially integrated to produce many pixel-wide pictures, $p_i(\mathbf{r})$ (Equation 5.6). These are then stacked to produce one virtually structured image $p(\mathbf{r}, \phi)$, with a given phase ϕ which is determined by the phase of the applied modulation.

This is repeated for both phases $\phi = 0, \pi/2$, which allows the two shifted Fourier bands for this orientation to be recovered. The central Fourier band is also recovered by applying the VSD process without modulation.

To produce an near-isotropic super-resolution image. The linescanning and processing must be repeated for all three orientations. This produces the seven distinct Fourier bands required to build up an super-resolution image.

5.3 Advantages of Virtually Structured Detection

There are three key distinct advantages in using VSD rather than widefield SIM:

The first is the need for precisely determining the spatial frequency and phase of the structured illumination is eliminated. As the modulation is applied digitally rather than physically, the spatial frequency and phase of the modulation is precisely known. This removes any associated reconstruction artefacts that arise from estimation errors in the illumination parameters.

Second, as the spatial frequency of the modulation mask is precisely known, it can be made to equal the cut-off frequency of the OTF, leading to maximal band shifting and therefore maximal resolution improvement. This is not possible in SIM, as the structured illumination needs to be resolved by the imaging system, and therefore must be of a spatial frequency lower than the cut-off frequency.

The last advantage is the reduction in implementation complexity. Over the 25 years of wide-field SIM development, a variety of illumination systems have been proposed [46, 95, 106, 107], each improving the robustness of the illumination at the expense of increasing complexity. As seen with SIM, producing the high quality structured illumination is a non-trival task. In comparison, VSD the generation of diffraction-limited line profile is trivial due to the simplicity of the illumination mask approach.

These advantages come at one obvious cost, an significant increase in the number of raw images required for reconstruction. VSD reconstruction requires many images per scan orientation, the number of which depends on the field of view and the widefield diffraction limit of the system. The number of scan images must be such that the resultant reconstruction is not hindered by the Nyquist sampling limit. For a modern microscope, this can easily be hundreds of images per orientation. SIM in comparison, only requires 3 raw images per orientation. As a result, VSD will always have a slower acquisition process when compared to SIM.

5.4 Generating THz Line Illumination

Generating the line illumination that has a width no larger than the diffraction limit of the imaging system is important for the VSD approach. This ensures the the resolution of the system is limited by the PSF of the imaging system rather than the PSF of the illumination.

There are two sensible approaches to generating the line-illumination required. Either by focusing a collimated THz source along one dimension using a cylindrical lens and focusing onto the object plane. Or by illuminating a sub-diffraction wide slit and projecting the masked illumination onto the object plane by using a relay lens.

Here both approaches were simulated using the *diffractio* Python package [108], which simulates the wave propagation of an input Gaussian THz field through numerical calculation of the Rayleigh-Sommerfeld diffraction integral [109].

For both simulations, a 17 mm diameter 0.55 THz ($\lambda = 545$ μm) collimated THz beam is used as the input source. Both the cylindrical lens and relay lenses have a focal length of $f = 75$ mm, diameter of $d = 50$ mm and are assumed to be made of PTFE ($n = 1.46$). This makes the numerical aperture of both the lenses equal, and therefore the simulation comparable. The intended outcome of the simulations is to determine which approach is most practical for our use.

5.4.1 Cylindrical lens

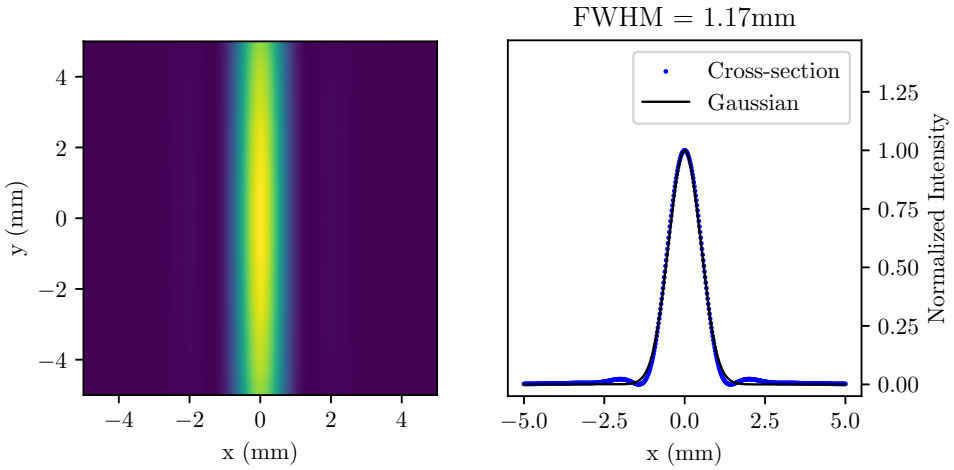

Figure 5.2: Line illumination intensity and cross-section profile when produced from a cylindrical lens, resulting in a FWHM of 1.17 mm.

Simulation of the cylindrical lens takes the input THz Gaussian beam and passes through the described cylindrical lens. The THz field is then propagated to a distance f from the front surface of the cylindrical lens, where it undergoes line focusing in the direction perpendicular to the axis of the cylinder, producing a line illumination at the focal plane. The resulting illumination and cross-section profile is shown in Figure 5.2

As the cylindrical lens focuses the input Gaussian beam in one dimension, the resulting profile is also Gaussian in nature. Using a $f = 75$ mm lens produces a line illumination with a FWHM of 1.17 mm.

5.4.2 Projected sub-diffraction slit

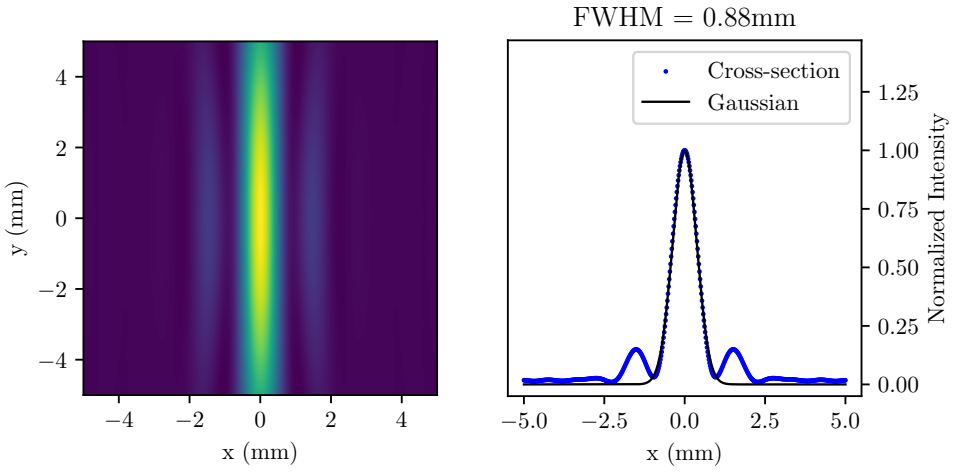

Figure 5.3: Line illumination intensity and cross-section profile when produced from an imaged sub-diffraction slit, resulting in a FWHM of 0.88 mm.

To simulate the projected sub-diffraction slit approach, the input THz beam is masked by a $\lambda/2$ wide vertical slit. Two spherical plano-convex lenses, each of focal length $f = 75$ mm, are placed a distance of f from the mask. The placement position is with respect of the front surface of the first relay lens, to account for the thickness of the lens. The simulation then propagates the input THz beam out to f distance from the front-surface of the second relay lens. The intensity field and cross-section profile of the projected line illumination is shown in Figure 5.3.

The output of the image relay is a line illumination, with a cross-section of the Airy profile. This arises from the diffraction of the THz beam through the sub-diffraction wide slit. To determine the line illumination width, a Gaussian was fitted to its cross-section, yielding a FWHM of 0.88 mm.

5.4.3 Comparison

In comparison, the sub-diffraction slit approach produces the line illumination with the narrower FHWM when compared to the cylindrical lens.

More importantly, it is the approach that produces a line-illumination that is narrower than the FWHM of the THz imaging system's Point Spread Function (PSF). Therefore, the narrow illumination does not degrade the resolution of the imaging system which is ultimately limited by the broader PSF. This is not true for the cylindrical lens approach, as the FWHM is larger than the imaging systems PSF.

Therefore, the sub-diffraction slit approach will therefore be used in the following simulations and experimental implementations.

However, one caveat of the sub-diffraction slit approach, is the addition of side-peaks from the first maxima of the Airy profile. These additional maxima leads to off-axis illumination, which contributes as a source of noise and interference during modulation and VSD reconstruction. To prevent this, the image scan can be cropped to a narrow Region of Interest (ROI) that spans between the first Airy minima, therefore rejecting the off-axis illumination. This approach has been shown in other VSD implementations [103, 105] and shown later in Figure 5.8.

5.5 Simulation

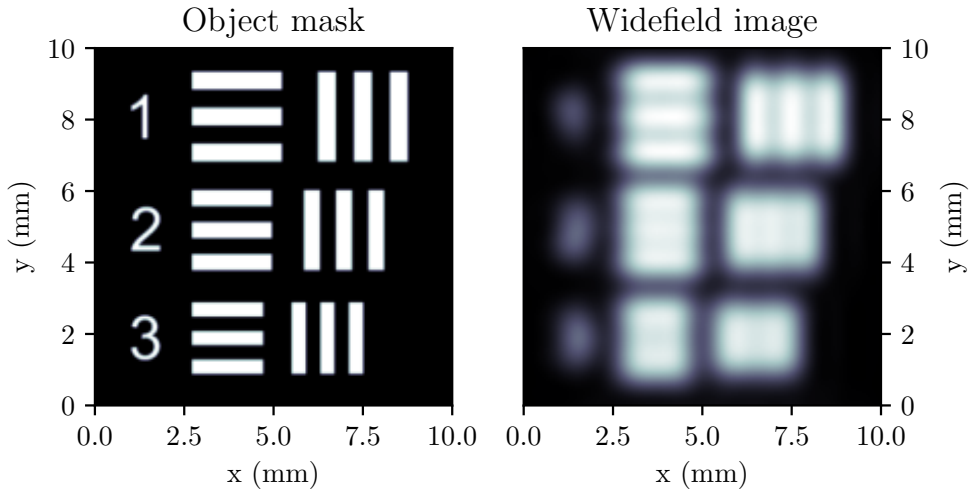

Figure 5.4: USAF target mask used in the simulation, with the outputted widefield image. Only Element 1 remains resolvable in the widefield as the other Elements have a spatial frequency greater than the cut-off spatial frequency of the system.

To verify the VSD approach, the line-scanning approach is simulated followed by the VSD reconstruction to show it is feasible at the THz band. The parameters of the simulation follows the real performance of the THz imaging system, including a 10×10 mm field of view (FOV) and a spatial resolution of 1.06 mm^{-1}. The Optical Transfer Function (OTF) of the system was modelled by the ideal model introduced by Equation 4.14. An effective pixel size of 40 μm is set by FOV and input image size of 250×250 pixels. This pixel size is sufficiently small enough to ensure the produced super-resolution image is sufficiently sampled by at least the Nyquist sampling limit [110]. The illumination is modelled using the projected sub-diffraction slit approach taken from the previous simulation, providing a line illumination with a FWHM of 0.88 mm.

To easily verify super-resolution, a simulated USAF resolution target is used as the object mask. By imaging USAF resolution elements that cannot be resolved in the widefield, super-resolution can be verified by seeing those elements becoming resolved in the super-resolution result. From the USAF target, Elements 1, 2 and

3 from Group 0 was chosen to be imaged, as these have a corresponding spatial frequency of 1.00 mm^{-1}, 1.12 mm^{-1} and 1.26 mm^{-1} respectively, of which only Element 1 is resolvable under widefield imaging. This is shown in Figure 5.4.

In order to demonstrate resolution improvement along the horizontal, the object target is scanned across the horizontal by a vertical line illumination, corresponding to an orientation angle of $\theta = 0°$. A total number of 250 scans images were produced, with each scan image being multiplied by the appropriate digital modulation mask before being spatially integrated to a one-pixel wide column. Stacking of the 250 scan images results in a 250×250 pixel virtually structured image, as described in Equation 5.6.

This process is repeated to produce two virtually structured images with phases $\phi = 0$ and $\phi = \pi/2$, which allows for the recovery of the two shifted Fourier bands $S(\mathbf{k} \pm \mathbf{p}_\theta)$ and one virtually structured image without modulation for recovery of the central Fourier band $S(\mathbf{k})$. Here, $\mathbf{p}_\theta$ denotes the spatial frequency vector of the digital modulation.

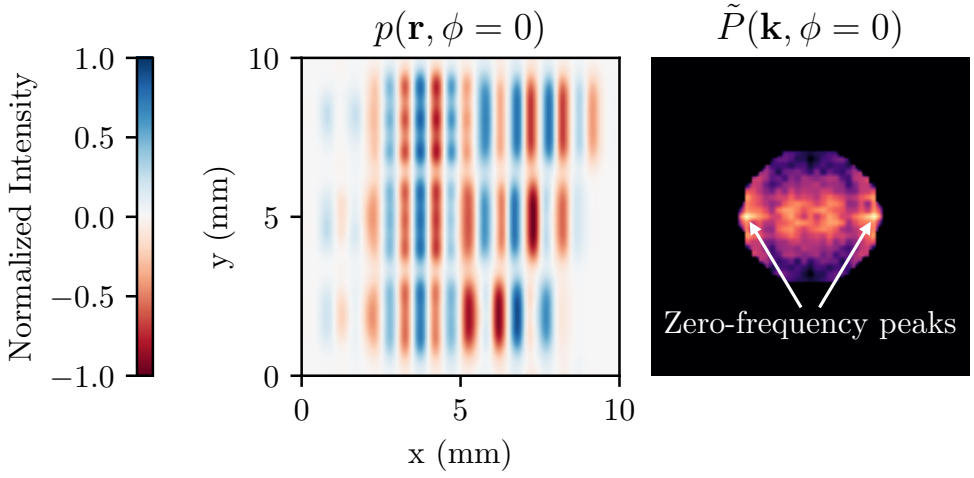

Figure 5.5: Virtually structured image for $\phi = 0$ and respective Fourier spectra, which contains a linear combination of the two shifted Fourier bands $S(\mathbf{k} \pm \mathbf{p}_\theta)$. These two bands are identified by the two shifted zero-frequency peaks.

Figure 5.5 shows the produced virtually structured image for $\phi = 0$. It should be noted that the resulting virtually structured image is unlike the SIM structured images seen in Chapter 4. These phase images are instead bound between $[-1, 1]$. Because the modulation is applied digitally, the resultant intensity values in our image can be negative and therefore avoid any DC component in the modulation (the mean average of the modulation is zero). The consequence of this is shown in the Fourier transform, $\tilde{P}(\mathbf{k}, \phi = 0)$, which lacks the central Fourier band component $S(k)$ which arises from the DC component of the modulation. Instead, $\tilde{P}(\mathbf{k}, \phi = 0)$ is just a linear combination of the two shifted Fourier bands $\tilde{S}(\mathbf{k} \pm \mathbf{p}_\theta)$. This is observed by the two bright peaks in the Fourier spectra. The bright peaks correspond to the zero spatial frequency component from the object's Fourier spectra $S(\mathbf{k})$ that have been shifted with $S(\mathbf{k} \pm \mathbf{p}_\theta)$. This is the expected result of Equation 5.9, and ultimately allows for easier and more accurate separation of the encoded Fourier bands.

The generated virtually structured images can be then used to recover the three Fourier bands $S(\mathbf{k})$ and $S(\mathbf{k} \pm \mathbf{p}_\theta)$ through the use of Equation 5.10 and Equation 5.11. From here, the outlined SIM reconstruction process from Chapter 4 can be used to construct the super-resolution image which is shown against the comparative widefield image in Figure 5.6.

As seen, the widefield image is unable to resolve all but Element 1 from the portion of USAF target imaged. In comparison, the VSD super-resolution image easily resolves the vertical bars in all three Elements, demonstrating an improvement in resolution beyond the diffraction limit of the system. In this case, only the vertical bars become resolved, as the resolution improvement has only been attained along the horizontal scan direction. This fact is reflected in the Fourier spectrum of the VSD image, which shows an increased extent in the horizontal direction but not in the vertical direction when compared with the Fourier spectrum of the widefield image. The VSD image also shown minimal image artifact, due to precisely knowing the spatial frequency and phases of the digital modulation exactly.

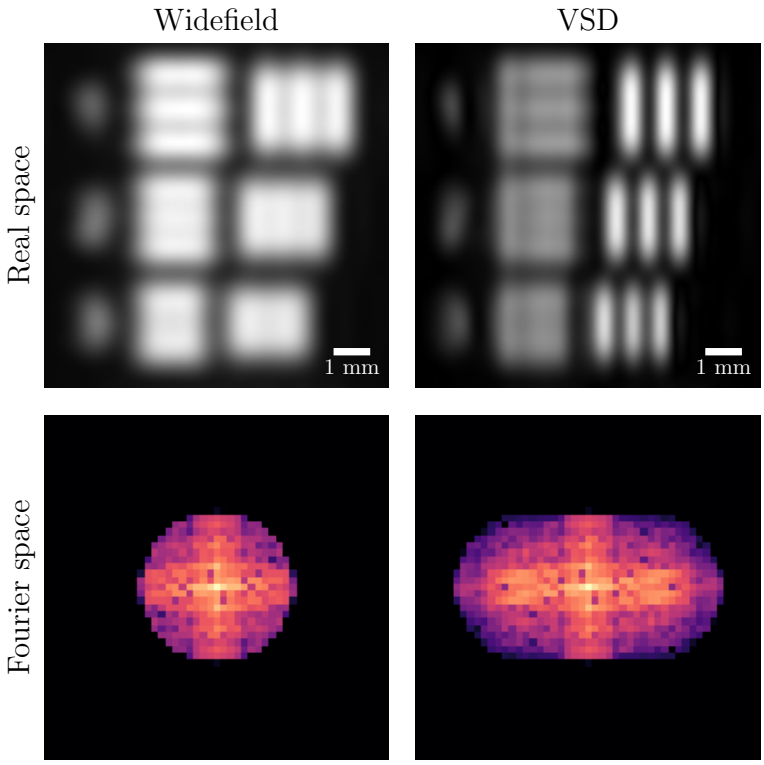

Figure 5.6: Simulation of the VSD process under the THz imaging conditions for the USAF resolution target, showing Elements 1, 2 and 3 from Group 0.

Unlike the simulation of SIM in Chapter 4, deconvolution is not applied to the results. This is to keep consistent with later experimental results and, as discussed in Chapter 4, is a well studied aspect of SIM that ultimately detracts from the evaluation of the effectiveness of these super-resolution techniques at the THz band.

Overall, this simulation verifies, like SIM, that VSD is a feasible technique for use at THz band. A sub-diffraction slit is used to produce narrow line illumination which, when scanning a target object under the VSD process, enables reconstruction of diffraction-beating super-resolution images.

5.6 Experimental Implementation

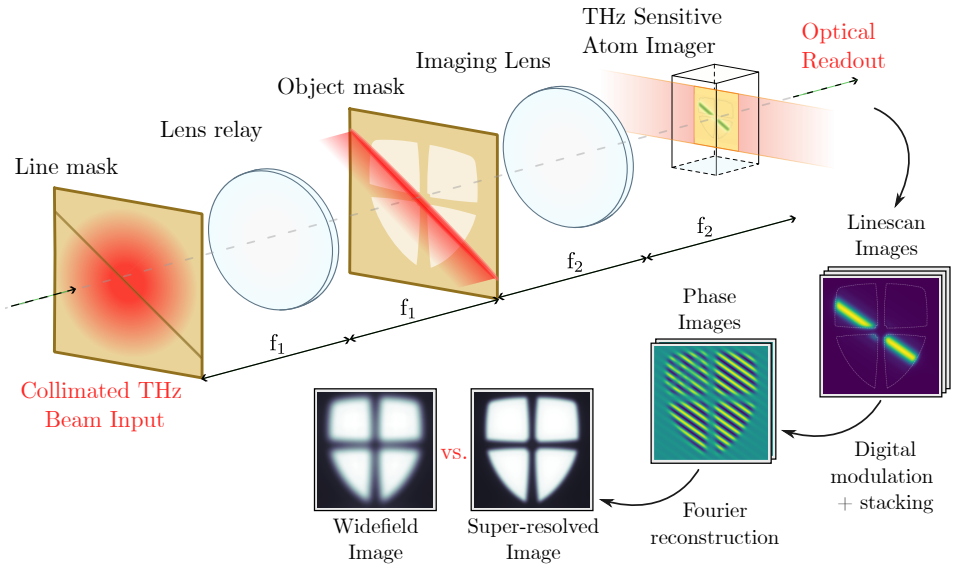

Figure 5.7: Experiential layout for THz VSD through the sub-diffraction slit approach. For clarity, only the THz optics are shown. A more extensive experimental setup was described in Chapter 2.

With insight into how THz VSD can be implemented, the method was subsequently realised experimentally. The setup is shown in Figure 5.7. For clarity, only the THz optics are shown, with the THz source, infrared lasers and optical readout camera that are described in Chapter 2 omitted.

The required line-illumination profile is generated through the line mask approach. A sub-diffraction wide, 250 μm slit mask, produced from machined copper-clad FR4 board, is illuminated by the collimated THz source. To project the line-illumination onto the object plane, an image relay consisting of two aspheric PTFE plano-convex lenses ($\mathrm{d} = 50.8$ mm, $\mathrm{f} = 75$ mm) are used. Using a pair of plano-convex lenses, rather than a single biconvex lens, provides independent focusing of each side of the image relay, aiding with alignment and optimization of the line-illumination. In order to orientate the line-illumination, the line mask was mounted to a manual rotation stage, allowing the scan angle θ to be manually set between each scan.

Transmissive binary masks were used as the target object. Like the line-illumination

mask, the target mask was machined from copper-clad FR-4 board. The masks were placed at the imaging plane of the THz imager, which coincides with the output plane of the line-illumination relay.

Optical implementations of VSD [103–105] use a complex beam scanning approach, sweeping the line-illumination across the target object. These systems must scan the beam across the object, and then de-scan the beam such that the position of the illumination beam remains fixed on the imaging sensor. To keep the process simple, the object is instead swept through the line illumination. This is similar to the approach taken in Chapter 4 for SIM. A pair of translation stages (Thorlabs MTS50-Z8) are used to translated the target mask through the fixed line-illumination. For a given line-illumination orientation, the mask is translated along a path that is orthogonal to the illumination line.

The previously described i2S Silicon THz objective lens ($\mathrm{d} = 60$ mm, $\mathrm{f} = 70$ mm) is used to image the line-illuminated target mask. The atom based THz imager continues to operate as described in Chapter 2. For each scan, the optical readout camera was set to a 200 ms exposure, this was judged to produce a sufficiently high signal-to-noise while keeping acquisition times sensible.

5.6.1 Calibration

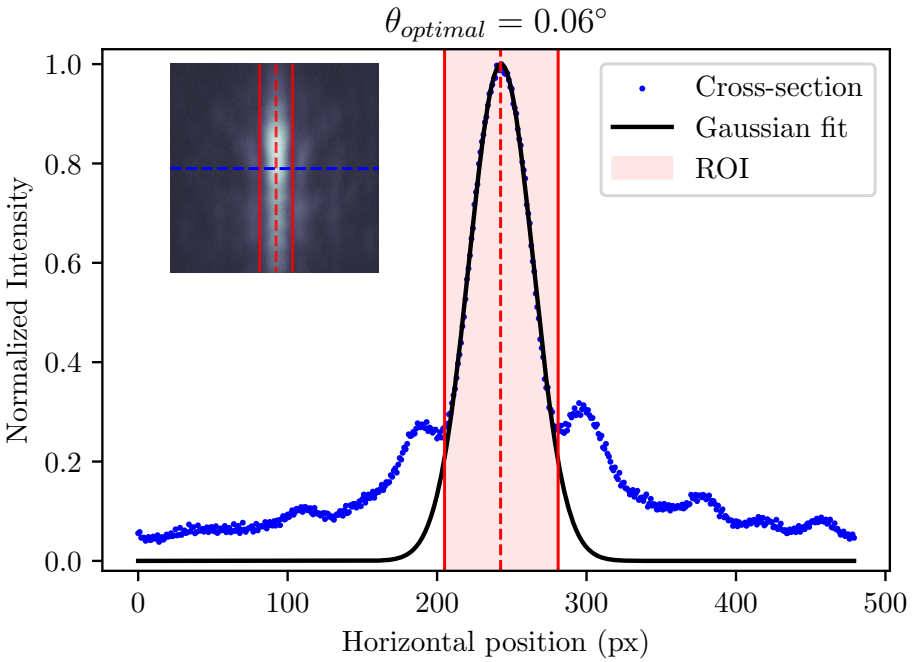

Figure 5.8: Cross-section of the line-profile illumination used for calibration. This helps determine the orientation and center-position of the illumination and an the optimal Region of Interest (ROI) crop region. The inset shows the illumination calibration image, with the sampling cross-section line (blue) and the line-centre and ROI (red).

Prior to scanning and reconstruction of the target mask, the system must be calibrated to determine the line centre, orientation, and width of the line illumination. Without any target object in the imaging system, the line illumination to directly imaged, allowing for calibration. This is done by taking a cross-section of the line illumination to produce an illumination profile, as shown in Figure 5.8. A Gaussian profile is then fitted to cross-section data.

To determine the orientation angle of the illumination, the angle of the cross-section sampling line (shown by the blue line in the inset), is optimized such that the Gaussian profile width is at a minimum. Calibration of the illumination orientation is important to ensure the target mask is translated exactly perpendicular to the illumination. As seen in Figure 5.8 the illumination angle can be calibrated by hand to within at least 0.1°, which is sufficiently accurate.

Calibration also provides the line-centre position of the illumination, enabling precise alignment of the target mask before translation. This ensures that the mask is scanned across the illumination in a way that centres it in the reconstructed image.

Finally, the calibration step allows for the Region of Interest (ROI) to be determined. This marks the region to where each individual image scan is cropped down to, which is used to reject background noise without rejecting part of the signal.

This final ROI cropping step is advantageous when working with sub-optimal line illuminations, as seen in Figure 5.8 in where the illumination profile of the line illumination does not appear strictly Airy, as the side peaks are much larger than expected when compared with simulation (see Figure 5.3). For this work, the ROI is chosen such that it coincides with the first minimum of the Airy profile. This allows for maximum signal from the central peak of the Airy profile while rejecting unwanted diffracted illumination from the side lobes. This is inline with the VSD technique in [103] and [105].

5.7 Results

To assess the performance of the VSD method, two distinct set of masks were manufactured and imaged. The first set consisted of a USAF resolution target, which was used for quantitative measurement of resolution enhancement (as discussed in Chapter 3). The second set comprised image masks designed to demonstrate the qualitative improvements achieved through isotropic resolution enhancement. These two sets allowed for a comprehensive evaluation of the VSD technique, both in terms of its ability to quantitatively improve resolution and its capacity to produce isotropic improvements across multiple axes.

5.7.1 USAF Target

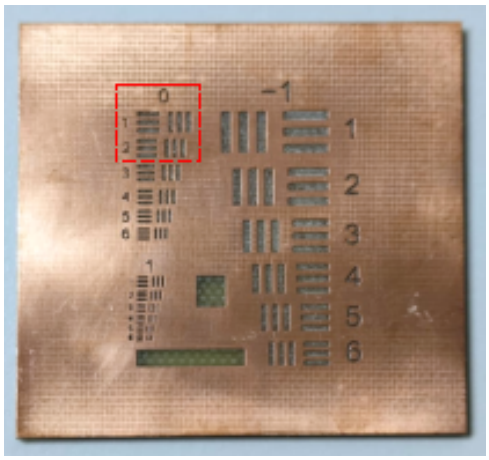

Figure 5.9: Photo of USAF target manufactured for this work. This was introduced in Chapter 3 as Figure 3.10 as the *de facto* target for super-resolution imaging. For 0.55 THz the copper surface is reflective whilst the underlying FR4 substrate is transparent, making it an ideal tranmission mask material.

The same USAF target as manufactured in Chapter 3 was used, reminder of this target is shown in Figure 5.9. For imaging, the highlighred Elements 1 and 2 from Group 0 were selected. These elements correspond to line pairs per millimetre (lp/mm) of 1.00 lp/mm and 1.12 lp/mm, respectively and were chosen as they

exist either side of the widefield resolution threshold. Hence, Element 1 should be resolved but Element 2 should not be.

The imaging was performed in both widefield and VSD modalities for comparison. For the VSD reconstruction, the target was scanned along the horizontal direction across the 8.5 mm field of view. A total of 48 image scans were taken, to produce an effective pixel size of 177 μm and a reconstructed image size of 48×48 pixels. The effective pixel size is over four times smaller than the widefield spatial resolution. This means the super-resolution image will be sufficiently sampled to satisfy the Nyquist sampling limit, as the pixel size will be at least two times smaller than the spatial resolution. The image won't also be grossly oversampled, therefore we can be confident no pseudo resolution enhancements occur through over-sampling our target. A comparative widefield image was taken by removal of the line illumination mask and cropped to ensure both super-resolution and widefield images had the same field of view.

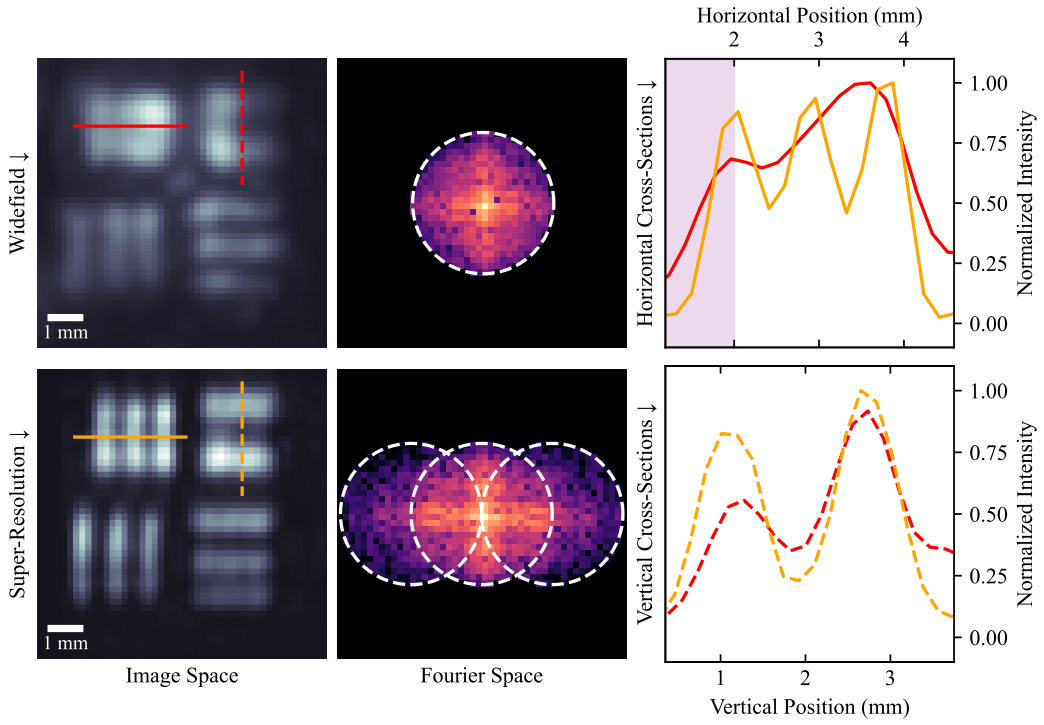

Figure 5.10: Comparison of the widefield and super-resolution images of the USAF target. Horizontal and vertical cross-sections are taken from each image for comparison. Additionally, the respective Fourier spectra of each image is shown.

Figure 5.10 presents a comparison of the widefield and super-resolution images, their respective Fourier spectra and cross-sections the the horizontal and vertical bars of Element 2.

The horizontal cross-sections (shown by the solid line plots) demonstrates that Element 2 is unresolved in the widefield image, but well resolved in the super-resolution image with a mean fringe contrast of 55%. This indicates an improvement in horizontal spatial resolution, and therefore successful super-resolution. The fact that Element 2 is now resolved in the super-resolution image shows we have increased the cut-off spatial frequency of the image beyond the diffraction limit.

As expected, the cross-section of the vertical bars of Element 2 (shown by the dashed line plots) shows that in both the widefield and super-resolution image the element is unresolved, with the middle bar of the element missing in both cross-sections. While the horizontal lines in the super-resolution image demonstrate improved contrast and uniformity, this does not conclusively show super-resolution in the horizontal direction. Instead, this shows that through the scanning process, the super-resolution image receives a more uniform illumination. This in contrast with the widefield image, which receives an illumination with a 2D Gaussian profile, leading to reduced contrast at the edges of the image. Overall, the fact that the horizontal elements remain unresolved is consistent with the fact that the resolution improvement is only attained in the scan direction, and therefore in this case, only along the horizontal axis.

More evidence for super-resolution is found in the Fourier spectra of the images. For clarity the extent of each recovered Fourier band is outlined with a contour. The Fourier spectra of the widefield images consists of the single central Fourier band, and the Fourier spectra of the super-resolution images consists of three bands; the central band and two additional recovered Fourier bands, expanding the spectral extent across the horizontal axis. The Fourier spectra of the super-resolved image shows extended structure, corresponding to recovered higher spatial frequency information which leads to the observed improvement in image resolution.

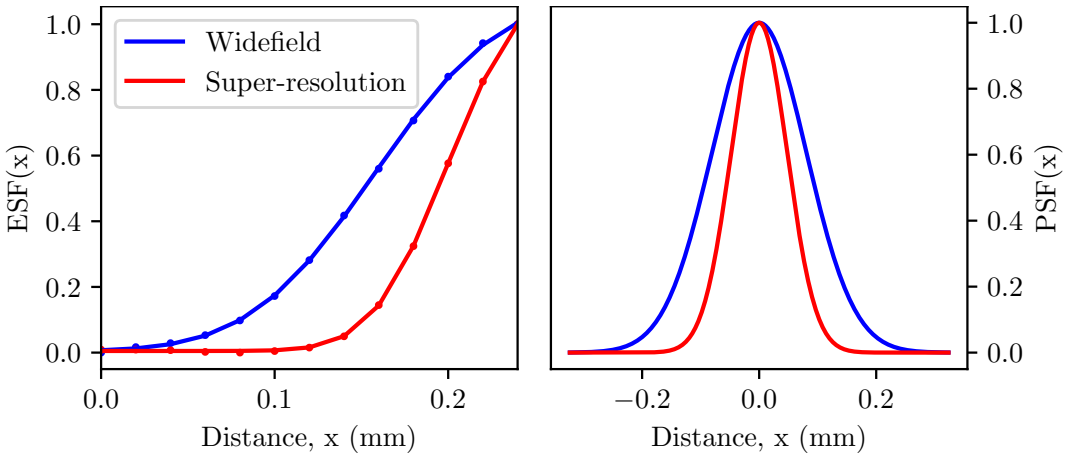

Figure 5.11: Measured and calculated Edge Spread Function and Point Spread Function for the widefield and super-resolution images.

Quantitative measurement of the resolution improvement can be done by analysing the edge profile of one of the bars, this process was discussed in Chapter 3. The edge profile is highlighted by the purple shaded region on the horizontal cross-section.

A Gaussian error function was fitted to the edge profile of both the widefield and super-resolution images to attain the effective Edge Spread Function (ESF) which is then differentiated to produce the effective Point Spread Function (PSF). The Full Width Half Maximum (FHWM) of the PSF could be then measured to provide a measure of the image resolution. This approach produces a resolution metric that is defined by the Rayleigh criterion. The ESF and resultant PSF of the widefield and super-resolution images is shown in Figure 5.11.

The measured FWHM of the widefield and super-resolution image was determined to be 0.94 ± 0.01 mm and 0.54 ± 0.01 mm respectively. This implies a resolution improvement of $\times 1.74 \pm 0.03$, demonstrating effective super-resolution. These values validate the qualitative observations, as our widefield resolution limit is equivalent to a spatial cut-off frequency of 1.06 mm^{-1}. This explains why Element 2 cannot be resolved, as its spatial frequency is beyond the widefield's cut-off frequency. Conversely, the super-resolution image has an spatial cut-off frequency of 1.82 mm^{-1}

which is why Element 2 becomes well resolved. As the new cut-off frequency is much higher than the spatial frequency of Element 2, the horizontal bars can be well resolved with high contrast.

The final improvement in resolution is less than the two-fold theoretical maximum. The deviation from the theoretical value is attributed to the presence of image noise and the attenuation of high spatial frequencies in the Fourier domain by the Optical Transfer Function (OTF). Both of these factors are corrected for by the omitted deconvolution step. Therefore the resolution of the super-resolution image could be enhanced further through post-processing.

5.7.2 Image Icon Targets

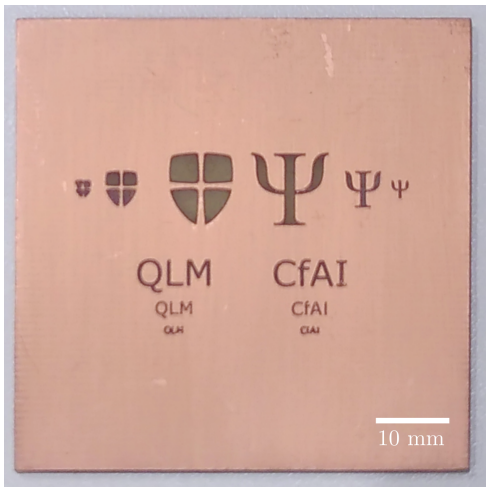

Figure 5.12: Photo of manufactured icon target. Of the two icons used, Ψ and the Durham University shield, the largest variants of the icons were used. A 10 mm scale bar is included for scale.

Two icon targets were chosen from imaging: the Durham University shield and the Greek letter Ψ, as shown in Figure 5.12. The largest icon of each was used as they measured 8.5 × 9.7 mm, and therefore maximize the coverage across the field of view of the THz imager.

The icon image targets were scanned along three equally spaced axes at angles $\theta = 0°, 60°, 120°$, in order to reconstruct an image with near-isotropic resolution improvement. This was achieved by rotating the illumination mask to the required orientation and translating the image mask in a direction normal to the line illumination. Each scan axis consisted of 48 individual scan images, allowing for resolution improvement along each axis. In total, 144 full-frame images were required to generate one super-resolution image with a 10×10 mm field-of-view. This produced a final reconstructed image with a size of 48×48 pixels, with an effective pixel size of 208 μm. Again, this is pixel size is small enough to ensure the super-resolution image is properly sampled.

For reconstruction, each orientation could be reconstructed independently, before being combined into final near-isotropic super-resolution image. The independent super-resolution images for each orientation is shown in Figure 5.13.

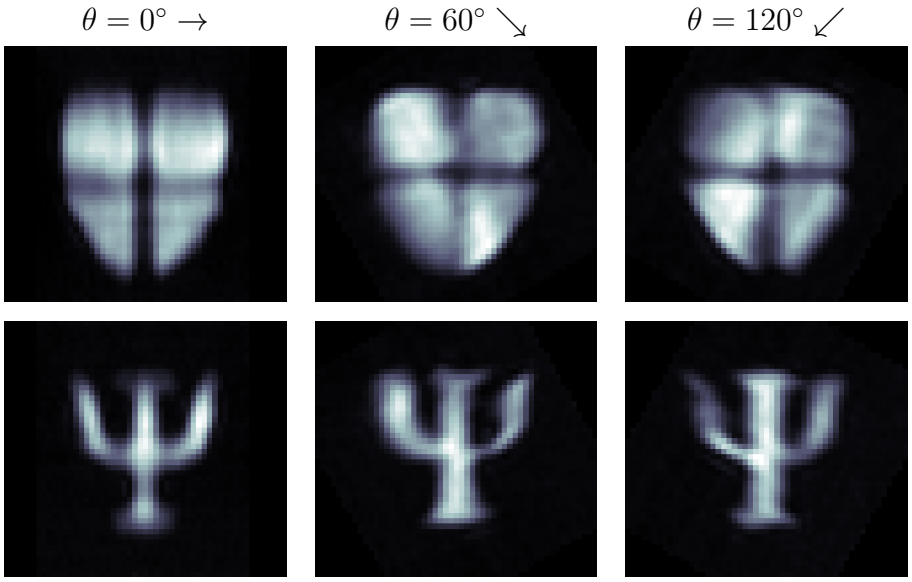

Figure 5.13: Super-resolution images produced from scans for each given orientation. Each scan produces super-resolution along the scan axis. The combinations of the three orientations produces a near-isotropic super-resolution image.

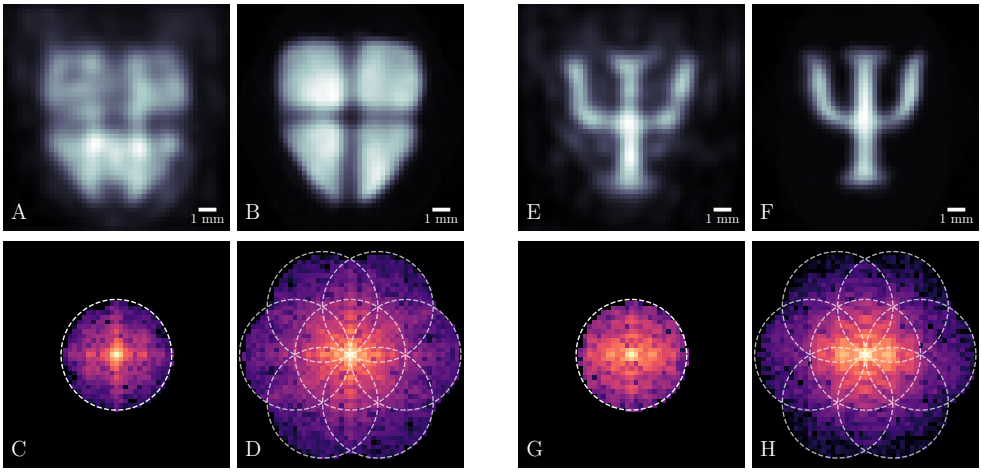

(a) **(b)**

Figure 5.14: Comparison of comparative widefield images (A, E) with super-resolution images (B, F) of the two icon targets: the Durham University shield and the Greek letter Ψ. The Fourier spectra of each image shown below the respective image with appropriate contours for each Fourier band.

Each scan orientation demonstrates super-resolution along the scan axis, this is is particular noticeable on the edges of the Durham shield. Different edges are sharper in each of the orientations, with edges perpendicular to the scan direction being sharper than those that are parallel.

The individual orientations also show the Gaussian profile of the line illumination, resulting in differing illumination of the target mask. This ultimately averages out once the three orientations are combined. This, alongside comparative widefield images are shown in Figure 5.14.

Comparison of the widefield and super-resolution images for the Durham shield (A and B) and the Ψ (E, F) show a clear notable improvement in image resolution. The super-resolution images exhibit finer details and improved image contrast at the masks edges. For the Durham shield, the cross is now clearly defined and resolved for both the horizontal and vertical bars, demonstrating the resolution improvement applies to all directions. For the Ψ the curves of the arms are better defined.

Unlike SIM, both super-resolution results are artefact free. This is owing to the post-process modulation of the raw input images, which means the phase of each modulation is known exactly, which eliminates any reconstruction artefacts that arise from phase-errors. Additionally, the frequency of the modulation is both known and absolute. That is, there are no additional spatial frequencies in the modulations, unlike in Chapter 4 during the SIM reconstruction. The spatial frequency of the modulation was maximised such that it is equal to the spatial cut-off frequency of the imaging system. This allows for the maximum shifting of the Fourier bands and therefore the largest improvement in the Fourier spectra extent.

The extent and therefore resolution improvement is apparent by looking at the Fourier spectra for the super-resolution images (D and H) which are constructed using seven distinct Fourier bands: two shifted bands per scan axis, along with a central band. In this reconstruction, the central Fourier band is recovered three times, once per orientation and therefore this is accounted for when the bands are averaged together.

Each Fourier band is highlighted by a contour, showing the extent of the band. This extent is determined from the cut-off spatial frequency of the imaging system. The overlap of the contours at the centre of the spectra shows each additional Fourier band is shifted exactly by cut-off spatial frequency, which leads to the doubling of the Fourier extent.

Again, we omit the deconvolution step from the reconstruction process in order to evaluate the merits of VSD without the aid of additional computational enhancement.

5.8 Conclusion

This chapter explored the concept of Virtually Structured Detection (VSD), a line-scanning variant of Structured Illumination Microscopy (SIM). The theory of VSD and outlined and demonstrated, showing how the VSD process leads to the formation of the same structured image phases used in SIM. This allowed for super-resolution reconstruction from our VSD images using the same approach as seen with SIM in Chapter 4.

The approach was verified through simulation. One set of simulations to determine the best approach to generate the required line illumination, and another simulation to verify the VSD method. As with SIM, VSD appeared to be applicable at the THz frequencies to attain a theoretical two-fold improvement in resolution.

VSD was then experimentally implemented, time was taken to consider the calibration process required to ensure an accurate scanning process. Initially, quantitative single axis super-resolution was achieved by horizontally scanning the USAF target which demonstrated a $\times 1.74 \pm 0.03$ improvement in resolution. Finally, near-isotropic resolution was demonstrated by changing the orientation of the illumination beam and scan direction.

The results outlined here confirm the capability of VSD to enhance the resolution of THz imaging systems, particularly by leveraging isotropic resolution improvements across multiple scan axes. This could be leveraged by application requiring both the high penetrating properties of low-frequency THz illumination [111] and high-spatial resolution. One use case includes the inspection of manufactured circuit boards and microprocessors [3].

It was recognized that VSD is inherently slower than the widefield SIM approach due to its scanning-based imaging nature. Therefore, VSD will continue to need many more images per reconstruction, and therefore longer acquisition times. This fact is especially true for our current implementation, as the acquisition speed is

ultimately limited by the speed of the translation stages. This approach was chosen for its minimal complexity, in order to easily demonstrate super-resolution at the THz band. Optical implementations of VSD demonstrate much faster acquisition through the use of beam-scanning and synchronized wide-field cameras [103, 105]. In theory, there is no limitation that would prevent such an approach in future THz VSD work.

Chapter 6

Conclusion and Outlook

From this work, there are several aspects that could be further explored and improved. For super-resolution imaging, this includes improved experimental and reconstruction implementations. There is also scope for additional imaging techniques that arise from using a structured illumination. Such ideas are briefly explored for their potential as future works.

6.1 Image Deconvolution

For this work, the deconvolution step has been omitted from the reconstruction of experimental data, in both the SIM and VSD approaches. This was intentional on two counts. One, to be able to evaluate the super-resolution technique without the inclusion of computational enhancement. And two, the use of binary masks makes deconvolution, in many senses, trivial and meaningless. For example, with the prior knowledge of the target being a binary mask, a simple threshold of the image would recover a binary image. Such image would have perfect contrast and absolute resolution, defeating the purpose of the super-resolution technique.

Overall, the deconvolution of images is a well-known concept, and has been shown to work successfully not only in SIM, but across the wider microscopy field [112] and beyond [113–115]. It is therefore expected that it would apply equally well to the

THz band. Within the THz domain, image deconvolution has only been explored for images generated by raster-scanning objects in a THz Time-domain Spectroscopy (TDS) system [116–119]. Therefore there is scope for exploring deconvolution on THz images from focal-plane array detector, such as our atom based system. For the context of super-resolution imaging, this would be worthwhile when applied to real-world applications.

6.2 Improved Widefield Structured Illumination

As seen in Chapter 4, the widefield SIM technique showed promising results, but was ultimately hindered by unwanted additional spatial frequencies in the structured illumination generated by the Fresnel biprism.

A higher quality illumination, one that is sinusoidal at a single spatial frequency, would be improve the widefield SIM approach. One approach would be following the more traditional two-beam interference route. The illumination source could be split using a 50:50 beamsplitter to generate the two beams. One beam at on-axis incidence and the other at off-axis incidence to the target object. Better illumination would help eliminate the artifacting seen during reconstruction, and therefore lead to more successful SIM imaging.

6.3 Beam-scanning Virtually Structured Detection

Chapter 5 showed successful implementation of the VSD technique as a proof of concept. In the present form, the technique is not very practical due to the long acquisition times to generate one super-resolution image. This is because of the object-translation approach of the imaging scanning is slow, and the longest part of the acquisition process.

To leverage the high-speed capabilities of the imaging system, a better option would be a beam-scanning approach, as demonstrated in [103–105]. The cost of

this approach is increases complexity in the illumination system, however through the use of fast galvo-steering mirrors, the THz line illumination could scan across a stationary object, while the THz imaging system runs at high-speed. Despite the need for 100's of raw images per super-resolution reconstruction, the high frame-rate capability of the THz imaging system could still allow for video-rate super-resolution imaging.

6.4 Other Structured Illumination Technqiues

The use of structured illumination is not unique to super-resolution imaging, and has been used in the optical successfully for a variety of other applications. These applications could prove to be successful and useful at the THz band.

6.4.1 Optical Sectioning

Optical sectioning via structured illumination is another microscopy derived technique. Where SIM uses structured illumination to improve lateral resolution, OS uses structured illumination to help reject out-of-focus light, and therefore improved the axial (depth) resolution. Optical sectioning is used in microscopy to image through thick specimens, which scatter the illumination. Such a technique could be translated to widefield THz imaging, especially in non-destructive testing applications where imaging within a target object is required.

6.4.2 THz Off-Axis Holography

THz off-axis holography works by generating structured fringes by interference of the incoming THz field with an off-axis reference plane wave at the detector plane. This differs to SIM, which generates structured fringes at the imaging plane, in order to encode high-spatial frequency information. Instead, the phase information

of the incoming THz field is encoded, and through reconstruction the complex-field can be recovered from a single image.

This would enable high-speed widefield complex-field imaging, which would have useful applications in that can leverage the phase-information from an object of interest.

Recovering the complex-field can also be used to achieve lensless imaging, as the complex-field can be back-propagated to an imaging arbitrary plane. Through lensless imaging, the effective numerical aperture of the system is inherently higher, as it is only bound by the illumination. As a result, the overall diffraction-limited resolution would be higher.

6.5 Conclusion

To conclude this thesis has explored and demonstrated structured illumination super-resolution imaging at the THz band, an application of structured light that enables imaging beyond the diffraction limit.

This work demonstrates the promising use of structured light in the THz domain to achieve sub-diffraction image resolution while preserving the key advantages of THz radiation, such as material contrast and penetration depth. By leveraging the speed and sensitivity of our atom-based widefield THz imaging system, structured illumination has been successfully implemented at 0.55 THz. Other work has explored such concepts at the longer microwave wavelength [120], but has been limited to just simulation. Therefore this work represents the longest wavelength at which SIM super-resolution has been experimentally realised.

This advancement opens new opportunities in application areas where fine detail must be resolved beneath the diffraction limit. In particular, it offers a powerful tool for non-destructive evaluation of layered dielectric structures in semiconductors [121]. Its compatibility with widefield acquisition also makes it well-suited to

real-time imaging scenarios such as security screening [8] and industrial inspection [5]. In extending advanced optical techniques into the THz regime, this work contributes meaningfully to both THz imaging and the broader field of structured light research.

Appendix **A**

Fourier Domain Shifting

The shifting of our Fourier domain of the sample object $\tilde{S}(\mathbf{k})$ is the result of combining the *δ-function convolution theorem* and the *Fourier shifting theorem.*

Fourier Shift Theorem

$$\mathcal{F}\{f(\mathbf{r}-\mathbf{r_0})\} = e^{-i\mathbf{k}\cdot\mathbf{r_0}} \cdot \tilde{F}(\mathbf{k}) \tag{A.1}$$

The Fourier shift theorem shows that a lateral shift in real space $\mathbf{r}_0$ leads to a global phase in the Fourier domain.

δ-function Convolution Theorem

$$\int_{\infty}^{\infty} f(\mathbf{r})\delta(\mathbf{r}-\mathbf{r_0})\,\mathrm{d}\mathbf{r} = f(\mathbf{r_0}) \tag{A.2}$$

The δ-function convolution theorem shows that convolving a function with a delta function of parameter $\mathbf{r_0}$ evaluates the functions at $\mathbf{r_0}$.

Fourier Domain Shifting

We start by considering the Fourier transform of our function $f(\mathbf{r})$

$$\tilde{F}(\mathbf{k}) = \int_{-\infty}^{\infty} f(\mathbf{r})e^{-i\mathbf{k}\cdot\mathbf{r}}\,\mathrm{d}\mathbf{r} \tag{A.3}$$

If we convolve $\tilde{F}(\mathbf{k})$ with our δ-function $\delta(\mathbf{k} - \mathbf{k_0})$, the phase term of the Fourier transform is fixed at $\mathbf{k_0}$. By the defintion of the Fourier shift theorem, this is therefore a translation of the Fourier spectra by $\mathbf{k_0}$.

$$F(\mathbf{k}) \otimes \delta(\mathbf{k} - \mathbf{k_0}) = \int_{-\infty}^{\infty} \int_{-\infty}^{\infty} f(\mathbf{r}) e^{-i\mathbf{k}\cdot\mathbf{r}} \cdot \delta(\mathbf{k} - \mathbf{k_0}) \, \mathrm{d}\mathbf{r} \, \mathrm{d}\mathbf{k} \tag{A.4}$$

$$= \int_{-\infty}^{\infty} f(\mathbf{r}) e^{-i\mathbf{k_0}\cdot\mathbf{r}} \, \mathrm{d}\mathbf{r} \tag{A.5}$$

$$= F(\mathbf{k} - \mathbf{k_0}) \tag{A.6}$$

Appendix B

VSD Convolution

In VSD, we observe that by spatially integrating our scan image, we appear to induce a convolution that we exploit for super-resolution imaging. Conceptually, the convolution arises from the physical scanning process. By scanning the object with our line illumination, we are in effect convolving the object with the illumination.

To be more specific to our use-case, we scan the object rather than the illumination. Therefore the true, actual position of the object $s_{\text{actual}}(\mathbf{r})$ is shifted by a displacement $\mathbf{r_0}$ by the translation stages.

$$s_{\text{actual}}(\mathbf{r}) = s(\mathbf{r} - \mathbf{r_0}) \tag{B.1}$$

If we apply this to Equation 5.4, we find

$$p_i(\mathbf{r}) = \iint m(r) \cdot [h_{il}(\mathbf{r}) \cdot s_{\text{actual}}(\mathbf{r})] \otimes h_{de}(\mathbf{r}) \; d\mathbf{r} \tag{B.2}$$

$$= \iint m(r) \cdot [h_{il}(\mathbf{r}) \cdot s(\mathbf{r} - \mathbf{r_0})] \otimes h_{de}(\mathbf{r}) \; d\mathbf{r} \tag{B.3}$$

By considering that translating our object is equivalent to translating our illumination across the object, we can write

$$p_i(\mathbf{r}) = \iint m(r) \cdot [h_{il}(\mathbf{r} - \mathbf{r_0}) \cdot s(\mathbf{r})] \otimes h_{de}(\mathbf{r}) \; d\mathbf{r} \tag{B.4}$$

Where $h_{il}(\mathbf{r} - \mathbf{r_0})$ is now our 'scanning' line illumination. As a result Equation B.4 is a convolution integral with the illumination. Under the properties of the convolution integral, we can therefore write

$$p_i(\mathbf{r}) = [\{m(r) \otimes h_{il}(\mathbf{r})\} \cdot s(\mathbf{r})] \otimes h_{de}(\mathbf{r}) \tag{B.5}$$

Which results in Equation 5.5.

Bibliography

[1] Lucy A Downes. *A high-speed THz imaging system based on THz-to-optical conversion in atomic vapour*. PhD thesis, Durham University, 2020.

[2] Alfred Leitenstorfer, Andrey S Moskalenko, Tobias Kampfrath, Junichiro Kono, Enrique Castro-Camus, Kun Peng, Naser Qureshi, Dmitry Turchinovich, Koichiro Tanaka, Andrea G Markelz, et al. The 2023 terahertz science and technology roadmap. *Journal of Physics D: Applied Physics*, 56 (22):223001, 2023.

[3] Binbin B Hu and Martin C Nuss. Imaging with terahertz waves. *Optics letters*, 20(16):1716–1718, 1995.

[4] Yao-Chun Shen and Philip F Taday. Development and application of terahertz pulsed imaging for nondestructive inspection of pharmaceutical tablet. *IEEE Journal of Selected Topics in Quantum Electronics*, 14(2):407–415, 2008.

[5] Zhanke Yan, Yibin Ying, Hongjian Zhang, and Haiyan Yu. Research progress of terahertz wave technology in food inspection. *Terahertz Physics, Devices, and Systems*, 6373:142–151, 2006.

[6] Sunil K Mathanker, Paul R Weckler, and Ning Wang. Terahertz (thz) ap-

plications in food and agriculture: A review. *Transactions of the ASABE*, 56 (3):1213–1226, 2013.

[7] Q Cassar, CL Koch-Dandolo, Jean-Paul Guillet, M Roux, F Fauquet, JB Perraud, and P Mounaix. Characterization of varnish ageing and its consequences on terahertz imagery: Demonstration on a painting presumed of the french renaissance. *Journal of Infrared, Millimeter, and Terahertz Waves*, 41:1556–1566, 2020.

[8] Michael C Kemp, Antony Glauser, and Colin Baker. Recent developments in people screening using terahertz technology: seeing the world through terahertz eyes. *Terahertz for Military and Security Applications IV*, 6212: 224–233, 2006.

[9] Steven R Murrill, Eddie L Jacobs, Steven K Moyer, Carl E Halford, Steven T Griffin, Frank C De Lucia, Douglas T Petkie, and Charmaine C Franck. Terahertz imaging system performance model for concealed-weapon identification. *Applied optics*, 47(9):1286–1297, 2008.

[10] Ruth M Woodward, Vincent P Wallace, Richard J Pye, Bryan E Cole, Donald D Arnone, Edmund H Linfield, and Michael Pepper. Terahertz pulse imaging of ex vivo basal cell carcinoma. *Journal of Investigative Dermatology*, 120(1):72–78, 2003.

[11] Benjamin St Peter, Sigfrid Yngvesson, Paul Siqueira, Patrick Kelly, Ashraf Khan, Stephen Glick, and Andrew Karellas. Development and testing of a single frequency terahertz imaging system for breast cancer detection. *IEEE Transactions on Terahertz Science and Technology*, 3(4):374–386, 2013.

[12] Udo Kaatze and Christof Hübner. Electromagnetic techniques for moisture content determination of materials. *Measurement Science and Technology*, 21(8):082001, 2010.

[13] Moumita Dutta, Amar S Bhalla, and Ruyan Guo. Thz imaging of skin burn: seeing the unseen—an overview. *Advances in wound care*, 5(8):338–348, 2016.

[14] Priyamvada Tewari, Colin P Kealey, David B Bennett, Neha Bajwa, Kelli S Barnett, Rahul S Singh, Martin O Culjat, Alexander Stojadinovic, Warren S Grundfest, and Zachary D Taylor. In vivo terahertz imaging of rat skin burns. *Journal of biomedical optics*, 17(4):040503–040503, 2012.

[15] Elizabeth Berry, James W Handley, Anthony J Fitzgerald, WJ Merchant, Roger D Boyle, NN Zinov'Ev, Robert E Miles, J Martyn Chamberlain, and Michael A Smith. Multispectral classification techniques for terahertz pulsed imaging: an example in histopathology. *Medical engineering & physics*, 26 (5):423–430, 2004.

[16] Daniel M Mittleman. Twenty years of terahertz imaging. *Optics express*, 26 (8):9417–9431, 2018.

[17] Sung-Liang Chen, You-Chia Chang, Cheng Zhang, Jong G Ok, Tao Ling, Momchil T Mihnev, Theodore B Norris, and L Jay Guo. Efficient real-time detection of terahertz pulse radiation based on photoacoustic conversion by carbon nanotube nanocomposite. *Nature Photonics*, 8(7):537–542, 2014.

[18] Marcel JE Golay. The theoretical and practical sensitivity of the pneumatic infra-red detector. *Review of Scientific Instruments*, 20(11):816–820, 1949.

[19] Yun-Shik Lee. *Principles of terahertz science and technology*, volume 170. Springer Science & Business Media, 2009.

[20] A Samy Saadeldin, Mohamed Farhat O Hameed, Essam MA Elkaramany, and Salah SA Obayya. Highly sensitive terahertz metamaterial sensor. *IEEE Sensors Journal*, 19(18):7993–7999, 2019.

[21] Bo Su and Guoteng Duan. A high sensitivity thz detector. In *International Symposium on Photoelectronic Detection and Imaging 2011: Terahertz Wave Technologies and Applications*, volume 8195, pages 416–422. SPIE, 2011.

[22] Thomas Siday, Polina P Vabishchevich, Lucy Hale, Charles Thomas Harris, Ting Shan Luk, John L Reno, Igal Brener, and Oleg Mitrofanov. Terahertz detection with perfectly-absorbing photoconductive metasurface. *Nano Letters*, 19(5):2888–2896, 2019.

[23] Eui Su Lee, Mugeon Kim, Kiwon Moon, Il-Min Lee, Dong Woo Park, Jun-Hwan Shin, Hyun-Soo Kim, Da-Hye Choi, Kyeong Sun Choi, Dong Hun Lee, et al. High-speed and cost-effective reflective terahertz imaging system using a novel 2d beam scanner. *Journal of Lightwave Technology*, 38(16):4237–4243, 2020.

[24] Rayko Ivanov Stantchev, Xiao Yu, Thierry Blu, and Emma Pickwell-MacPherson. Real-time terahertz imaging with a single-pixel detector. *Nature communications*, 11(1):2535, 2020.

[25] Rayko Ivanov Stantchev and Emma Pickwell-MacPherson. *Spatial terahertz-light modulators for single-pixel cameras*. IntechOpen, 2022.

[26] Geon Lee, Jinwoo Lee, Q-Han Park, and Minah Seo. Frontiers in terahertz imaging applications beyond absorption cross-section and diffraction limits. *ACS Photonics*, 9(5):1500–1512, 2022.

[27] Krunal Radhanpura, David Farrant, and Jia Du. Measurement of agricultural products using terahertz hyperspectral imaging. In *2017 42nd International Conference on Infrared, Millimeter, and Terahertz Waves (IRMMW-THz)*, pages 1–2. IEEE, 2017.

[28] Chen Wang, Ruiyun Zhou, Yuxin Huang, Lijuan Xie, and Yibin Ying. Terahertz spectroscopic imaging with discriminant analysis for detecting foreign materials among sausages. *Food Control*, 97:100–104, 2019.

[29] Hongyi Ge, Ming Lv, Xuejing Lu, Yuying Jiang, Guofang Wu, Guangming Li, Li Li, Zhi Li, and Yuan Zhang. Applications of thz spectral imaging in the

detection of agricultural products. In *Photonics*, volume 8, page 518. MDPI, 2021.

[30] Hua Qin, Jiandong Sun, Shixiong Liang, Xiang Li, Xinxin Yang, Zehao He, Cui Yu, and Zhihong Feng. Room-temperature, low-impedance and high-sensitivity terahertz direct detector based on bilayer graphene field-effect transistor. *Carbon*, 116:760–765, 2017.

[31] Alan WM Lee, Benjamin S Williams, Sushil Kumar, Qing Hu, and John L Reno. Real-time imaging using a 4.3-thz quantum cascade laser and a 320/spl times/240 microbolometer focal-plane array. *IEEE Photonics Technology Letters*, 18(13):1415–1417, 2006.

[32] MA Dem'yanenko, DG Esaev, BA Knyazev, GN Kulipanov, and NA Vinokurov. Imaging with a 90frames/ s microbolometer focal plane array and high-power terahertz free electron laser. *Applied physics letters*, 92(13), 2008.

[33] François Simoens and Jérôme Meilhan. Terahertz real-time imaging uncooled array based on antenna-and cavity-coupled bolometers. *Philosophical Transactions of the Royal Society A: Mathematical, Physical and Engineering Sciences*, 372(2012):20130111, 2014.

[34] Denis Dufour, Linda Marchese, Marc Terroux, Hassane Oulachgar, Francis Généreux, Michel Doucet, Luc Mercier, Bruno Tremblay, Christine Alain, Patrick Beaupré, et al. Review of terahertz technology development at ino. *Journal of Infrared, Millimeter, and Terahertz Waves*, 36:922–946, 2015.

[35] Seiichiro Ariyoshi, Chiko Otani, Adrian Dobroiu, Hiroshi Matsuo, Hiromi Sato, Tohru Taino, Kodo Kawase, and Hirohiko M Shimizu. Superconducting detector array for terahertz imaging applications. *Japanese journal of applied physics*, 45(10L):L1004, 2006.

[36] Artem Kuzmin, Steffen Doerner, Stefan Singer, Ilya Charaev, Konstantin Ilin, Stefan Wuensch, and Michael Siegel. Terahertz transition-edge sensor

with kinetic-inductance amplifier at 4.2 k. *IEEE Transactions on Terahertz Science and Technology*, 8(6):622–629, 2018.

[37] Lucy A Downes, Andrew R MacKellar, Daniel J Whiting, Cyril Bourgenot, Charles S Adams, and Kevin J Weatherill. Full-field terahertz imaging at kilohertz frame rates using atomic vapor. *Physical Review X*, 10(1):011027, 2020.

[38] Lucy A Downes, Lara Torralbo-Campo, and Kevin J Weatherill. A practical guide to terahertz imaging using thermal atomic vapour. *New Journal of Physics*, 25(3):035002, 2023.

[39] Thomas F Gallagher. Rydberg atoms. In *Springer Handbook of Atomic, Molecular, and Optical Physics*, pages 231–240. Springer, 1994.

[40] Jonathon A Sedlacek, Arne Schwettmann, Harald Kübler, Robert Löw, Tilman Pfau, and James P Shaffer. Microwave electrometry with rydberg atoms in a vapour cell using bright atomic resonances. *Nature physics*, 8(11): 819–824, 2012.

[41] C. Wade, Matteo Marcuzzi, Emanuele Levi, Jorge Douglas Kondo, I. Lesanovsky, Charles Adams, and Kevin Weatherill. A terahertz-driven non-equilibrium phase transition in a room temperature atomic vapour. *Nature Communications*, 9, 09 2018. doi: 10.1038/s41467-018-05597-4.

[42] N. Šibalić, J.D. Pritchard, C.S. Adams, and K.J. Weatherill. Arc: An open-source library for calculating properties of alkali rydberg atoms. *Computer Physics Communications*, 220:319–331, 2017. ISSN 0010-4655. doi: https://doi.org/10.1016/j.cpc.2017.06.015. URL `https://www.sciencedirect.com/science/article/pii/S0010465517301972`.

[43] Matthew James Jamieson. *Optimizing a Rydberg atom-based terahertz imaging system.* PhD thesis, Durham University, 2023.

[44] John Broky, Georgios A Siviloglou, Aristide Dogariu, and Demetrios N Christodoulides. Self-healing properties of optical airy beams. *Optics express*, 16 (17):12880–12891, 2008.

[45] Andrew Forbes, Michael De Oliveira, and Mark R Dennis. Structured light. *Nature Photonics*, 15(4):253–262, 2021.

[46] Mats GL Gustafsson. Surpassing the lateral resolution limit by a factor of two using structured illumination microscopy. *Journal of microscopy*, 198(2): 82–87, 2000.

[47] Yuanjie Yang, Yu-Xuan Ren, Mingzhou Chen, Yoshihiko Arita, and Carmelo Rosales-Guzmán. Optical trapping with structured light: a review. *Advanced Photonics*, 3(3):034001–034001, 2021.

[48] Jing Du and Jian Wang. High-dimensional structured light coding/decoding for free-space optical communications free of obstructions. *Optics Letters*, 40 (21):4827–4830, 2015.

[49] Ming-June Tsai and Chuan-Cheng Hung. Development of a high-precision surface metrology system using structured light projection. *Measurement*, 38 (3):236–247, 2005.

[50] Rusnė Ivaškevičiūtė-Povilauskienė, Paulius Kizevičius, Ernestas Nacius, Domas Jokubauskis, Kęstutis Ikamas, Alvydas Lisauskas, Natalia Alexeeva, Ieva Matulaitienė, Vytautas Jukna, Sergej Orlov, et al. Terahertz structured light: nonparaxial airy imaging using silicon diffractive optics. *Light: Science & Applications*, 11(1):326, 2022.

[51] L Schermelleh, A Ferrand, T Huser, C Eggeling, M Sauer, O Biehlmaier, and G Drummen. Super-resolution microscopy demystified. *Nature Cell Biology*, 21(1):72–84, 2019.

[52] J Vangindertael, R Camacho, W Sempels, H Mizuno, P Dedecker, and K P F Janssen. An introduction to optical super-resolution microscopy for the ad-

venturous biologist. *Methods and Applications in Fluorescence*, 6(2):022003, mar 2018. doi: 10.1088/2050-6120/aaae0c. URL `https://dx.doi.org/10.1088/2050-6120/aaae0c`.

[53] Masahito Yamanaka, Nicholas I. Smith, and Katsumasa Fujita. Introduction to super-resolution microscopy. *Microscopy*, 63(3):177–192, 03 2014. ISSN 2050-5698. doi: 10.1093/jmicro/dfu007. URL `https://doi.org/10.1093/jmicro/dfu007`.

[54] Mikhail Glyavin. Gyrotrons for high-power terahertz science and technologies. 07 2019.

[55] Jonathan Blackledge, Albert Boretti, Lorenzo Rosa, and Stefania Castelletto. Fractal graphene patch antennas and the thz communications revolution. volume 1060, 02 2021. doi: 10.1088/1757-899X/1060/1/012001.

[56] C Harrison Brodie, Isaac Spotts, Hajer Reguigui, Camille A Leclerc, Michael E Mitchell, Jonathan F Holzman, and Christopher M Collier. Comprehensive study of 3d printing materials over the terahertz regime: absorption coefficient and refractive index characterizations. *Optical Materials Express*, 12(9):3379–3402, 2022.

[57] Radoslaw Piesiewicz, Christian Jansen, S Wietzke, Daniel Mittleman, Martin Koch, and Thomas Kürner. Properties of building and plastic materials in the thz range. *International Journal of Infrared and Millimeter Waves*, 28: 363–371, 2007.

[58] CP Pearman, CS Adams, SG Cox, PF Griffin, DA Smith, and IG Hughes. Polarization spectroscopy of a closed atomic transition: applications to laser-frequency locking. *Journal of Physics B: Atomic, Molecular and Optical Physics*, 35(24):5141, 2002.

[59] Christopher Carr, Charles S Adams, and Kevin J Weatherill. Polarization spectroscopy of an excited state transition. *Optics letters*, 37(1):118–120, 2012.

[60] Ronald WP Drever, John L Hall, Frank V Kowalski, James Hough, GM Ford, AJ Munley, and Hywel Ward. Laser phase and frequency stabilization using an optical resonator. *Applied Physics B*, 31:97–105, 1983.

[61] C Wieman and Th W Hänsch. Doppler-free laser polarization spectroscopy. *Physical Review Letters*, 36(20):1170, 1976.

[62] RE Teets, FV Kowalski, WT Hill, N Carlson, and TW Hansch. Laser polarization spectroscopy. In *Advances in Laser Spectroscopy I*, volume 113, pages 80–87. SPIE, 1977.

[63] ML Harris, CS Adams, SL Cornish, IC McLeod, E Tarleton, and IG Hughes. Polarization spectroscopy in rubidium and cesium. *Physical Review A—Atomic, Molecular, and Optical Physics*, 73(6):062509, 2006.

[64] Eric D Black. An introduction to pound–drever–hall laser frequency stabilization. *American journal of physics*, 69(1):79–87, 2001.

[65] Arthur Edelstein, Nenad Amodaj, Karl Hoover, Ron Vale, and Nico Stuurman. Computer control of microscopes using μmanager. *Current protocols in molecular biology*, 92(1):14–20, 2010.

[66] Abbe. The relation of aperture and power in the microscope (continued). *Journal of the Royal Microscopical Society*, 2(4):460–473, 1882.

[67] Rayleigh. Xxxi. investigations in optics, with special reference to the spectroscope. *The London, Edinburgh, and Dublin Philosophical Magazine and Journal of Science*, 8(49):261–274, 1879.

[68] Charles S Adams and Ifan Hughes. *Optics f2f: from Fourier to Fresnel*. Oxford University Press, 2019.

[69] Carroll Mason Sparrow. On spectroscopic resolving power. *Astrophysical Journal, vol. 44, p. 76*, 44:76, 1916.

[70] Martin V Kadiev. Using the modulation transfer function as a metric for lens sharpness. 2020.

[71] Norman Koren, Robert C Sumner, and Henry Koren. Measuring mtf with wedges: pitfalls and best practices. *Electronic Imaging*, 29:6–11, 2017.

[72] G Beziuk, PP Jarzab, K Nowak, EF Plinski, MJ Walczakowski, and JS Witkowski. Dielectric properties of the fr-4 substrates in the thz frequency range. In *2012 37th International Conference on Infrared, Millimeter, and Terahertz Waves*, pages 1–2. IEEE, 2012.

[73] International Organization for Standardization. Iso 12233:2024 - digital cameras — resolution and spatial frequency responses, 2024. URL `https://www.iso.org/standard/88626.html`. Accessed: 2025-03-05.

[74] Kenichiro Masaoka, Takayuki Yamashita, Yukihiro Nishida, and Masayuki Sugawara. Modified slanted-edge method and multidirectional modulation transfer function estimation. *Optics express*, 22(5):6040–6046, 2014.

[75] Hang Li, Changxiang Yan, and Jianbing Shao. Measurement of the modulation transfer function of infrared imaging system by modified slant edge method. *Journal of the Optical Society of Korea*, 20(3):381–388, 2016.

[76] Farhank Saber Braim. *Slanting EDGE Method for Modulation Transfer Function Computation of X-Ray System*. PhD thesis, Universiti Teknologi Malaysia, 2013.

[77] F Kharfi, O Denden, A Bourenane, T Bitam, and A Ali. Spatial resolution limit study of a ccd camera and scintillator based neutron imaging system according to mtf determination and analysis. *Applied Radiation and Isotopes*, 70(1):162–166, 2012.

[78] Albert Abraham Michelson. *Studies in optics*. Courier Corporation, 1995.

[79] Krishnendu Samanta and Joby Joseph. An overview of structured illumination microscopy: recent advances and perspectives. *Journal of Optics*, 23 (12):123002, 2021.

[80] Kenneth A Myers and Christopher Janetopoulos. Recent advances in imaging subcellular processes. *F1000Research*, 5:F1000–Faculty, 2016.

[81] Amit Lal, Chunyan Shan, and Peng Xi. Structured illumination microscopy image reconstruction algorithm. *IEEE Journal of Selected Topics in Quantum Electronics*, 22(4):50–63, 2016.

[82] Nadya Chakrova, Bernd Rieger, and Sjoerd Stallinga. Deconvolution methods for structured illumination microscopy. *JOSA A*, 33(7):B12–B20, 2016.

[83] Yueshu Xu, Yile Sun, Hanmeng Wu, Wen Cao, Ling Bai, Siwei Tao, Zonghan Tian, Yudong Cui, Xiang Hao, Cuifang Kuang, et al. Regularized deconvolution for structured illumination microscopy via accelerated linearized admm. *Optics & Laser Technology*, 169:110119, 2024.

[84] Xin Chen, Suyi Zhong, Yiwei Hou, Ruijie Cao, Wenyi Wang, Dong Li, Qionghai Dai, Donghyun Kim, and Peng Xi. Superresolution structured illumination microscopy reconstruction algorithms: a review. *Light: Science & Applications*, 12(1):172, 2023.

[85] Kaiqin Chu, Paul J McMillan, Zachary J Smith, Jie Yin, Jeniffer Atkins, Paul Goodwin, Sebastian Wachsmann-Hogiu, and Stephen Lane. Image reconstruction for structured-illumination microscopy with low signal level. *Optics express*, 22(7):8687–8702, 2014.

[86] Xiaoshuai Huang, Junchao Fan, Liuju Li, Haosen Liu, Runlong Wu, Yi Wu, Lisi Wei, Heng Mao, Amit Lal, Peng Xi, et al. Fast, long-term, super-resolution imaging with hessian structured illumination microscopy. *Nature biotechnology*, 36(5):451–459, 2018.

[87] Christian Karras, Maria Smedh, Ronny Förster, Hendrik Deschout, Julia Fernandez-Rodriguez, and Rainer Heintzmann. Successful optimization of reconstruction parameters in structured illumination microscopy–a practical guide. *Optics Communications*, 436:69–75, 2019.

[88] Victor Perez, Bo-Jui Chang, and Ernst Hans Karl Stelzer. Optimal 2d-sim reconstruction by two filtering steps with richardson-lucy deconvolution. *Scientific reports*, 6(1):37149, 2016.

[89] Mélanie TM Hannebelle, Esther Raeth, Samuel M Leitao, Tomáš Lukeš, Jakub Pospíšil, Chiara Toniolo, Olivier F Venzin, Antonius Chrisnandy, Prabhu P Swain, Nathan Ronceray, et al. Open-source microscope add-on for structured illumination microscopy. *Nature Communications*, 15(1):1550, 2024.

[90] Kai Wicker. Non-iterative determination of pattern phase in structured illumination microscopy using auto-correlations in fourier space. *Optics express*, 21(21):24692–24701, 2013.

[91] Christiaan H Righolt, Johan A Slotman, Ian T Young, Sabine Mai, Lucas J van Vliet, and Sjoerd Stallinga. Image filtering in structured illumination microscopy using the lukosz bound. *Optics Express*, 21(21):24431–24451, 2013.

[92] Lin Shao, Peter Kner, E Hesper Rego, and Mats GL Gustafsson. Super-resolution 3d microscopy of live whole cells using structured illumination. *Nature methods*, 8(12):1044–1046, 2011.

[93] Joseph W Goodman. *Introduction to Fourier optics*. Roberts and Company publishers, 2005.

[94] Charles Sumner Williams and Orville A Becklund. *Introduction to the optical transfer function*, volume 112. SPIE Press, 2002.

[95] Dan Dan, Ming Lei, Baoli Yao, Wen Wang, Martin Winterhalder, Andreas Zumbusch, Yujiao Qi, Liang Xia, Shaohui Yan, Yanlong Yang, et al. Dmd-based led-illumination super-resolution and optical sectioning microscopy. *Scientific reports*, 3(1):1116, 2013.

[96] Alistair Curd, Alexa Cleasby, Katarzyna Makowska, Andrew York, Hari Shroff, and Michelle Peckham. Construction of an instant structured illumination microscope. *Methods*, 88:37–47, 2015.

[97] H Shabani, A Doblas, G Saavedra, and C Preza. 3d structured illumination microscopy using an incoherent illumination system based on a fresnel biprism. In *Three-Dimensional and Multidimensional Microscopy: Image Acquisition and Processing XXV*, volume 10499, page 1049903. SPIE, 2018.

[98] Feifei Wei, Joseph Louis Ponsetto, and Zhaowei Liu. Plasmonic structured illumination microscopy. In *Plasmonics and Super-Resolution Imaging*, pages 127–163. Jenny Stanford Publishing, 2017.

[99] AD Squires and RA Lewis. Feasibility and characterization of common and exotic filaments for use in 3d printed terahertz devices. *Journal of Infrared, Millimeter, and Terahertz Waves*, 39:614–635, 2018.

[100] Reto Fiolka, Markus Beck, and Andreas Stemmer. Structured illumination in total internal reflection fluorescence microscopy using a spatial light modulator. *Optics letters*, 33(14):1629–1631, 2008.

[101] Arash Sabatyan and Seyyed Akbar Hoseini. Fresnel biprism as a 1d refractive axicon. *Optik*, 124(21):5046–5048, 2013.

[102] David J Cuccia, Frederic Bevilacqua, Anthony J Durkin, Frederick R Ayers, and Bruce J Tromberg. Quantitation and mapping of tissue optical properties using modulated imaging. *Journal of biomedical optics*, 14(2):024012–024012, 2009.

[103] Rong-Wen Lu, Ben-Quan Wang, Qiu-Xiang Zhang, and Xin-Cheng Yao. Super-resolution scanning laser microscopy through virtually structured detection. *Biomedical optics express*, 4(9):1673–1682, 2013.

[104] Yiming Lu, Taeyoon Son, Tae-Hoon Kim, David Le, and Xincheng Yao. Virtually structured detection enables super-resolution ophthalmoscopy of rod and cone photoreceptors in human retina. *Quantitative Imaging in Medicine and Surgery*, 11(3):1060, 2021.

[105] Yanan Zhi, Benquan Wang, and Xincheng Yao. Super-resolution scanning laser microscopy based on virtually structured detection. *Critical Reviews in Biomedical Engineering*, 43(4), 2015.

[106] Hui-Wen Lu-Walther, Martin Kielhorn, Ronny Förster, Aurélie Jost, Kai Wicker, and Rainer Heintzmann. fastsim: a practical implementation of fast structured illumination microscopy. *Methods and Applications in Fluorescence*, 3(1):014001, 2015.

[107] Hyunwoo Kim, Yeong-Hyeon Seo, Jaehun Jeon, and Ki-Hun Jeong. Lissajous scanning structured illumination microscopy. *Biomedical Optics Express*, 11 (10):5575–5585, 2020.

[108] Luis Miguel Sanchez-Brea, Angela Soria-Garcia, Joaquin Andres-Porras, Veronica Pastor-Villarrubia, Mahmoud H. Elshorbagy, Jesus del Hoyo Muñoz, Francisco Jose Torcal-Milla, and Javier Alda. Diffractio: an open-source library for diffraction and interference calculations. In Peter J. de Groot, Felipe Guzman, and Pascal Picart, editors, *Optics and Photonics for Advanced Dimensional Metrology III*, volume 12997, page 129971B. International Society for Optics and Photonics, SPIE, 2024. doi: 10.1117/12.3021879. URL `https://doi.org/10.1117/12.3021879`.

[109] Fabin Shen and Anbo Wang. Fast-fourier-transform based numerical integra-

tion method for the rayleigh–sommerfeld diffraction formula. *Applied optics*, 45(6):1102–1110, 2006.

[110] Emiel Por, Maaike van Kooten, and Vanja Sarkovic. Nyquist–shannon sampling theorem. *Leiden University*, 1(1):1–2, 2019.

[111] Vulugundam Anitha, Ankur Beohar, and Anveshkumar Nella. Thz imaging technology trends and wide variety of applications: a detailed survey. *Plasmonics*, 18(2):441–483, 2023.

[112] Jean-Baptiste Sibarita. Deconvolution microscopy. *Microscopy Techniques: -/-*, pages 201–243, 2005.

[113] Jean-Luc Starck, Eric Pantin, and Fionn Murtagh. Deconvolution in astronomy: A review. *Publications of the Astronomical Society of the Pacific*, 114 (800):1051, 2002.

[114] André Jalobeanu, Laure Blanc-Féraud, and Josiane Zerubia. Satellite image deconvolution using complex wavelet packets. In *Proceedings 2000 International Conference on Image Processing (Cat. No. 00CH37101)*, volume 3, pages 809–812. IEEE, 2000.

[115] Oleg V Michailovich and Dan R Adam. Deconvolution of medical images from microscopic to whole body images. In *Blind Image Deconvolution*, pages 193–262. CRC Press, 2017.

[116] Kiarash Ahi and Mehdi Anwar. Developing terahertz imaging equation and enhancement of the resolution of terahertz images using deconvolution. In *Terahertz physics, devices, and systems X: advanced applications in industry and defense*, volume 9856, pages 57–74. SPIE, 2016.

[117] Wei Ning, Feng Qi, Zhaoyang Liu, Yelong Wang, Hongming Wu, and Jinkuan Wang. Resolution enhancement in terahertz imaging via deconvolution. *IEEE Access*, 7:65116–65121, 2019.

[118] Gillian C Walker, John W Bowen, Julien Labaune, J-Bianca Jackson, Sillas Hadjiloucas, John Roberts, Gerard Mourou, and Michel Menu. Terahertz deconvolution. *Optics express*, 20(25):27230–27241, 2012.

[119] Yang Chen, Shengyang Huang, and Emma Pickwell-MacPherson. Frequency-wavelet domain deconvolution for terahertz reflection imaging and spectroscopy. *Optics express*, 18(2):1177–1190, 2010.

[120] Ali Shayei, Zahra Kavehvash, and Mahdi Shabany. Improved-resolution millimeter-wave imaging through structured illumination. *Appl. Opt.*, 56 (15):4454–4465, May 2017. doi: 10.1364/AO.56.004454. URL `https://opg.optica.org/ao/abstract.cfm?URI=ao-56-15-4454`.

[121] John True, Chengjie Xi, Nathan Jessurun, Kiarash Ahi, and Navid Asadizanjani. Review of thz-based semiconductor assurance. *Optical Engineering*, 60(6):060901–060901, 2021.

If you made it this far, well done! Unless you hit the end key.

Colophon

This thesis is based on a template developed by Matthew Townson and Andrew Reeves. It was typeset with LaTeX 2_ε. It was created using the *memoir* package, maintained by Lars Madsen, with the *madsen* chapter style. The font used is Latin Modern, derived from fonts designed by Donald E. Kunith.